Modeling Linear and Nonlinear Soft Ferromagnetic Materials

Thesis project from

Sebastià Agramunt Puig

under the supervision of

Dr. Àlvar Sánchez Moreno
Dr. Nuria Del Valle Benedí
Dr. Carles Navau Ros

Departament de Física
Universitat Autònoma de Barcelona

Bellaterra, September 2013

Als meus pares,
Josep Sebastià i Empar,
i a la memòria dels meus iaios,
Justo i José.

Preface

Today magnets form part of our daily life. They are responsible for most of the energy generation (e.g. turbines), conversion (e.g. transformers) and its use (e.g. motors). In these applications the precise control of magnetic fields and magnetization is essential to devise new applications or to improve the existing ones. All these would not be possible without an impressive development of magnetic materials. For example, in the last century very large (hard magnets) and very small (soft magnets) values of crystalline anisotropy have been achieved, spanning in five orders of magnitude. The vast range of coercivities makes possible the design of the shape of the hysteresis loop desired for a particular application.

Soft ferromagnets are of great interest because they can guide and concentrate magnetic fields and present low hysteresis and large values of both saturation magnetization and susceptibility. These materials are found, for instance, in electromagnets, where a soft ferromagnetic core is set to concentrate the field, and in electrical transformers, motors or generators, in which the low power loss is an advantage.

The large number of existing and potential applications of soft ferromagnets ranges from large scales (meters) to very small scales (nanometers). One of the large scale applications is superconducting magnetic levitation. Superconductors have demonstrated to present stable and passive levitation lifting weights of hundreds of kilograms. Using these concepts, superconducting materials can be located in a vehicle that levitates above a permanent-magnet guideway in what is known a magnetic levitation vehicle. The main advantage of this technology is its contactless nature which allows a major reduction of friction, and therefore larger vehicle speeds can be achieved with the same power consumption. Soft ferromagnets located in the guideway modify the magnetic field landscape of the permanent magnets leading to optimized values of levitation force and stability of the levitating superconducting vehicle.

At the small scale, a very important application of soft ferromagnets is in magnetic recording and since few decades ago, this industry has been pushing hard in the deep understanding of magnetism at the nanoscale. In essence magnets produce magnetic fields that can be used to store bits of information. This information can be read using a magnetoresistive read head that consists of a multilayer of soft ferromagnetic-metal-soft ferromagnetic with one of the ferromagnetic layers (pinned layer) attached to an antiferromagnet. The other ferromagnetic layer is free to sense the magnetic field at very small spatial scales. Information can also be stored in arrays of magnetic tunnel junctions or simply cylindrical soft ferromagnets. These latter ones can present a magnetic vortex state at remanence, a magnetization pattern that can store two bits of information increasing the information density (number of bits per area of magnetic media).

The aim of the present thesis is to model the behavior of soft ferromagnets in the macroscopic and microscopic scales and their interaction with other magnetic materials such as permanent magnets, superconductors or antiferromagnets for their use in the mentioned applications.

This thesis is structured in two parts. In Part I we introduce a model that describes the mutual interaction of a linear, isotropic, and homogeneous soft ferromagnetic bar with a hard type II superconductor. The model is applied to the optimization of a typical magnetic levitation guideway. In Part II a non linear model based on micromagnetic scheme is introduced to model soft ferromagnets at the nanoscale range. The model is applied to the study of exchange biased systems and the control of magnetic vortex states.

Before starting with the first part, we review in the first chapter the main concepts used throughout the thesis, introducing the main characteristics of ferromagnetic materials and the critical-state model, a model widely accepted in the description of the macroscopic behavior of a hard type II superconductor, which we will use.

In the first part (Chapter 2) we start by reviewing the properties that make superconductors good candidates to achieve a passive and static levitation. In Chapter 3 we introduce the model of a linear, isotropic, and homogeneous soft ferromagnet in the limit of very large susceptibility interacting with a superconductor. The magnetic poles in the ferromagnet and the currents induced in the superconductor will be calculated using a functional related to their magnetic energy. An advantage of the model presented is that both elements will mutually interact so that the magnetic pole density of the ferromagnet will be affected by the currents induced in the superconductor and vice versa.

A systematic study of the soft ferromagnet will be performed in Chapter 4. The magnetic pole density in the ferromagnet will be studied when submitted to different applied fields. The first, a uniform applied field, is used to understand the basic phenomena and to compare our results with the existing analytical ones. Then the magnetic response of the ferromagnet in the fields produced by one or two magnets (non-uniform) is studied. The results of this chapter will be helpful to determine the size and shape that a soft ferromagnet must have in each of the three applied fields to enhance the magnetic field in a certain region of the space.

In a Chapter 5 we use the results obtained in the previous chapter to maximize the levitation force and stability of a typical magnetic levitation system based on superconductors. Results in this chapter may be useful when designing future magnetic levitation systems.

At the beginning of Part II we set the motivation for the study of magnetism at the nanoscale, and in particular we review the importance of soft ferromagnets in devices using giant magnetoresistance and magnetic memories. The model for a non-linear ferromagnet in the micromagnetic framework is presented in Chapter 6.

In Chapter 7 we present the hysteretic behavior of a ferromagnetic cylinder at the nanoscale. Typically, the most stable magnetic configuration for this shape and size in a soft ferromagnet is the magnetic vortex state. A simple procedure is introduced to achieve independent control of chirality and polarity of a vortex state by simply adjusting the applied field direction given a particular dot geometry.

An extension of the model presented in Chapter 6 is made in Chapter 8 to take into account the effect that an antiferromagnetic material makes to the macroscopic behavior of a soft ferromagnet. In this case, we will reproduce the basic phenomena of exchange bias and study the distortion that a magnetic vortex state suffers along the thickness of the soft ferromagnet due to the surface interaction with the antiferromagnet.

Finally, in Chapter 9 the conclusions of this thesis and future lines are presented.

Contents

CHAPTER 1

Basic Concepts in Magnetism

In this chapter we review the basic concepts used in this thesis. In the first part we present the main physical quantities describing the magnetism of materials. In the second section we briefly explain ferromagnetism and the energies involved. Finally, we introduce the main properties of superconducting materials and present a macroscopic model that describes the magnetic behavior of hard superconductors.

1.1 Magnetostatics and Magnetic Materials

A magnetic material is a material that produces a magnetic field either spontaneous or when submitted to an external applied field. In this section we review some key concepts involving the magnetism of materials.

1.1.1 Magnetic Moment and Magnetization

In classical magnetostatics the dipolar magnetic moment created by a current density $\mathbf{J}$ is

$$\mathbf{m} = \frac{1}{2}\int \mathbf{r} \times \mathbf{J}(\mathbf{r})\mathrm{d}V, \tag{1.1}$$

where V is the volume where the current is present. In magnetic materials, apart from the magnetic dipole induced by the currents flowing through it, there is an intrinsic magnetic moment of quantum mechanical origin associated with the spin (angular momentum) of each electron [1, 2]. In materials where the spins locally point in the same direction we can define the magnetization vector $\mathbf{M}$ which is a mesoscopic volume average of the magnetic moments $\mathbf{M}(\mathbf{r}) = \mathrm{d}\mathbf{m}/\mathrm{d}V$. The macroscopic volume average magnetization of a sample either from currents or magnetic moments is defined by $\mathbf{M}_{\mathrm{vol}} \equiv \int \mathbf{m}\mathrm{d}V/V_{\mathrm{s}}$ where V_{s} is the volume of the sample.

1.1.2 Maxwell's Static Equations: Magnetostatics

When no magnetic moments or currents vary on time, the two fundamental equations in magnetostatics are

$$\begin{aligned} \nabla \times \mathbf{H} &= \mathbf{J}, & (1.2)\\ \nabla \cdot \mathbf{B} &= 0, & (1.3) \end{aligned}$$

where **H** is the magnetic field, **B** is the magnetic induction and **J** is the free current density [3]. The boundary conditions of the magnetic induction and the magnetic field between two magnetic materials are

$$\begin{aligned} (\mathbf{H}_1 - \mathbf{H}_2) \times \mathbf{e}_\mathrm{n} &= 0, & (1.4)\\ (\mathbf{B}_1 - \mathbf{B}_2) \cdot \mathbf{e}_\mathrm{n} &= 0, & (1.5) \end{aligned}$$

where 1 and 2 indicate the magnetic medium and $\mathbf{e}_\mathrm{n}$ the unit vector perpendicular to the interface pointing from medium 1 to 2. The quantity that relates magnetic induction and magnetic field is the magnetization according to

$$\mathbf{B} = \mu_0 \left(\mathbf{H} + \mathbf{M}\right), \tag{1.6}$$

where μ_0 is the vacuum permeability. The divergenceless nature of the magnetic induction [see Eq. (1.3)] which is also accomplished in the non-static regime allows the definition of a magnetic vector potential $\mathbf{A}(\mathbf{r})$ such that

$$\mathbf{B}(\mathbf{r}) = \nabla \times \mathbf{A}(\mathbf{r}). \tag{1.7}$$

The choice of $\nabla \cdot \mathbf{A}(\mathbf{r})$ or gauge is free since it does not change $\mathbf{B}(\mathbf{r})$. A common gauge used is the Coulomb gauge $\nabla \cdot \mathbf{A}(\mathbf{r}) = 0$.

1.1.3 Magnetostatics without Free Currents

In magnetic materials where the free current density is zero (**J**=0) Eqs. (1.2), (1.3), (1.4) and (1.5) can be rewritten as

$$\begin{aligned} \nabla \times \mathbf{H} &= 0, & (1.8)\\ \nabla \cdot \mathbf{H} &= \rho_\mathrm{M}, & (1.9)\\ (\mathbf{H}_1 - \mathbf{H}_2) \times \mathbf{e}_\mathrm{n} &= 0, & (1.10)\\ (\mathbf{H}_1 - \mathbf{H}_2) \cdot \mathbf{e}_\mathrm{n} &= -\sigma_\mathrm{M}, & (1.11) \end{aligned}$$

where ρ_M and σ_M are the volume and surface magnetic pole densities, respectively and are defined as

$$\begin{aligned} \rho_\mathrm{M} &\equiv -\nabla \cdot \mathbf{M}, & (1.12)\\ \sigma_\mathrm{M} &\equiv (\mathbf{M}_1 - \mathbf{M}_2) \cdot \mathbf{e}_\mathrm{n}. & (1.13) \end{aligned}$$

Equations (1.9) and (1.11) along with Eqs. (1.12) and (1.13) indicate that the source of magnetic field is due to a variation of the magnetization either in the volume [Eq. (1.12)] or in the surface sample [Eq. (1.13)]. Magnetic field lines start in positive magnetic poles and end in negative magnetic poles but never forming a closed loop.

The vanishing curl of $\mathbf{H}(\mathbf{r})$ in current free magnetic materials allows the definition of the magnetic scalar potential ϕ, whose gradient is $\mathbf{H}(\mathbf{r}) = -\nabla\phi(\mathbf{r})$. This potential is enough to describe the magnetic field in the whole space.

1.1.4 Magnetic Susceptibility and Linear Isotropic and Homogeneous Materials

Magnetization $\mathbf{M}$ at each point in the sample is related to the magnetic field $\mathbf{H}$ in the same point as

$$\mathbf{M}(\mathbf{r}) = \chi(\mathbf{H}, \mathbf{r})\mathbf{H}(\mathbf{r}), \tag{1.14}$$

where $\chi(\mathbf{H}, \mathbf{r})$ is an intrinsic parameter of the magnetic material known as the magnetic susceptibility. In general, χ is a tensor that depends on the position $\mathbf{r}$ and the local field $\mathbf{H}(\mathbf{r})$ inside the material. A linear isotropic and homogeneous material (LIH) is defined as a material for which χ is a scalar quantity (isotropic) independent of the field (linear) and the position (homogeneous) so that

$$\mathbf{M}(\mathbf{r}) = \chi\mathbf{H}(\mathbf{r}), \tag{1.15}$$

is accomplished being χ is a real quantity. A LIH material can also be characterized by the magnetic permeability μ which is related to the susceptibility as

$$\chi = \frac{\mu}{\mu_0} - 1. \tag{1.16}$$

In a LIH material without any free current the combination of Eqs. (1.3), (1.6), (1.12) and (1.15) leads to the conclusion that no volumic poles are induced and therefore the divergence of $\mathbf{H}$ vanishes inside the sample. Only the difference (divergence) of $\mathbf{M}$ at the surface induce a surface magnetic pole density according to Eq. (1.13). Another characteristic of this approximation (LIH) is that no irreversible processes can be described.

1.1.5 Demagnetizing Fields and Demagnetizing Factors

The magnetic behavior of a sample does not only depend on its intrinsic properties such as $\chi(\mathbf{H}, \mathbf{r})$ but on the shape of the magnetic sample itself [4, 5]. This can be understood by looking at the boundary conditions Eqs. (1.4) and (1.5). The geometrical effects of the magnetic sample are usually called demagnetizing effects. The demagnetizing field $\mathbf{H}_\mathrm{d}$ or stray field is the magnetic field generated by the surface and volumic magnetic pole densities in a magnet. If an external magnetic field $\mathbf{H}_\mathrm{a}$ is applied to the sample, the total magnetic field at any point in the space is

$$\mathbf{H} = \mathbf{H}_\mathrm{a} + \mathbf{H}_\mathrm{d}. \tag{1.17}$$

The averaged volume magnetization of a sample is related to the averaged volume demagnetizing field $\mathbf{H}_{\mathrm{d,vol}}$ as

$$\mathbf{H}_{\mathrm{d,vol}} = -N\mathbf{M}_{\mathrm{vol}}, \tag{1.18}$$

where N is the magnetometric demagnetizing tensor. In general, $\mathbf{H}_{\mathrm{d,vol}}$ and $\mathbf{M}_{\mathrm{vol}}$ are not parallel even in LIH materials. In some cases, as for instance LIH ellipsoidal samples this two quantities are strictly parallel and the demagnetizing tensor reduces to a scalar quantity called demagnetizing factor which can be defined as

$$N = -\frac{H_{\mathrm{d,vol}}}{M_{\mathrm{vol}}}. \tag{1.19}$$

In general, the directions of $\mathbf{H}_{\mathrm{a}}$ for which all the averaged magnetic quantities are parallel and the demagnetizing tensor is reduced to a scalar are called the principal directions of the sample. In this case, the demagnetizing tensor [defined in Eq. 1.18] expressed in the basis of the principal directions is diagonal. i.e. has zeros in the non-diagonal part of the matrix.

1.2 Special Cases of Linear Isotropic and Homogeneous Magnetic Materials

The demagnetizing fields for LIH materials with $\chi \to 0^+$ and $\chi \to \infty$ are analyzed in this section.

1.2.1 $\chi \to \infty$

When a uniform field is applied to a sample of positive susceptibility, the average volume magnetization $\mathbf{M}_{\mathrm{vol}}$ has the same direction as the external uniform applied field $\mathbf{H}_{\mathrm{a}}$, as shown in Fig. 1.1(a). Positive magnetic pole density is generated in the surface whose normal vector (directed outwards the sample) has the same direction as the applied field. Conversely a negative surface magnetic pole density appears when the normal to the surface is antiparallel to the field as indicated by Eq. (1.13).

As seen in Figs. 1.1(a) and 1.1(b) for $\chi > 0$ the magnetic field produced by the poles in the interior of the sample is opposite to the averaged magnetization direction. Therefore, the total magnetic field inside the sample $\mathbf{H} = \mathbf{H}_{\mathrm{a}} + \mathbf{H}_{\mathrm{d}}$ is reduced with respect to the applied field. The fact that $\mathbf{H}_{\mathrm{d}}$ reduces the magnetic field inside the sample gives the original name of demagnetizing field to $\mathbf{H}_{\mathrm{d}}$.

When $\chi \to \infty$, we can see by the definition of magnetic susceptibility Eq. (1.14) that $\mathbf{H}$ inside the sample must be zero so that the magnetization $\mathbf{M}$ remains finite. This implies that inside the sample the demagnetizing field is the same but with opposite direction to the applied field, i.e. $\mathbf{H}_{\mathrm{d}} = -\mathbf{H}_{\mathrm{a}}$ as depicted in Fig. 1.1(a). In this case, since the total magnetic field inside the sample is zero (this is, $\mathbf{H}_1 = 0$), the perpendicular boundary condition [Eq. (1.11)] indicates that at the surface of the sample the field takes a value $|\mathbf{H}| = \sigma_{\mathrm{M}}$. No magnetic field component parallel to the surface exists [Eq. (1.10)

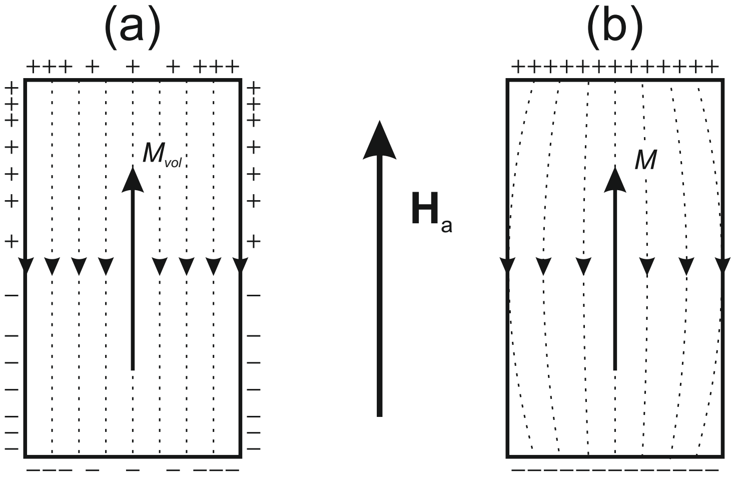

Figure 1.1: Surface magnetic pole density indicated by signs and demagnetizing field lines (dashed) for two LIH materials, $\chi \to \infty$ (a) and $\chi =\to 0^+$(b).

and $\mathbf{H}_1 = 0$] and therefore the magnetic field at the surface is perpendicular to it with expression $\mathbf{H} = \sigma_{\mathrm{M}}\mathbf{e}_{\mathrm{n}}$.

In magnetically soft materials (large χ) the initial slope of a hysteresis loop far from saturation is very large and almost linear. For instance the typical slope for Permalloy material is 10^5. The approximation of $\chi \to \infty$ is only valid in this kind of materials and in the applied field region where the material is far from saturation.

1.2.2 $\chi \to 0^+$

The limit of vanishing χ (from positive values) describes well the saturated regime of ferromagnetic materials. This is, in the limit where the magnetization does not change due to an increment or decrement of the applied magnetic field. It is also a way to describe permanent magnets (PMs), or magnetic materials that due to their intrinsic properties are magnetized mostly in one direction and do not change their magnetization in a large range of applied magnetic fields. A typical example of a permanent magnetic material is NdFeB having huge coercivities about 2.5 Tesla [6].

In the uniform magnetization or, equivalently $\chi = 0$ limit, the magnetic pole density is constant on the surfaces perpendicular to the applied field as shown in Fig. 1.1(b). In this case, even though the magnetization is constant in the sample volume the demagnetizing field is not uniform. This apparent contradiction is solved as follows. For small χ the magnetization of the sample is small according to Eq. (1.14) and therefore small magnetic pole density is generated resulting in a small demagnetizing field. Since $\mathbf{H} = \mathbf{H}_{\mathrm{a}} + \mathbf{H}_{\mathrm{d}}$ a small uniform applied field $\mathbf{H}_{\mathrm{a}} >> \mathbf{H}_{\mathrm{d}}$ will make that inside the material the magnetic field $\mathbf{H}$ is in the direction of $\mathbf{H}_{\mathrm{a}}$. Therefore the magnetization has the same uniform direction as the applied field according to $\mathbf{M} = \chi\mathbf{H}$.

1.3 Ferromagnetic Materials

Even though we can consider magnetic materials as LIH in some cases (explained above), in general they present an irreversible behavior as described by the hysteresis loops. Ferromagnetic materials [2, 7] at a temperature below its Curie temperature T_c (temperature above which the ferromagnetic ordering no longer exists) may present small zones called magnetic domains in which the magnetization remains mostly in one direction. The existence of domains was proposed by Weiss back in the year 1907 in order to explain why materials known to be ferromagnetic did not have a net magnetic moment at the macroscopic scale [8]. The irreversible processes in a ferromagnet (FM) occur due to coherent rotation of the magnetization in a domain or by domain wall displacements. The study of these effects is complicated due to the high non linearity of the problem.

Magnetic domains result from the competition of the main three energies in a FM: the magnetostatic, the exchange and the crystalline anisotropy energies. The magnetostatic energy results from the divergence of the magnetization, or in other words, the magnetic pole densities in a FM. This energy can be written as [1]

$$E_\mathrm{d} = -\frac{1}{2}\mu_0 \int \mathbf{H}_\mathrm{d}\mathbf{M}\mathrm{d}V. \tag{1.20}$$

The minimization of the magnetostatic energy is achieved by reducing the magnetic poles (which is known as the magnetic pole avoidance principle [9]) or equivalently the demagnetizing field inside the sample.

The exchange energy has a quantum origin [1, 10]. It reflects the competition between the Coulomb interaction of two nearby electrons, and the Pauli exclusion principle. This is, electrons in the same place can not have the same spin direction. If the Coulomb interaction is weak two electrons are close and therefore must point in opposite directions, conversely if the Coulomb interaction is strong they can point in the same direction. Heisenberg set up to express the Hamiltonian of this interaction for two spins as [2],

$$H = -2J\mathbf{S}_1 \cdot \mathbf{S}_2, \tag{1.21}$$

where J is the exchange integral and $\mathbf{S}_1$, $\mathbf{S}_2$ are dimensionless quantum operators. In the case of ferromagnetic materials $J > 0$ and neighboring spins point in the same direction.

Ferromagnetic materials present, independently of their shape, directions of easy magnetization [7]. This is, a direction for which saturating the magnetic sample needs for a weaker applied field compared to other directions. This phenomenon is known as the crystalline anisotropy and is related with the crystal structure of the FM. A material with uniaxial crystalline anisotropy has two easy directions and its energy density can be expressed as

$$E = K\sin^2\theta, \tag{1.22}$$

as a first approximation. Here, K is the anisotropy constant with units of J/m^3 and $\theta = 0$ or $\theta = \pi$ are the easy directions.

In soft materials (where the anisotropy is negligibly small) magnetostatic and exchange energies act on different scales to form domains. The main point is that the exchange energy density is several orders of magnitude larger than the magnetostatic one. However the magnetostatic energy density is of long range order whereas the exchange interaction is short range (neighboring spins). In this way, when the magnetic sample is large it forms domains where locally the exchange energy is minimized (spins point in the same direction) and globally the non uniformity of the domains reduces the magnetic pole density lowering the magnetostatic energy. Conversely, when the sample is small, the exchange forces dominate and the sample is uniformly magnetized approaching the limit $\chi = 0$. Using these concepts, Brown announced what would be known as the fundamental theorem of fine particle theory [11]: *the state of the lowest free energy of a ferromagnetic particle is one uniform magnetization if the particle is sufficiently small and one of nonuniform magnetization if it is sufficiently large.* Size effects (not the shape) on a soft fine magnetic particle are studied briefly in Appendix C.

1.4 Hard Superconductors

In this section we briefly review some of the main properties of the superconductors (SCs); readers are referred to [12, 13, 14, 15] for a further and deeper understanding of these materials.

The superconducting state is a thermodynamic state of some materials that when cooled below a critical temperature T_{crit} present two phenomena simultaneously. The first is that the electrical resistance drops abruptly to zero. The second is that for sufficiently low fields the SC presents perfect diamagnetism, this is, the field produced by the material is opposed to that of the applied field leading to null magnetic field intensity in the interior of the sample. Two aspects must be distinguished from the diamagnetic behavior of the SC. The first is the flux exclusion: when the SC is cooled below T_{crit} at zero field and then a field is applied, the magnetic flux does not penetrate the sample. The second is the flux expulsion: cooling the SC in the presence of an applied field makes the magnetic flux to be expelled from the SC as it reaches the SC state. This last effect is known as the Meissner effect. Another fact worth mentioning from SC is that contrary to many magnetic materials in which the source of magnetic field is due to localized magnetic moments in the crystal (dipolar moment due to the angular momentum of the electrons), the SC magnetic response is due to a free current induced in the material.

There are two types of SCs, type I and type II. Type I presents a Meissner state if the applied field H_{a} is below a critical field H_{c} specific for each material. In this type of SC some currents (shielding currents) flowing in a shell of depth λ (penetration depth) are induced in the surface of the SC in order to shield the magnetic induction inside it. So $\mathbf{B}$ is zero in all the sample volume but in the regions where currents penetrate.

Type II SCs have the same properties as type I for any applied field below a certain critical value $H_{c,1}$. However, between $H_{c,1}$ and another larger critical field $H_{c,2}$ ($H_{c,2} > H_{c,1}$), magnetic induction partially penetrate inside the material bulk in the form of superconducting current vortices, a state commonly known as the mixed state. These vortices are quantized in the sense that each of them is surrounded by a current loop whose magnetic flux $\phi = h/2e = 2.07 \cdot 10^{-15}$Wb is quantized.

In type II SC in the mixed state, current vortices repel each other due to the interaction of their magnetic induction generated. As a result, the vortices in a perfect type II SC distribute in a triangular array called the Abrikosov net [16]. Normally, SCs contain defects or impurities that can pin vortices, this is, they can keep a vortex fixed in a position with a force called the pinning force. These imperfections can compensate the repulsion of the vortices and suppress the Abrikosov net generating a non uniform distribution of vortices in the SC. This, at the same time makes a non-uniform distribution of $\mathbf{B}$ in some regions of the SC and according to Eq. (1.2) a macroscopic current density appears. The magnitude of the current density in these regions is limited by the average maximum pinning force, called critical-current density J_c. The type II SCs in the mixed state presenting a strong pinning force are commonly known as hard SCs.

1.4.1 Critical-State Model

The critical-state model is a macroscopic model that describes the magnetic response of hard SCs. It was proposed by C. P. Bean [17, 18] and is based on the assumption that *any electromagnetic force, whatever small, will induce a macroscopic constant current density* J_c. This model applicability has been proved to be very broad to understand magnetic measurements [19, 20, 21, 22, 23, 24, 25, 26]. The critical-state model implicitly assumes that $H_{c,1} = 0$, this is, no surface currents generated in the Meissner state are considered.

In the following we review the main features of the Bean's critical-state model by studying an example. We consider the case of an infinite slab [1] of hard SC immersed in a uniform applied field H_a in the y direction (this slab is finite in the x direction.).

The SC is initially zero-field cooled below T_{crit}. When the applied field is increased from zero some currents will be induced from the edge inwards following the Lenz's law [3] as shown in Fig. 1.2(a). These currents are opposite in sign so that they try to shield SC volume. According to the model, the current density has a constant value J_c and since $J_c = |\nabla \times \mathbf{H}| = |\partial H_y/\partial x|$, the total magnetic field inside the sample decays linearly. This is, at the edge of the sample $H = H_a$ and decreases linearly up to zero. Two regions can be observed here, the region where the current has penetrated and therefore a non-zero magnetic field exists and a region where there is no current and consequently a vanishing magnetic field.

If the applied field is further increased the SC currents penetrate even more inside the sample [Fig. 1.2(b)] up to a field H_p for which the sample is fully penetrated [Fig.

---

[1] An infinite slab is a geometry consisting on two infinite directions and a finite one being the sides of the latter parallel and flat

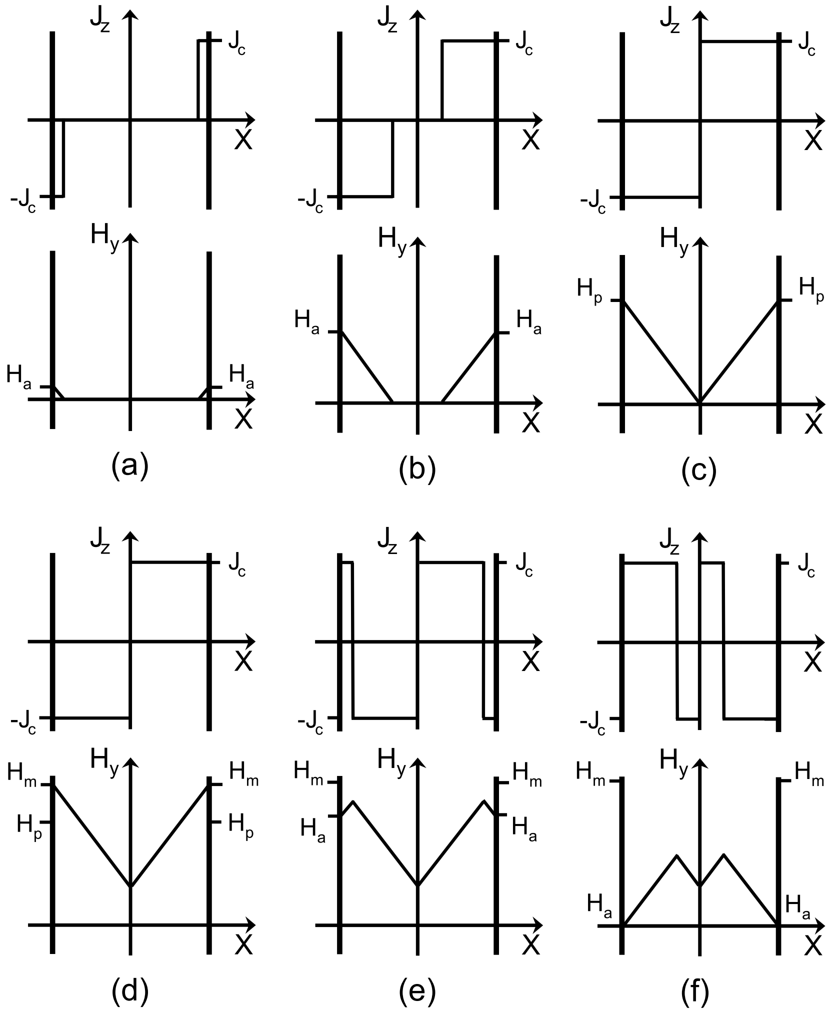

Figure 1.2: Sketch of current and field profiles within the Bean model for infinite slab in which the field is applied in the y direction (one of the infinite directions of the slab).

1.2(c)]. Larger fields than H_p do not induce new currents in the sample but shift the total field at the interior of the sample as shown in Fig. 1.2(d). If the applied field is decreased after a maximum applied field H_m, critical-current density is induced in the opposite direction [Fig. 1.2(e)]. These currents, penetrate in the same way as the initial ones, this is, from the edges to the interior of the sample keeping the already existing currents frozen.

The above example evidences the hysteretic nature of the critical-state model because, for instance, the initial state of zero applied field [Fig. 1.2(a)] is different to the state found at the same field after increasing and decreasing it as shown in Fig. 1.2(f). Even though we have solved the simplest case, critical-state modeling for different geometries such as cylinders or infinitely long bars has been solved and are reviewed in [27].

Part I

Modeling Linear Soft Ferromagnets: Application to Levitation

CHAPTER 2

Superconducting-Ferromagnetic Hybrids

The study of the interaction between soft ferromagnetic materials and superconductors has become an active topic of research because of their potential applications when properly combined. One of the areas that has attracted much attention is high-temperature coated conductors (CCs) [28, 29, 30] where usually [29] the superconducting material is deposited over a ferromagnetic substrate [31]. CCs are combined with soft ferromagnetic materials for electric and power applications such as high magnetic field generation [32], energy storage [33, 34, 35], motors [36] or fault current limiters [37] or even space gyroscopes [38]. For these applications a large critical-current density J_c and low AC losses (hysteretic losses) are advisable. Usually J_c is increased by adding some defects [39] to the SC that pin the vortices, however new studies reveal that soft ferromagnetic parts placed inside [40] or outside [41, 42, 43, 44, 45, 46, 47] the SC can increase its J_c. This effect is produced by the reduction of the magnetic field inside the SC, a result that can also be used to reduce the AC losses in SC cables [48, 49] and increase their transport current.

Another important application of systems where superconductors and ferromagnets appear together is in levitation. In the following sections of this chapter we explain the concept of levitation and the usefulness of superconductors combined with soft ferromagnets for this application.

2.1 Magnetic Levitation

Levitation is the process by which an object or body is suspended by a force against gravity remaining in a stable position without contact. There are many forces on the nature that can make an object to levitate [50] and depending on their nature can be: aerodynamic (produced by gas pressure), acoustic (sound pressure), electrostatic (electric fields) or magnetic (magnetic fields), among others. In this section we will analyze magnetic levitation.

A levitation system must be stable, this is, if the levitating object is slightly displaced from its equilibrium position there must exist some restoring forces so that the levitated object remains in the same position. Stability is crucial in levitation but difficult to achieve, for this reason many systems need a feedback system (and therefore an additional energy input to the system) that changes dynamically the restoring force. This is called active levitation. Conversely if the restoring force does not need for a feedback system the system is called passive. Some systems start to levitate when the levitating object moves. In this case the levitation is called dynamic levitation, and static otherwise. A good example of dynamic levitation is the levitron[1] in which a small spinning magnet levitates over a larger one.

In magnetic levitation the force that makes the object to levitate is magnetic. The first levitating system one may think of consist of a magnet placed above a fixed array of magnets. Is it possible to find an array configuration so that the magnet above can levitate static and passively? The answer is negative, the free magnet will wind up attached to the others. More generally, Earnshaw [51] proved mathematically that stable and static levitation is impossible for a body placed in a repulsive or attractive static force field in which the force is dependent on the inverse square of the distance, which is the case of magnetostatic force. In spite of the difficulty in achieving static and passive levitation with magnetic fields, there are some systems in which the Earnshaw theorem can be circumvented [52] using diamagnetic materials or superconductors as explained in the following section.

2.2 Levitation with Diamagnets and Hard Type II Superconductors

Stable and static levitation with diamagnets is possible because they repel the magnetic field. Levitation of living organisms, that due to their water composition are weakly diamagnetic, has been largely demonstrated. For instance, in Refs. [53, 54] a frog is levitated in a large magnetic field gradient produced by two coils. In biological sciences different techniques [55] have been developed to study the effect of ingravity on cells and plants. Even more surprising is the demonstration of the movement control of single cells [56] due to the field gradient produced by domain walls in ferromagnets.

Diamagnets as levitating objects are only stable if placed in local field minimum [54]. Hard type II superconductors however, can achieve levitation not necessarily in a field minimum. When cooling the superconductor below its critical temperature in an arbitrary (static and non uniform) magnetic field distribution, the superconductor remains stuck in the air as if it was in a medium with a lot of friction [57]. This frictional force requires an energy dissipation that is caused by the pinning of the superconducting

---

[1] Commercially available at http://www.levitron.com/

vortices. This fact makes hard type II superconductors good candidates to achieve static and passive levitation because it is possible to make them levitate over an arbitrary arrangement of permanent magnets.

Hard type II superconductors also present a large levitation force compared to typical diamagnets because its magnetic response is much more large. This property along with the intrinsic stability of hard type II superconductors is used to levitate heavy systems. Some examples of this are linear magnetic bearings [58] or spaceship propulsion systems [59] but the main applicability is on transportation systems based on superconductors. Since the first demonstration of a man loading levitating vehicle based on this technology [60], projects in China [61], Germany [62] and Brazil [63] have been developing new technology to improve both stability and levitating force of the vehicle.

Transportation systems based on hard superconductors usually consist of a guideway of permanent magnets and an array of hard type II superconductors attached to the vehicle. These permanent magnets are made of rare earth materials and have a very large coercivity and high saturation magnetization so that to make a large magnetic field above the guideway. Rare earth price has been soaring for the last few years [64], for this reason some test lines [65, 66, 67] include soft ferromagnets (commonly iron) between the permanent magnets. Soft ferromagnets are also useful to guide the magnetic field of the permanent magnets towards the superconductor and increase its levitation force.

CHAPTER 3

Numerical Model for Magnetic Interaction between SC and FM

In this chapter the mathematical model that describes the magnetic behavior of a superconductor and a soft ferromagnet is described. Such a model will also take into account the mutual interaction of both magnetic elements. Different theoretical approaches have been proposed to understand the effects that a soft ferromagnet produces to a superconductor. Many of them use finite element methods assuming linear [68, 69] or non-linear [70] permeability in the ferromagnetic parts. Other authors have obtained analytical results by considering the SC as a perfect diamagnet and an ideal soft ferromagnet ($\chi \to \infty$) [71] or image methods considering a finite susceptibility [72] in the ferromagnetic materials. Apart from finite element methods, there are also works based on energy minimization of the SC parts considering linear ferromagnetic materials [73] and others that minimize the energy of the ferromagnetic material combined with iterative methods in the superconductor [74].

Our model assumes a SC in the critical state and an ideal soft ferromagnet both translationally symmetric along the same direction. This model allows the simultaneous calculation of the current profiles in the SC and magnetic pole density in the FM by considering their mutual magnetic interaction and their interaction with an external applied field.

3.1 Geometry and Magnetic Elements

We consider a FM and a SC, both infinitely long (translationally symmetric) in the z direction and with rectangular cross section of $a_{\mathrm{SC}} \times b_{\mathrm{SC}}$ for the SC (in the x and y directions, respectively) while the FM cross section occupies $-a_{\mathrm{FM}}/2 \leq x \leq a_{\mathrm{FM}}/2$ in the horizontal direction and $-b_{\mathrm{FM}} \leq y \leq 0$ in the vertical direction. Although here we have considered rectangular elements, the model presented is valid for any cross-sectional shape as long as both elements are infinitely long. An external magnetic field with translational symmetry $\mathbf{H}_e(x, y)$ and no z component is applied to such elements.

The SC is assumed to be in the critical-state regime [17, 18]. In general, the critical-current density J_c is field dependent [75] and could be considered in our model by means of iterative methods. However in the present work will always consider J_c independent of the field. The critical current is also temperature dependent but we assume that our simulations are performed at constant temperature and therefore at a fixed J_c.

The FM is considered ideal [71], this is, we consider a linear, isotropic and homogeneous FM with a very large value of susceptibility ($\chi \to \infty$). This implies that there are only magnetic poles in the surfaces of the ferromagnet and a vanishing total magnetic field $\mathbf{H}$ inside it. By construction of the model, we are implicitly assuming that saturation magnetization can never be achieved.

3.2 Interaction Functional

In this section we describe a functional related to the magnetic energy of the FM and SC. The minimization of this functional will give the physical value of the magnetic pole density distribution in the FM and supercurrents in the SC.

Different functionals have been proposed in the literature [76, 77, 78, 79, 80, 81, 82, 83] to find the induced current distribution on the SC in a translational field, those in refs. [80, 81, 83, 84] for instance are based on the energy as the quantity to be minimized. Our functional is an extension of the one presented in [84].

The current density distribution $J(\mathbf{r})$ on the SC volume and the magnetic charge per unit length (surface magnetic pole density) $\sigma(\mathbf{r})$ on the FM surface at a certain time is obtained by minimizing the functional

$$\mathcal{F}[J, \sigma] = \mathcal{F}_\mathrm{SC}[J, \sigma] + \mathcal{F}_\mathrm{FM}[J, \sigma], \tag{3.1}$$

where

$$\begin{aligned} \mathcal{F}_\mathrm{SC}[J, \sigma] &= \frac{1}{2}\int_S J(\mathbf{r}) A_J(\mathbf{r})\mathrm{d}S - \int_S J(\mathbf{r}) A_{\hat{J}}(\mathbf{r})\mathrm{d}S + \int_S J(\mathbf{r})(A_\mathrm{e}(\mathbf{r}) - \hat{A}_\mathrm{e}(\mathbf{r}))\mathrm{d}S \\ &+ \int_S J(\mathbf{r})(A_\sigma(\mathbf{r}) - \hat{A}_{\hat{\sigma}}(\mathbf{r}))\mathrm{d}S, \qquad (3.2) \\ \frac{\mathcal{F}_\mathrm{FM}[J, \sigma]}{\mu_0} &= \frac{1}{2}\int_l \sigma(\mathbf{r})\phi_\sigma(\mathbf{r})\mathrm{d}l - \int_l \sigma(\mathbf{r})\phi_{\hat{\sigma}}(\mathbf{r})\mathrm{d}l + \int_l \sigma(\mathbf{r})(\phi_\mathrm{e}(\mathbf{r}) - \hat{\phi}_\mathrm{e}(\mathbf{r}))\mathrm{d}l \\ &+ \int_l \sigma(\mathbf{r})(\phi_J(\mathbf{r}) - \hat{\phi}_{\hat{J}}(\mathbf{r}))\mathrm{d}l. \qquad (3.3) \end{aligned}$$

Here, $\mathrm{d}S$ is the differential of area in the transverse section S of the SC whilst $\mathrm{d}l$ is the differential of length in the perimeter l of the transverse area of the FM. The term $\mathcal{F}_\mathrm{SC}[J, \sigma]$ takes into account the interaction of the currents in the SC with themselves (first and second terms), with an external applied field (third term) and with the FM (last term) whereas the term $\mathcal{F}_\mathrm{FM}[J, \sigma]$ is the analogous functional for the FM. In Eqs.

(3.2) and (3.3) A stands for the vector potential, ϕ for the magnetic scalar potential and the subindexes indicate the source, which can be the external applied field e, the supercurrents J in the SC or the magnetic poles σ in the FM. The hat terms represent the quantities in the previous time layer, therefore $\hat{J}$ and $\hat{\sigma}$ are the current densities in the SC and magnetic pole densities in the FM that minimize the functional (3.1) in the previous time[1].

The constraints applied to the magnitudes describing the SC and the FM are different. For the SC we impose the critical-state condition [17] which is $|J| \leq J_c$. We choose the Coulomb gauge so that the potential vector direction is parallel to the current. In the SC a transport current can be considered when minimizing the functional [82] however in the present work we only consider changes in the SC currents due to external magnetic fields, in this case, the net current in a transverse section of the SC is zero, $\int_S J \mathrm{d}S = 0$. For the FM the only constraint needed is $\int_l \sigma(r)\mathrm{d}l = 0$ indicating that no net magnetic charges are induced.

The functional $\mathcal{F}[J,\sigma]$ has units of energy per unit length since the term for the SC (FM) depends on a current density (a magnetic pole density) multiplied by a vector potential (magnetic scalar potential). The first term $\mathcal{F}_{\mathrm{SC}}[J,\sigma]$ cannot be considered as simply the energy per unit length of the SC system since it describes a hysteretic process. $\mathcal{F}_{\mathrm{SC}}[J,\sigma]$ reduces to the functional introduced by Prigozhin [77, 85] if the interaction with the FM is not considered, i.e., $\sigma(\mathbf{r})$ is set to zero. Only under some conditions [82] this functional is equivalent to the magnetic energy. The second term $\mathcal{F}_{\mathrm{FM}}[J,\sigma]$, however, is μ_0 times the energy per unit length of the FM if $J(r)$ is zero, this is so because the FM is non hysteretic. By setting the hat terms in $\mathcal{F}_{\mathrm{FM}}[J,\sigma]$ to zero we recover the functional in [74] in which the behavior of a FM substrate was analyzed by just minimizing the energy of the FM.

Defining the surface magnetic pole density variation $\delta\sigma \equiv \sigma - \hat{\sigma}$ and current density variation $\delta J \equiv J - \hat{J}$ it is possible to obtain another functional $\mathcal{F}'[\delta J,\delta\sigma]$ whose minimization is equivalent to minimize $\mathcal{F}[J,\sigma]$. So, we define

$$\mathcal{F}'[\delta J,\delta\sigma] = \mathcal{F}'_{\mathrm{SC}}[\delta J,\delta\sigma] + \mathcal{F}'_{\mathrm{FM}}[\delta J,\delta\sigma], \tag{3.4}$$

where

$$\begin{aligned}\mathcal{F}'_{\mathrm{SC}}[\delta J,\delta\sigma] &= \frac{1}{2}\int_S \delta J(\mathbf{r})A_{\delta J}(\mathbf{r})\mathrm{d}S + \int_S \delta J(\mathbf{r})(A_{\mathrm{e}}(\mathbf{r}) - \hat{A}_{\mathrm{e}}(\mathbf{r}))\mathrm{d}S \\ &+ \int_S \delta J(\mathbf{r})(A_{\hat{\sigma}}(\mathbf{r}) - \hat{A}_{\hat{\sigma}}(\mathbf{r}))\mathrm{d}S \\ &+ \int_S \delta J(\mathbf{r})A_{\delta\sigma}(\mathbf{r})\mathrm{d}S + \int_S \hat{J}(\mathbf{r})A_{\delta\sigma}(\mathbf{r})\mathrm{d}S\end{aligned} \tag{3.5}$$

---

[1] This time dependence can be introduced either by considering an external applied field which changes with time, or by considering that the external applied field is static and the SC and/or the FM are moved relative to the source of magnetic field. With this latter consideration the external applied field varies with time from the standpoint of the SC and/or the FM. In any case variations are performed quasiestatically.

and

$$\begin{aligned}\frac{\mathcal{F}'_{\rm FM}\left[\delta J,\delta\sigma\right]}{\mu_0} &= \frac{1}{2}\int_l \delta\sigma(\mathbf{r})\phi_{\delta\sigma}(\mathbf{r})\mathrm{d}l + \int_l \delta\sigma(\mathbf{r})(\phi_{\rm e}(\mathbf{r})-\hat{\phi}_{\rm e}(\mathbf{r}))\mathrm{d}l\\ &+ \int_l \delta\sigma(\mathbf{r})(\phi_{\hat{J}}(\mathbf{r})-\hat{\phi}_{\hat{J}}(\mathbf{r}))\mathrm{d}l\\ &+ \int_l \delta\sigma(\mathbf{r})\phi_{\delta J}(\mathbf{r})\mathrm{d}l + \int_l \hat{\sigma}(\mathbf{r})\phi_{\delta J}(\mathbf{r})\mathrm{d}l. \qquad (3.6)\end{aligned}$$

If $\sigma = \delta\sigma + \hat{\sigma}$ and $J = \delta J + \hat{J}$ are introduced in $\mathcal{F}\left[J,\sigma\right]$, we obtain $\mathcal{F}'\left[\delta J,\delta\sigma\right]$ and other terms that only depend on $\hat{J}$ and $\hat{\sigma}$. Because of the definition of $\hat{J}$ and $\hat{\sigma}$, the terms including only them are already minimized and thus are omitted in Eq. (3.4).

3.3 Calculation of Currents and Magnetic Poles

The magnetic behavior of the SC and FM is determined by the supercurrents induced in the former and the magnetic pole density originated in the surface of the latter. In this section we show how to calculate both using the functional (3.4) when they are set in a non-uniform applied field with translational symmetry along the z direction.

Since the currents in the SC are distributed in its cross section we divide it in $N_{\rm SC}$ rectangular-sectioned elements of infinite length and the same cross sectional area $\Delta_x \times \Delta_y = \Delta S$. The current density at each element is assumed to be uniform and with a value $mJ_{\rm c}/m_m$ where m_m is a positive integer and m is an integer between $-m_m$ and m_m. The FM surface is discretized in $N_{\rm FM}$ elements of the same width ΔL and infinite length. In each FM element it is assumed a uniform magnetic pole density that can be $\pm n\Delta\sigma$ where n is a positive integer with arbitrarily high value.

The change of $\mathcal{F}'_{\rm FM}\left[\delta J,\delta\sigma\right]$ due to a magnetic pole density variation $\Delta\sigma$ over the j element of the FM is

$$\begin{aligned}\frac{\Delta\mathcal{F}'_{{\rm FM},j}}{\mu_0} &= \Delta\sigma\Delta L\sum_{p=1}^{N_{\rm FM}} E_{pj}\delta\sigma_p + \frac{1}{2}E_{jj}(\Delta\sigma)^2\Delta L + \Delta\sigma\Delta L\left[Y_{{\rm e},j}-\hat{Y}_{{\rm e},j}\right]\\ &+ \Delta\sigma\Delta L\sum_{k=1}^{N_{\rm SC}}\hat{J}_k\left(Q^{\rm SC}_{kj}-\hat{Q}^{\rm SC}_{kj}\right) + \Delta\sigma\Delta L\sum_{k=1}^{N_{\rm SC}}\delta J_k Q^{\rm SC}_{kj}\\ &+ \sum_{p=1}^{N_{FM}}\sum_{k=1}^{N_{\rm SC}}\hat{\sigma_p}\delta J_k Q^{\rm SC}_{kp}\Delta L, \qquad (3.7)\end{aligned}$$

where E_{pj} and $Q^{\rm SC}_{kj}$ are related to the magnetic scalar potential at the j element of the SC due to a p element of the FM and a k element of the SC, respectively. These quantities are geometrical factors between the element j of the SC and another element of the FM or SC and are defined and explained in Sec. A.1 of Appendix A. $Y_{{\rm e},j}$ is the magnetic scalar potential at the center of an element j in the FM due to an external applied field ($\mathbf{H}_{\rm e}$). The quantity $Q^{\rm SC}_{kj} - \hat{Q}^{\rm SC}_{kj}$ is related to the change in magnetic scalar potential at an element j of the FM due to a change in the relative positions between j and an element k in the SC with respect to the previous time layer.

We can perform the equivalent change of current ΔI in an element i of the SC that leads to a variation of the functional $\mathcal{F}'_{\mathrm{SC}}\left[\delta J, \delta\sigma\right]$ by an amount

$$\begin{aligned}
\frac{\Delta\mathcal{F}'_{\mathrm{SC},i}}{\mu_0} &= \Delta S \Delta I \sum_{k=1}^{N_{\mathrm{SC}}} D_{ki}\delta J_k + \frac{1}{2} D_{ii}(\Delta I)^2 + \Delta I \left[G_{\mathrm{e},i} - \hat{G}_{\mathrm{e},i}\right] \\
&+ \Delta I \sum_{p=1}^{N_{\mathrm{FM}}} \hat{\sigma}_p \left(Q_{pi}^{\mathrm{FM}} - \hat{Q}_{pi}^{\mathrm{FM}}\right) + \Delta I \sum_{p=1}^{N_{\mathrm{FM}}} \delta\sigma_p Q_{pi}^{\mathrm{FM}} \\
&+ \sum_{k=1}^{N_{\mathrm{SC}}} \sum_{p=1}^{N_{\mathrm{FM}}} \hat{J}_k \delta\sigma_p Q_{pk}^{\mathrm{FM}} \Delta S, \qquad (3.8)
\end{aligned}$$

where D_{ki} and Q_{pi}^{FM} are quantities related to the magnetic vector potential over an element i of the SC created by a k element of the SC and a p element of the FM, respectively. As above, the first two quantities are geometrical factors between the element i and another element of the FM or SC, further explanation and exact calculation of D_{ki} and Q_{pi}^{FM} can be found in Appendix A Sec. A.2. $G_{\mathrm{e},i}$ is the magnetic vector potential per unit μ_0 due to an external applied field ($\mathbf{H}_{\mathrm{e}}$). In the third term the quantity $Q_{pi}^{\mathrm{FM}} - \hat{Q}_{pi}^{\mathrm{FM}}$ takes into account the change of magnetic vector potential at the i element of the SC produced by a p element of FM due to a change in the relative position between i and p in the previous and present time layer.

For a given current density $\hat{J}$ and magnetic pole density $\hat{\sigma}$ distributions (both are zero at the beginning) we calculate the next values of J and σ on the new field characterized by A_{e} and ϕ_{e} by minimizing the sum of the two discretized functionals of Eqs. (3.8) and (3.7) in the following way. First we consider $\Delta\sigma = 0$, hence the functional Eq. (3.7) is zero except the last term, and we find the pair of elements in the SC such that by setting a current increment $\Delta I = \Delta S J_c/m_m$ and $-\Delta I$, respectively, the sum of the two functionals would decrease the most but always keeping the condition $|J| \leq J_{\mathrm{c}}$ fulfilled. In the same way, we consider $\Delta I = 0$, and so the functional Eq. (3.8) becomes zero except the last term. We then find the pair of elements in the FM for which an increment of magnetic pole density $\Delta\sigma$ and $-\Delta\sigma$, respectively, would decrease the sum of the two functionals the most. Once the pair of currents and magnetic pole densities are found we choose the pair (either of currents or magnetic poles) that minimizes the most the sum of the functionals. This pair of poles or currents are added to their respective discretization elements. This step of minimization is repeated until the sum of the functionals can not be further minimized. In the process of finding the optimum pair the last term of both Eqs. (3.7) and (3.8) are not considered since they are additive constants independently of the trial-position for ΔI and $\Delta\sigma$.

3.4 Calculation of Levitation Force

In the case of magnetic levitation, we are interested in obtaining the magnetic force over the SC. This force comes from the interaction of the currents in the SC and the magnetic field $\mathbf{H}_\mathrm{m}$ produced by the guideway (FMs and PMs), i.e. it is a Lorentz force. Once we obtain the current distribution in the SC and the magnetic pole density in the FM the vertical force per unit length L exhibited by the SC is

$$\frac{F_\mathrm{y}}{L} = \mu_0 \int_S J_\mathrm{z} H_{\mathrm{m,\,x}}\,\mathrm{d}S, \tag{3.9}$$

where J_z is the current density, S is the cross section of the SC and $H_{\mathrm{m,\,x}}$ is the x-component of the magnetic field created by the guideway (PMs and FM) at the cross-section of the SC. Similarly, horizontal force (guidance force) per unit length is

$$\frac{F_\mathrm{x}}{L} = -\mu_0 \int_S J_\mathrm{z} H_{\mathrm{m,\,y}}\,\mathrm{d}S, \tag{3.10}$$

where $H_{\mathrm{m,\,y}}$ is the y-component of the magnetic field created by the guideway over the SC. In our model, the SC cross section is discretized and Eqs. (3.9) and (3.10) can be approximated as

$$\frac{F_\mathrm{y}}{L} \simeq \mu_0 \sum_{j=1}^{N_\mathrm{SC}} H_{\mathrm{m,\,x},\,j} I_j, \tag{3.11}$$

$$\frac{F_\mathrm{x}}{L} \simeq -\mu_0 \sum_{j=1}^{N_\mathrm{SC}} H_{\mathrm{m,\,y},\,j} I_j, \tag{3.12}$$

respectively. In these two equations $I_j = J_j \Delta S$ is the current at the j-element and $H_{\mathrm{m,\,x},\,j}$, $H_{\mathrm{m,\,y},\,j}$ are the horizontal and vertical components of the field created by the guideway in the center of the element j of the SC.

3.5 Calculation of Stability

In levitation systems it is not only important the force acting on the levitating body (in our case the SC) but the restoring forces over it when the body undergoes small displacements around its equilibrium position. The vertical and horizontal stiffnesses per unit length are defined as

$$\frac{\kappa_{yy}}{L} = -\frac{\partial F_\mathrm{y}/L}{\partial y}, \tag{3.13}$$

$$\frac{\kappa_{xx}}{L} = -\frac{\partial F_\mathrm{x}/L}{\partial x}, \tag{3.14}$$

respectively. For the system to be stable, vertical and horizontal stiffnesses must remain positive around the levitation point.

3.6 Limits and Validity of the Model

The SC is assumed to be below its critical temperature $\mathrm{T_{crit}}$ (around 77K for YBCO) whilst the FM is below its Curie temperature $\mathrm{T_c}$ [7] which is typically 1044K for iron [2]. Our simulations are performed in a quasi-static situation.

The approximation of considering the soft ferromagnet as a perfect soft ferromagnet is justified by the large susceptibilities ($\chi \sim 10^5 - 10^6$) and very low coercivities ($H_c \sim 1 - 10$ A/m) found in some magnetic materials manufactured today [2, 86, 87]. These ferromagnets are smartly located in electromagnets, transformers or motors where low coercivities and large susceptibilities are advisable [2]. All these materials get saturated when set in a sufficiently large applied field. In our model the saturation of the soft ferromagnet is not considered. This may restrict ourselves to simulations where magnetic fields are not large. However, even in this case our model can give a first approximation.

CHAPTER 4

Magnetic Response of an Ideal Soft Ferromagnet

Before analyzing the mutual interaction between the SC and FM in the levitation case, it is important to understand the magnetic behavior of both SC and FM separated. The simplest case is to submit the FM or SC to a constant applied field. The SC response to a uniform applied field has already been studied for different geometries, such as slabs [17], or infinitely long bars with rectangular [88, 89, 90] or elliptical [91, 92] cross sections among others [27]. Also, much research has been done when the applied field over the SC is non-uniform [27, 93, 95]. However no systematic study of a FM under different applied fields has been carried out. In this chapter we analyze the magnetic response of the FM bar set in a uniform applied field or a field produced by PMs, i.e. non-uniform.

4.1 Uniform Applied Field

The simplest case is to consider a FM immersed in a uniform applied field. Studying this case not only allows us to understand the basic behavior of the FM but also to validate our results through analytical calculations. In our case of translationally symmetric ideal soft ferromagnet with rectangular cross section $a_{\rm FM} \times b_{\rm FM}$ there exists an analytical solution for the magnetic pole density distribution at its surface [96].

In our simulation, we consider a vertical applied field (perpendicular to $a_{\rm FM}$ side) $\mathbf{H}_{\rm e} = H_{\rm a}\hat{\mathbf{y}}$, where $H_{\rm a}$ is positive (see inset of Fig. 4.1). Figure 4.1 shows the distribution of surface magnetic pole density in the FM for several values of $b_{\rm FM}/a_{\rm FM}$ obtained by numerical calculations (symbols) and by the analytical expressions of the Ref. [96] (lines). We will refer to the different sides of the FM as top (T, $y = 0$), bottom (B, $y = -b_{\rm FM}$), left (L, $x = -a_{\rm FM}/2$) and right (R, $x = a_{\rm FM}/2$). For sake of simplicity only the pole densities of the upper right corner are plotted since, in the uniform applied field case, the pole distribution is horizontally symmetric and vertically antisymmetric

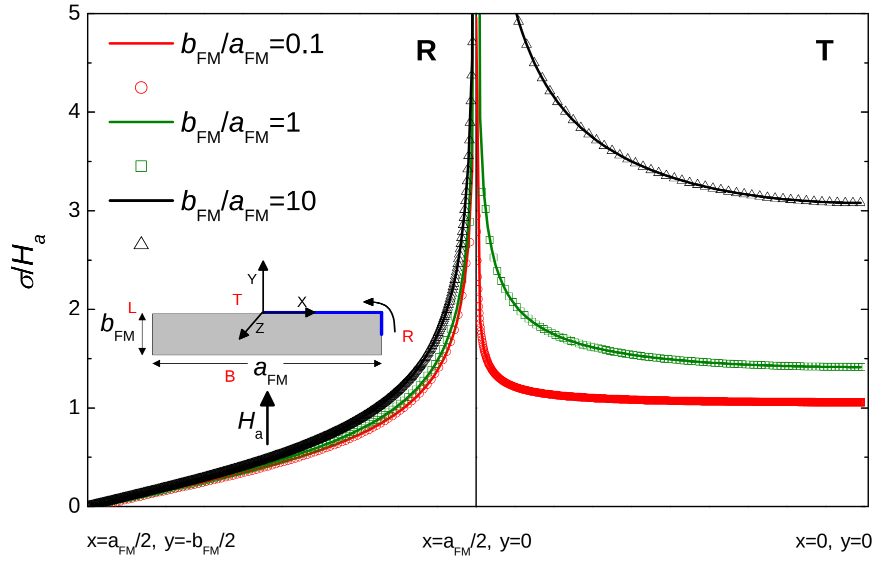

Figure 4.1: Comparison of the numerical (symbols) and analytical (lines) distributions of surface magnetic pole density of a FM set in a uniform applied field in the positive y direction for different ratios $b_{\rm FM}/a_{\rm FM}$. The inset shows an sketch of the considered system. Because of the symmetry, on the abscissa only the position of poles starting from the middle of the right side (R) to the middle of the top side (T) are represented counterclockwise (see blue line and the arrow in the inset).

with respect to the center of the FM ($x = 0$,$y = -b_{\rm PM}/2$). By comparing numerical and analytical distributions we can see that there is an excellent agreement between both, so the validity of our model in this limit is confirmed.

To make the total field **H** zero inside, the FM has to produce a negative vertical component of magnetic field in its interior. For this reason top and bottom sides must have positive and negative values of magnetic pole density, respectively. As can be seen in Fig. 4.1 these sides have a quasi-constant magnetic pole density at the regions far from the corners. This distribution creates a quasi-uniform vertical magnetic field in the central region in order to cancel the applied field. Near the corners however, a uniform magnetic pole density can no longer exist, otherwise a large horizontal field would be created in the interior region near the corners. Istead, the magnetic pole density increases in all the sides near the corners so that the horizontal field is completely canceled. Magnetic pole density diverges in the corners as can be seen in Fig. 4.1. Top and bottom sides diverge more rapidly than left and right side do, to make a net field in the -y direction. This is, if both sides were to diverge in the same way, their field would cancel mutually and therefore near the corners we would not have a zero total field.

The linearity of the FM is evidenced in Fig. 4.1 (see the normalization of σ). For the same FM, if the applied field is changed by a factor, the magnetic pole density at each point will be multiplied by the same factor. Since the applied field has the same value and direction at every point in the space, the magnetic pole density shape and value for a given applied field only depend on the aspect ratio $b_{\rm FM}/a_{\rm FM}$.

It is interesting to see that when $b_{\rm FM}/a_{\rm FM} << 1$ we can approximate the top and bottom sides in a region far from the corners as two uniformly charged infinite sheets. As said previously, these distributions produce a quasi uniform vertical field inside the sample. In this case, the magnetic pole density is $|\sigma| = H_a$ far from the corners (see red curve in Fig. 4.1). By contrast, when $b_{\rm FM}/a_{\rm FM} >> 1$ the absolute value of pole density of the top and bottom sides increases (black curve in Fig. 4.1) and tends to diverge. A simple explanation can be given looking at the central point of the FM ($x = 0$, $y = -b/2$). Since top and bottom sides are farther from this point when $b_{\rm FM}/a_{\rm FM}$ increases they must increase their magnetic pole density to make the same vertical field and cancel the applied field.

4.2 Permanent-Magnet field

We now move to a case where the applied field is not uniform, as for example the field created by a square-sectioned PM. The FM is placed just above the PM, which is uniformly magnetized in the y direction ($M_{\rm PM} = 7.95 \times 10^5$ A/m) and of side $a_{\rm PM} = 0.1$ m. In this way the bottom side of the FM is always in contact with the top side of the PM. In this example, as opposed to the case of a uniform applied field, the shape of the magnetic pole density depends on the ratios $a_{\rm FM}/a_{\rm PM}$ and $b_{\rm FM}/a_{\rm PM}$. Changing the side lengths of the FM while keeping its aspect ratio fixed changes the magnetic pole density shape because the field felt by each side also changes.

For the case of a square-sectioned FM with the same side as the PM ($a_{\rm FM} = b_{\rm FM} = a_{\rm PM}$) we find the magnetic pole distribution of Fig. 4.2(a) when the field is created by the PM (dashed line) compared to the response to a uniform applied field as in the previous section (line). In the case of the PM field, the surface pole density σ is normalized to $H_{\rm PM}$, which is defined as the magnetic field created by a PM of square cross section at the center of its surface perpendicular to the magnetization ($H_{\rm PM} \simeq 0.35M$). In the case of the uniform applied field, σ is normalized to H_a.

Figure 4.2(a) shows that, unlike the case with uniform applied field, all surfaces of the FM have positive density except the bottom one. This result can be understood by looking at Fig. 4.2(b) where the magnetic field lines produced by the PM are represented. In these profiles we find that the PM field tends to enter from the bottom side of the FM and exit through the rest of the sides.

Furthermore, the non uniformity of the PM field is responsible for the difference, in modulus, between the poles of the upper and lower surfaces. The shape of the pole distribution in the bottom surface also creates a negative horizontal field in the region $x > 0$ and positive in $x < 0$ which compensates the horizontal field produced by the PM in this surface [see Fig. 4.2(b)]. Finally, in Fig. 4.2(a) it can be seen that left and right surfaces have a large positive value of magnetic pole density near the PM ($y \approx -b_{\rm FM}$)

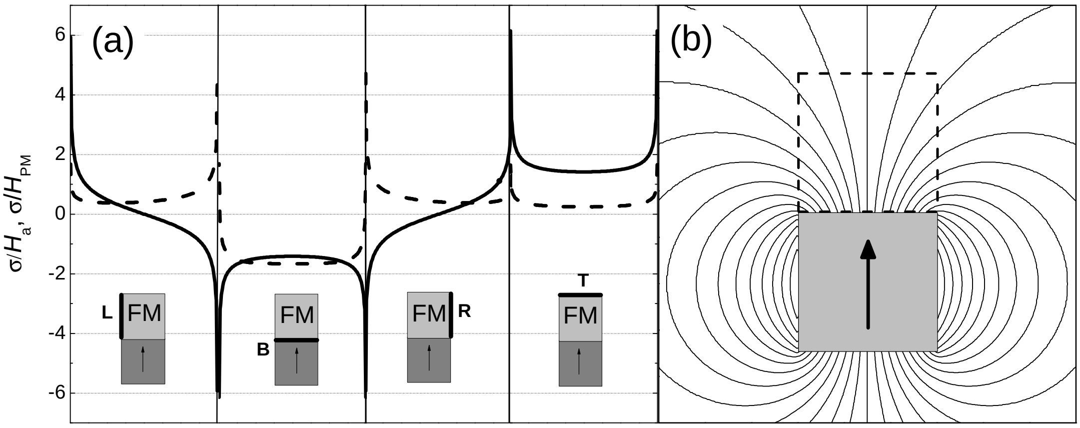

Figure 4.2: (a) Magnetic pole density of a square-sectioned FM of side $a_{\mathrm{FM}} = 0.1$ m set in a uniform applied field H_{a} (line) and in a field produced by a PM (dashed line). The PM has the same square cross section as the FM and is uniformly magnetized in the positive y direction with a saturation magnetization $M_{\mathrm{PM}} = 7.95 \times 10^5$ A/m. Magnetic pole densities are normalized to the applied field and H_{PM} (see text). The positions of magnetic pole density are represented on the abscissa starting from the left (L) surface of the FM and then following counterclockwise the bottom (B), right(R) and top (T) surfaces. (b) Calculated magnetic field lines produced by only the PM. The position of the FM is marked with a dashed square on top of the PM.

and this value decreases as the pole approaches to the top side because the horizontal field produced by the PM in the lateral sides is higher near the PM.

It should be noted that the sign and value of magnetic pole density at each point of the FM surface does not only depend on the external magnetic field at a particular point but on the field of all the other poles in that point. Analyzing the behavior of all magnetic poles can be cumbersome, therefore, we focus now on a single pole as representative of the overall response. In Fig. 4.3 we plot how the pole density at the center of the top side ($x = 0$) varies for three different heights of the FM (b_{FM}) as a function of its width (a_{FM}) being the PM kept always the same as before.

The dependence of the top central pole density with the FM width is, in general, very similar in the three studied heights, i.e., the pole density increases for small widths and it decreases when the FM is widened. For a fixed a_{FM}, the case of the thin FM ($b_{\mathrm{FM}}/a_{\mathrm{PM}} = 0.5$) is the one that provides larger central pole density since the thinner the FM is the stronger the field felt by the top side is because of its closeness to the PM.

When the width of the FM is very large ($a_{\mathrm{FM}} \to \infty$) the central magnetic pole density at the FM top side tends to zero for all b_{FM}'s. In fact, this result is extended to all poles of the upper surface. In the bottom surface, however, magnetic pole density at each point tends to double the value of the vertical component of the PM field at the particular point. One way to understand these results is to apply the image method [3, 97, 98], approximately valid in this limit because the FM volume and in particular its bottom surface are equipotential. The sum of the field produced by the PM and

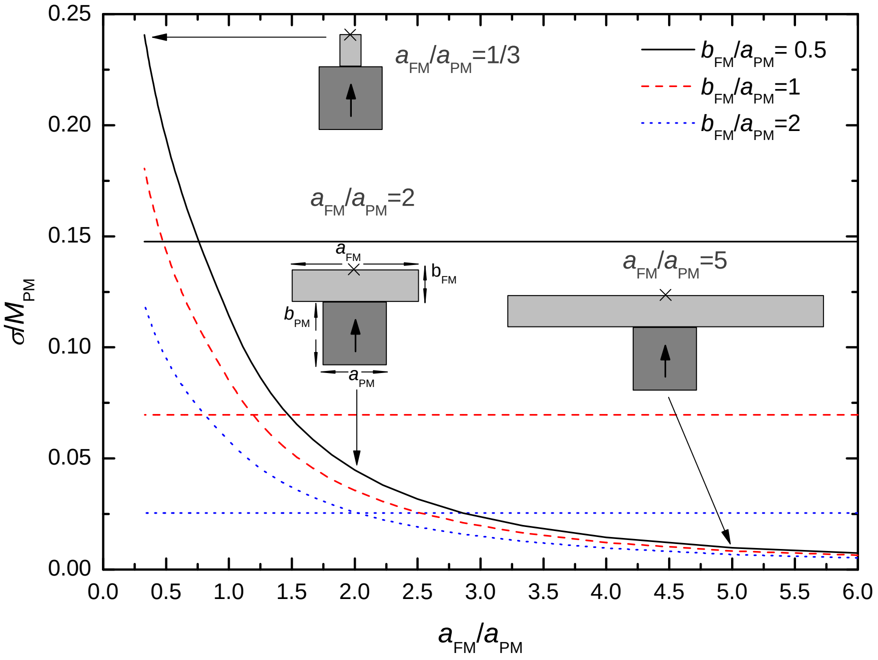

Figure 4.3: Magnetic pole density in the middle of the top side of the FM (marked with ×) as a function of the FM width ($a_{\rm FM}$) for different heights ($b_{\rm FM}$). Black line, red dashed line and blue dotted line represent the ratios $b_{\rm FM}/a_{\rm PM} = 0.5, 1, 2$, respectively. The corresponding straight lines represent the vertical field produced by the PM at the same points of the FM for the different curves $b_{\rm FM}/a_{\rm PM}$. The pole density σ is normalized to the PM magnetization $M_{\rm PM}$. The insets are sketches of the geometry for the curve $b_{\rm FM}/a_{\rm PM} = 0.5$ and three values of $a_{\rm FM}$.

its image will be the total magnetic field in the region $y \leq -b_{\rm FM}$ (under the FM). On the bottom side of the FM this sum is twice the field created by one of the PMs, and therefore σ is twice the vertical component of the PM field in this surface. In this limit, since the bottom side completely cancels the field produced by the PM for the region $y > -b_{\rm FM}$ (inside the FM and above it) there is no need for the top side to cancel any field and thus its pole density is zero.

By contrast, when the width of the FM is very small ($a_{\rm FM} \to 0$) for a fixed $b_{\rm FM}$ the magnetic pole density in the middle of the FM top surface diverges, because since the width shrinks, there is less surface able to create a field capable to cancel the PM field and so the top and bottom parts must have a large magnetic pole density.

FMs are added to PMs systems in order to modify the total magnetic field at some points without the need to increase the number of PMs. For this purpose in Fig. 4.3 it is also represented the magnetic field produced by the PM in the middle of the top side (straight black, red dashed and blue dotted lines for $b_{\rm FM}/a_{\rm FM}$=0.5,1,2, respectively). Figure 4.3 shows that, in the studied point, the set FM-PM generates more magnetic field than the case of a single PM when the width of the FM is small and the opposite happens when the width is large. Therefore, using a FM does not always enhance the magnetic field at a given point of interest. The shape of the FM is a crucial parameter. In particular, as the height of the FM increases the range of $a_{\rm FM}/a_{\rm PM}$ at which the magnetic field is enhanced also increases.

4.3 Two Permanent-Magnets Field

A more sophisticated case is when the applied field is produced by two square-sectioned PMs which are the same saturation magnetization $M_{\rm PM}$ and side $a_{\rm PM}$ as in the previous section. These two PMs are attached to the left and right sides of the FM (see inset of Fig. 4.4) with magnetizations in the positive and negative horizontal directions, respectively. The top sides of the three elements, PMs and FM are kept vertically aligned at $y = 0$. As it will be seen in the next chapter, this geometry is particularly interesting for levitation for it produces a large vertical and horizontal fields above it.

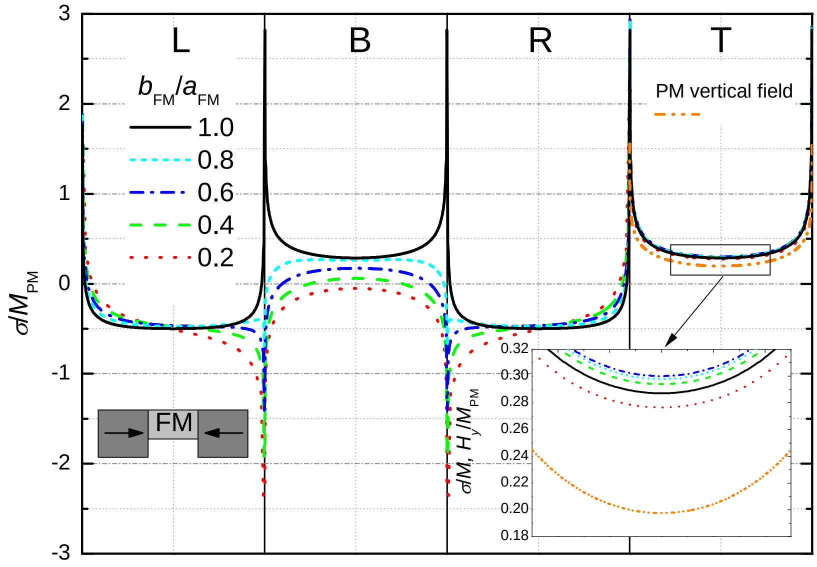

Figure 4.4: Distribution of magnetic pole density of a FM of width $a_{\rm FM} = a_{\rm PM}$ and different heights ($b_{\rm FM}$) set between two square-sectioned PMs with antiparallel magnetization in the x direction. On the abscissa the positions of the pole densities are represented starting from the left (L) surface and then the bottom (B), right (R) and top (T) surfaces, successively. The left inset shows an sketch of the guideway with $b_{\rm FM}/a_{\rm FM} = 0.6$. The right inset shows a zoom of the central region of the FM top surface. Orange dashed dot dot line is the vertical field produced by only the two PMs in the top side of the FM.

The magnetic pole density of the FM surface for different FM heights $b_{\rm FM}$ is shown in Fig. 4.4. In the case of the square FM (black line), the sign of the magnetic pole density is positive for the top and bottom sides (where the PM field tends to exit the FM) and negative in the left and right sides (where the PM field tends to enter the FM). The reason is that the FM tends to cancel the field perpendicular at each side.

According to this, the magnetic pole density in the top and bottom sides is maximum near the corners and minimum towards the middle ($x = 0$), as seen in Fig. 4.4, because the vertical component of the field produced by the PMs is larger near the corners. By contrast, the absolute value of magnetic pole density in the left and right sides takes its maximum in the middle of the side ($y = -b_{\mathrm{PM}}/2$) since the field perpendicular to this side produced by the PMs is maximum in this point and decreases towards the edges.

When the height of the FM changes, the field produced by the PMs over each point in the surface of the left, right and bottom parts also changes. More specifically, as the height of the FM decreases, two negatively charged regions appear in the bottom side close to the edges (see Fig. 4.4). For small heights, these regions extend and eventually occupy the entire lower surface. This behavior is consequence of three effects. The first one is that the vertical PM field begins to enter through the bottom surface when $b_{\mathrm{FM}} < a_{\mathrm{PM}}/2$, so the bottom part tends to be negative as the FM is shrunk. The second effect is due to the increase of the negative magnetic pole density on the lateral sides close to the bottom. This makes a positive vertical field over the region of the bottom part close to the left and right sides and thus more negative magnetic pole density builds up. Finally, the third effect comes from the positive top side, which tends to make a large negative vertical field over the bottom side as the height of the FM is shrunk. This makes the poles of the bottom side to decrease.

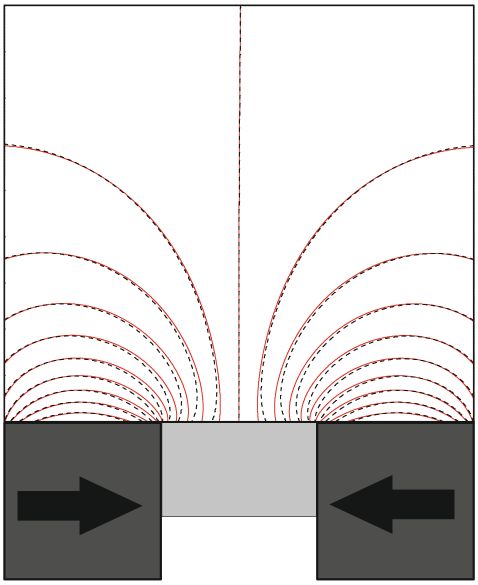

Figure 4.5: Magnetic field lines above the system of two square-sectioned PMs ($a_{\mathrm{PM}} = b_{\mathrm{PM}} = 0.1$ m) uniformly magnetized in opposite directions of x pointing each other (black dashed lines) and the same system with a FM width of a_{PM} and height of $b_{\mathrm{FM}}/a_{\mathrm{PM}} = 0.6$ set in the middle of the two PMs (red solid lines).

We find that the largest value of the magnetic pole density over the whole top side at a ratio $b_{\mathrm{FM}}/a_{\mathrm{PM}} = 0.66$ (Fig. 4.4). This is because the magnetic pole density over the top side depends mostly on the field produced by the bottom side over the upper one.

Particularly, it depends on the relative distance between top and bottom sides and the sign of the poles of the latter. As the FM height is shrunk from $b_{\mathrm{FM}} = a_{\mathrm{FM}}$, magnetic field over the top side produced by the bottom one increases because the latter side is positively charged. Therefore, the magnetic pole density increases in the top side (see inset of Fig. 4.4). However, the bottom side becomes eventually negatively charged and hence it produces a negative vertical field over the top side. This results in decreasing the magnetic pole density over the top side. The height at which the compensation of both effects occurs is $b_{\mathrm{FM}}/a_{\mathrm{PM}} \approx 0.66$.

Although the results of Fig. 4.4 are obtained for a fixed width ($a_{\mathrm{FM}} = a_{\mathrm{PM}}$), when different FM widths are considered, the largest values of the top pole density are also found for similar ratios $b_{\mathrm{FM}}/a_{\mathrm{PM}}$, being slightly higher or lower than 0.66 when the width increases or decreases, respectively.

Since the field at any point in the surface is perpendicular to it and with the value of the magnetic pole density, poles in the top surface indicate the vertical field just above the FM. Comparing to the vertical field produced by the two PMs (orange dashed dot dot curve in Fig. 4.4) we see that in fact any FM improves the vertical field above the guideway but for $b_{\mathrm{FM}}/a_{\mathrm{PM}} \approx 0.66$ this field is the highest. Magnetic pole density over the FM not only indicates the strength of the vertical field but of the horizontal field and its effect can be thought of as a uniformly charged sheet for a first approximation. We compare magnetic field lines with FM ($b_{\mathrm{FM}}/a_{\mathrm{PM}} \approx 0.66$) and without it in Fig. 4.5. As it can be seen, field lines are closer when the FM is present, indicating a larger field.

4.4 Chapter Summary and Conclusions

The magnetic response of a soft ferromagnetic bar has been studied in different applied fields. A remarkable agreement between our calculations and the previously analytical results has been found. In the cases of non-uniform applied field we have seen how by tuning the shape of the FM we can change the field at the FM surroundings.

Special focus has been given to the case of an ideal soft ferromagnet set between two permanent magnets. We have determined that when the two PMs are square-sectioned, a good option to maximize the field above them is to set a soft FM in between with height approximately 0.6 times the height of the PMs. This result can be useful when designing magnetic levitation trains based on superconducting levitation.

CHAPTER 5

Optimization of a Superconducting Levitation System

A good levitation system must be stable to horizontal and vertical displacements and achieve a large levitation force. Both effects have been studied experimentally by changing the size of the PMs or their orientation [63, 99, 106, 100, 101, 102, 103, 104, 107, 108], by modifying the SC arrangements and properties [59, 101, 105, 109, 110, 111, 112] or even by submitting the SC to different cooling processes [105, 106, 107, 108, 113, 114, 115, 116, 117, 118].

Equivalently, there are many theoretical studies where superconducting levitation is studied by changing the PM guideways [84, 93, 94, 95, 108, 119, 120, 121, 122, 123, 124, 131], or the bulk SC properties [84, 93, 95, 121, 122, 123, 124, 125, 126, 127, 128, 131]. Also the different cooling processes of the SC material [93, 95, 108, 120, 121, 123, 124, 127, 129] are a crucial point to take into account when designing good levitation systems.

In many theoretical works, soft ferromagnetic parts are not considered in the guideway [84, 119, 120, 121] whereas in others are modeled as passive non-interacting parts [108, 124]. This is, they consider that the SC behavior is affected by the FM but not the opposite way. In this chapter we study a practical case of levitation in which the soft ferromagnetic material is an ideal soft ferromagnet able to mutually interact with the SC. We optimize the shape of the system so that to achieve large levitation and complete stability.

5.1 Geometry for High Levitation Force

When optimizing the levitation force and stability of a magnetic levitation system there are two important factors: the physical properties of the PMs, FMs and SCs (e.g. saturation magnetization and critical-current density) and their geometry (width and height of each magnetic element). In this chapter we fix the physical properties and vary the geometrical ones in order to find the largest levitation force for a complete stability.

In the guideway we consider a FM of $a_{\mathrm{FM}} \times b_{\mathrm{FM}}$ cross section set between two uniformly magnetized PMs of side $a_{\mathrm{PM}} \times b_{\mathrm{PM}}$ each in the horizontal and vertical directions, respectively (see Fig. 5.1). The two PMs are uniformly magnetized in the horizontal direction pointing to the FM, i.e. the PM at $x < 0$ is magnetized in the positive x direction (see Fig. 5.1) whilst the PM at $x > 0$ in the negative one. The saturation magnetization is assumed $M_{\mathrm{PM}} = 7.95 \times 10^5\,\mathrm{A/m}$, or equivalently $\mu_0 M_{\mathrm{PM}} = 1\mathrm{T}$ (typical for rare earth PMs [130]). Several theoretical [93, 119, 121, 124, 131] and experimental [58, 59, 60, 63, 66, 67, 100, 103, 105, 106, 107, 132] studies show that this guideway arrangement is a good candidate to achieve large levitation force on the SC placed above.

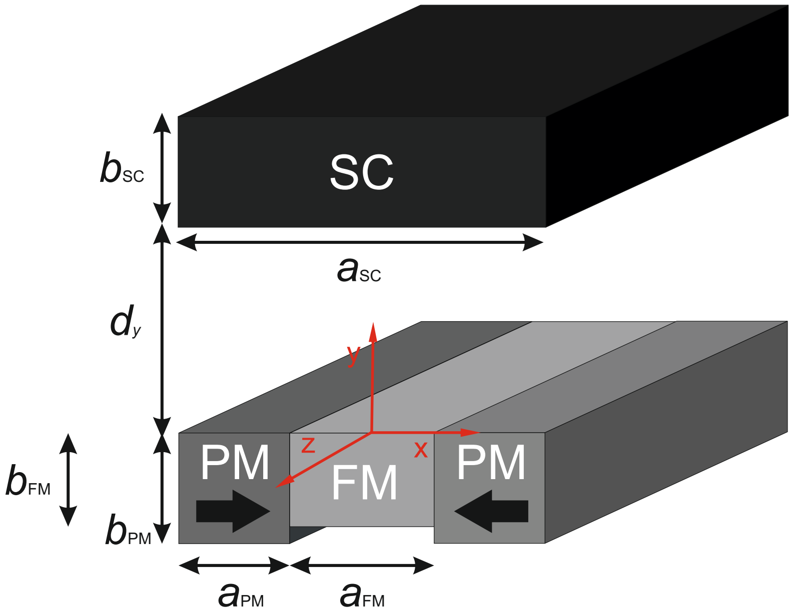

Figure 5.1: Sketch of the levitation system. A FM is set between two PMs with their top sides aligned. The arrows inside the PMs indicate the direction of their magnetization. The SC is set above the guideway at a vertical distance d_{y}.

The levitating SC of cross section $a_{\mathrm{SC}} \times b_{\mathrm{SC}}$ is set above the guideway being its center of the bottom side at a vertical distance d_{y} and horizontal distance d_{x} with respect to the origin (center of the top side of the FM). A constant critical-current density of $J_{\mathrm{c}} = 3.7 \times 10^5\,\mathrm{A/m}^2$ is assumed which corresponds to typical values found in experiments [102, 103]. Throughout this chapter the SC will occupy the total width of the guideway ($a_{\mathrm{SC}} = 2a_{\mathrm{PM}} + a_{\mathrm{FM}}$), in this way, for the same height of the SC the levitation force is larger [121]. Also, in all calculations the SC will be zero-field cooled (ZFC) at a large distance ($d_{\mathrm{y}}/b_{\mathrm{PM}}$=5) from the system of PMs and FM.

5.2 General Effect of a Soft Ferromagnet in Levitation

To show the effect that introducing a FM produces to the vertical force we study the case of square PMs of side $b_{\rm PM} = a_{\rm PM} = 0.05$ m and a SC of rectangular cross section $3b_{\rm PM} \times b_{\rm PM}$. In order to maximize the field above the guideway, the FM height is set to $b_{\rm FM} = 0.6b_{\rm PM}$ (see Sec. 4.3) whereas its width is the same as the PM $a_{\rm FM} = a_{\rm PM} = b_{\rm PM}$.

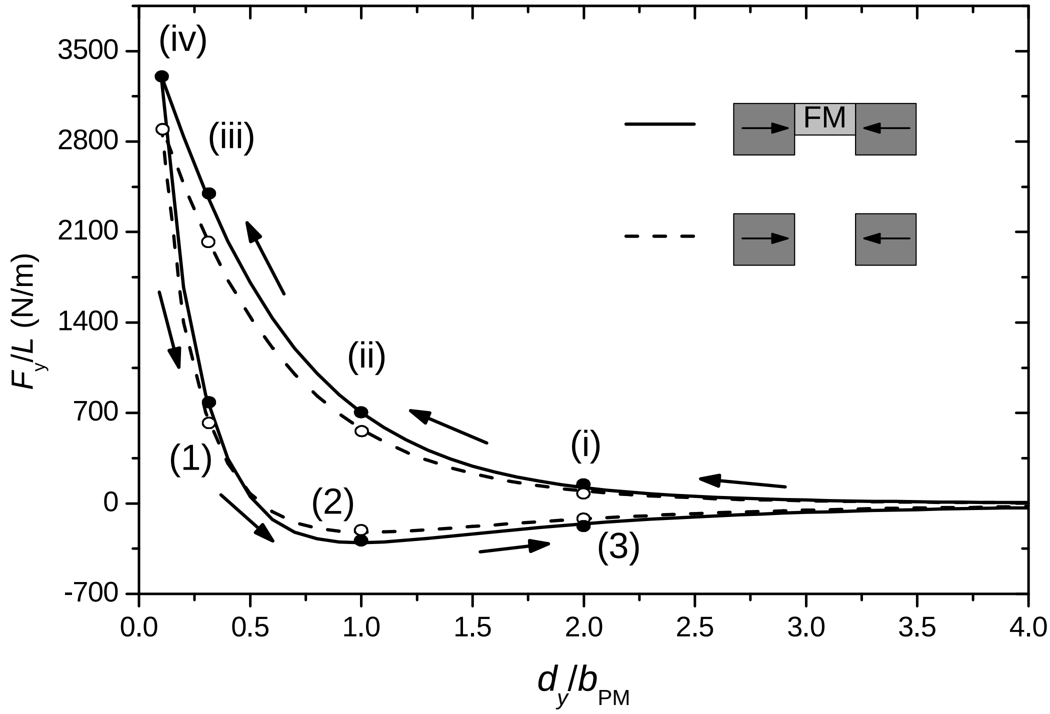

Figure 5.2: Levitation force per unit length over the SC of cross section $3b_{\rm PM} \times b_{\rm PM}$ as a function of the vertical distance $d_{\rm y}$ for the case of a guideway consisting on two square-sectioned PMs ($b_{\rm PM} = 0.05m$) separated a distance $b_{\rm PM}$ (dashed line) and the same PMs with a FM of height $b_{\rm FM} = 0.6b_{\rm PM}$ in between (solid line). Open and full dots indicate the force for the guideway with FM and without it, respectively. (i,ii,iii,iv) mark the force at the distances $d_{\rm y}/b_{\rm PM}$=2,1,0.3,0.1 for the descending curve and those labeled as 1, 2 and 3 indicate the force at $d_{\rm y}/b_{\rm PM}$=0.3,1,2 in the ascending one. Arrows indicate the SC direction of movement.

After cooling the SC at the ZFC point, it is descended towards the guideway (decreasing $d_{\rm y}$) up to a distance $d_{\rm y}/b_{\rm PM} = 0.1$ and then ascended again. Such movement is performed keeping the SC always centered with respect to the guideway ($d_{\rm x} = 0$). The resulting levitation force undergone by the SC during this process is represented in Fig. 5.2 for the cases of the guideway with FM and without it.

Levitation force increases in the descending process, a fact that can be explained by the current distribution in the SC and the field of the guideway over it. Currents begin penetrating the SC in order to cancel the field variation in its interior [see Fig. 5.3 (a)]. This penetration is larger when the SC is closer to the guideway yet the field over the SC increases. For the same reason, the bottom part of the SC has always a deeper penetration of currents although currents also appear in the top part due to demagnetizing effects [84]. In order to cancel the vertical field in the SC interior currents are positive for $x > 0$ and negative otherwise as can be seen in Fig. 5.3 (a). The horizontal field over the SC also increases as the SC gets closer to the guideway being always positive for $x > 0$ and negative otherwise (see Fig. 4.5 in the preceding chapter). The interaction of this horizontal field with the penetrated currents leads to a positive levitation force according to Eq. (3.9).

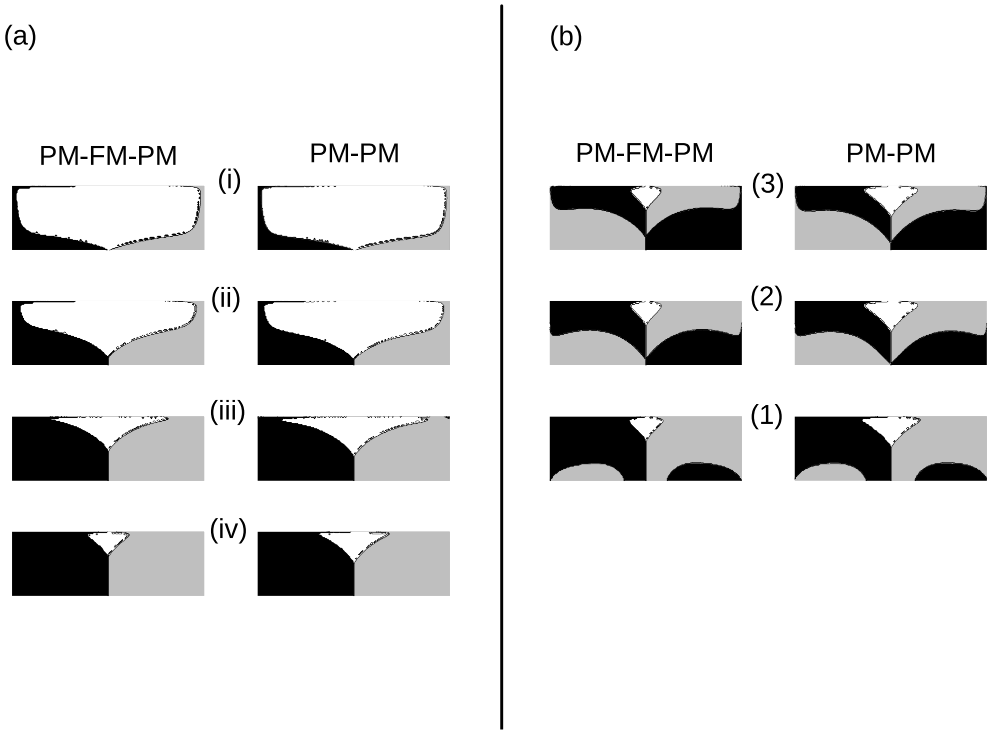

Figure 5.3: Current density profiles in the SC for the descending process (a) and the ascending one (b) for the cases of the guideway with FM (left column) and without FM (right column). Gray (black) represents positive (negative) current density in the z direction. i, ii, iii, vi in (a) mark the vertical distances $d_{\mathrm{y}}/b_{\mathrm{PM}} = 2, 1, 0.3, 0.1$, respectively whereas 1, 2 and 3 in (b) are $d_{\mathrm{y}}/b_{\mathrm{PM}} = 0.3, 1, 2$, respectively. These points are the same as shown in Fig. 5.2.

In the ascending process currents penetrate in opposite sign as compared to the descending one (see Fig. 5.3). This is consequence of a negative vertical field variation over the SC in this movement. These new currents interact with the field of the guideway resulting in a decrease of the levitation force as Fig. 5.2 shows.

The levitation force loop is wider for the case of the guideway with FM as shown in Fig. 5.2. In fact, although it has not been shown here, for a fixed FM width ($a_{\mathrm{FM}} = b_{\mathrm{PM}}$)

any FM would increase the levitation force. However, the height of the FM that gives the largest levitation force is $b_{\rm FM}/b_{\rm PM} = 0.6$. This is a consequence of what is shown in Sec. 4.3, both vertical and horizontal fields above the guideway are maximum for this FM shape. In our case this leads to a deeper penetration of currents in the SC (see Fig. 5.3) and a larger horizontal field over the penetrated region therefore forces become larger.

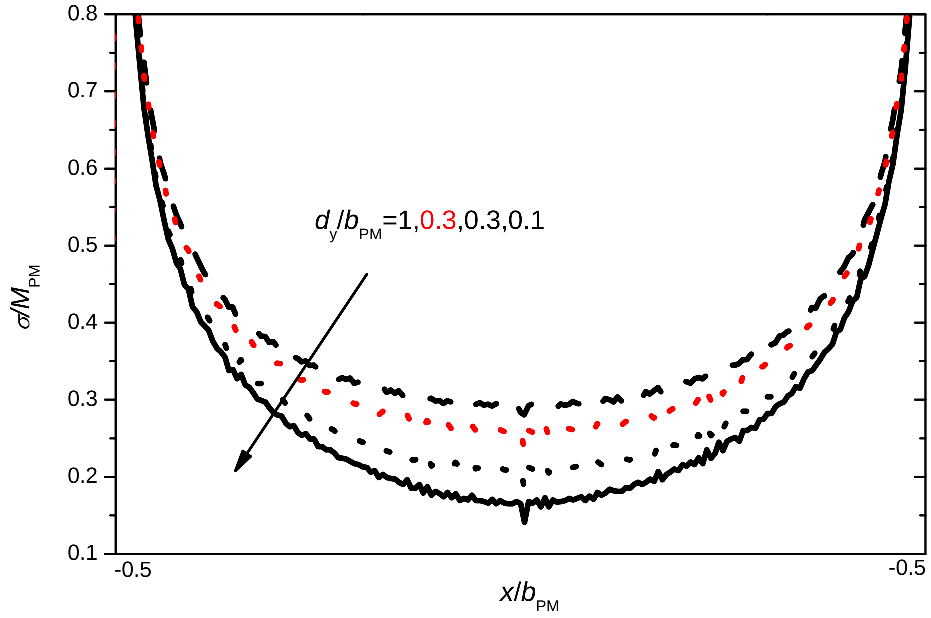

Figure 5.4: Magnetic pole density of the top side ($y = 0$) of the FM with cross section $b_{\rm PM} \times 0.6 b_{\rm PM}$ for three separations of the SC and the FM in the descending (black lines) process $d_{\rm y}/b_{\rm PM} = 1, 0.3, 0.1$ and one at $d_{\rm y}/b_{\rm PM} = 0.3$ in the ascending one (red). These vertical distances correspond to ii,iii,iv and 1 in Fig. 5.2.

During the ascending and descending processes the FM gets affected by the field of the SC and changes its magnetic pole density distribution. Initially, in the descending process, the FM is only affected by the field of the two PMs resulting in a magnetic pole density distribution as shown in the blue dash-dotted line of Fig. 4.4. When the SC gets closer to the guideway, their currents create a large negative vertical field over the FM making the top side of the latter to reduce its poles (see Fig. 5.4). In this way the FM is getting demagnetized and makes a weaker field above the guideway.

When the SC is ascended, the magnetic pole density distribution at the top side increases compared to the same vertical separation in the ascending process. This behavior is depicted in Fig. 5.4 where it is shown that magnetic pole density at the top side is larger in the ascending process at a distance $d_{\rm y}/b_{\rm PM} = 0.3$. This is a consequence of the penetration of opposite sign currents in the SC (see Fig. 5.3 (b)) that makes a weaker negative vertical field over the FM. Eventually, when the SC is ascended a sufficiently large distance ($d_y/b_{PM} \approx 2$), currents do not affect the FM and magnetic pole distribution is only due to the PMs field.

5.3 Stability and Minor Loops

Stability for our geometry without FM has already been studied [115, 120, 133]. This section is focused on the influence of the FM on stability.

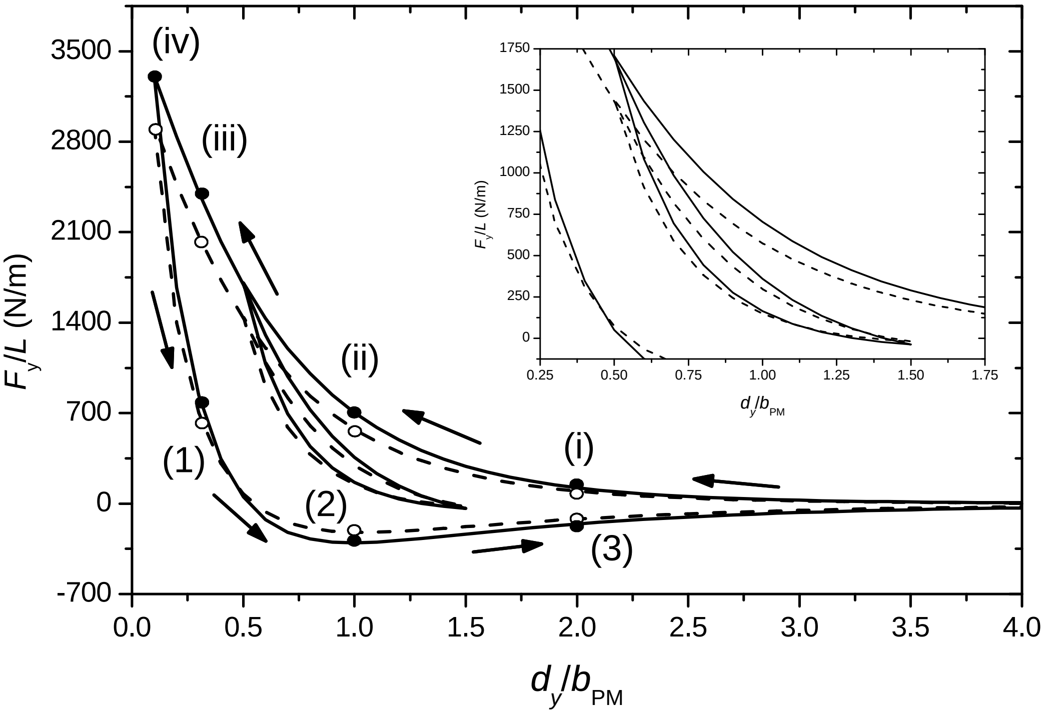

Figure 5.5: Same as Fig. (5.2) but with a vertical minor loop starting at $d_y/b_{PM} = 0.5$ and finishing at $d_y/b_{PM} = 1.5$ in the descending curve. The inset shows a zoom of the minor loop.

A vertical minor loop in the descending branch is performed as follows. The SC is descended from the cooling point to a given distance d_{y1} and then firstly it is ascended to a vertical distance $d_{2y} > d_{1y}$ and then descended again to d_{y1}. Considering the geometry of the previous section, we perform a vertical minor loop starting at $d_{y1}/b_{PM} = 0.5$ and ending at $d_{y2}/b_{PM} = 1.5$ as Fig. 5.5 shows. Two features must be noticed here. The first is that the vertical minor loop is closed, this is, the vertical force at the beginning and end of the loop is the same in spite of the hysteretic process of the minor loop, a fact well known from other calculations [84] without FM. When adding a FM this behavior does not change and the starting and ending point present the same force as well as current profile in the SC and magnetic pole density in the FM. This is a consequence of the linearity of the FM. The second feature is that, as above, the guideway with FM makes a wider loop as a consequence of the larger field and deeper penetration of currents. After the minor loop (see inset Fig. 5.2) the descending and ascending processes are the same as if the minor loop had not been performed.

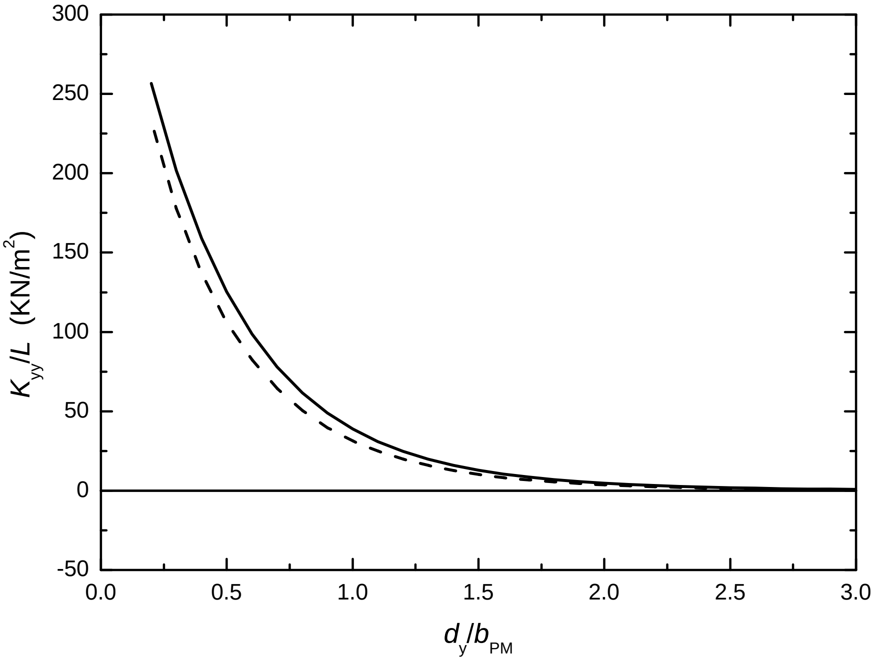

Figure 5.6: Vertical stiffness per unit length as a function of the vertical separation for the case of a guideway composed of two square-sectioned PMs of side $a_{\rm PM} = b_{\rm PM} = 0.05$m (dashed line) and the same guideway with a FM of width $a_{\rm FM} = b_{\rm PM}$ and height $b_{\rm FM} = 0.6 b_{\rm PM}$ (solid line). The SC is $3b_{\rm PM} \times b_{\rm PM}$ cross-sectioned. A reference for zero vertical stiffness is represented by the straight line.

An interesting quantity to study is the vertical (horizontal) stiffness defined in Eqs. (3.13) and (3.14) which measures the change of vertical (horizontal) force due to a small vertical (horizontal) displacement. In our simulations we study the vertical stiffness at a given vertical distance $d_{\rm y}$ by descending the SC horizontally symmetric with respect to the guideway ($d_{\rm x} = 0$) and then ascending the SC a small distance $\Delta d_{\rm y}/b_{\rm PM} = 0.2$. The resulting vertical stiffness is shown in Fig. 5.5. In this particular geometry the SC is always vertically stable. This result can also be understood by looking at the initial slope of the minor loop in Fig. 5.2. When ascending the SC in the descending branch levitation force decreases because currents with opposite sign start to penetrate the SC. This current penetration (and field over the currents) is even larger when the FM is in the guideway resulting in a larger stability at all the vertical distances as shown in Fig. 5.6.

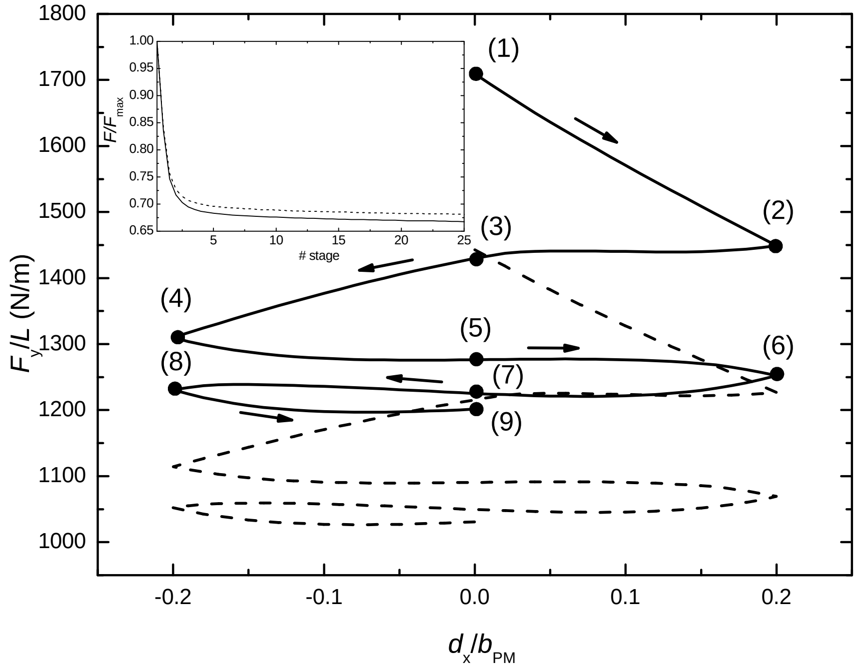

Figure 5.7: Levitation force per unit length for two consecutive minor loops with amplitude $|\Delta d_\mathrm{x}/b_\mathrm{PM}| = 0.2$ at a constant vertical distance $d_\mathrm{y}/b_\mathrm{PM} = 0.5$. Solid line and dashed line correspond to the guideway with and without FM, respectively. Arrows indicate the direction of SC movement and levitation force at distances $d_\mathrm{x}/b_\mathrm{PM} = -0.2, 0, 0.2$ are marked with points. In the inset a plot of the force at $d_\mathrm{x}/b_\mathrm{PM} = 0$ normalized to initial levitation force is represented as a function of the loop number.

In real cases horizontal displacements of the SC around its equilibrium point may exist. To study the SC behavior in this case horizontal minor loops are performed. For our minor loop, the SC is descended to a working distance $d_\mathrm{y}/b_\mathrm{PM} = 0.5$, and then is horizontally displaced to $d_\mathrm{x}/b_\mathrm{PM} = 0.2, -0.2, 0$ one after the other. In general, during this process, the SC undergoes a torque that makes it rotate [66]. However in our simulations the SC is forced to make the horizontal displacement without rotating. Vertical force for two consecutive minor loops is shown in Fig. 5.7. Levitation force decreases monotonically when the SC is horizontally displaced, a fact observed in several experiments [59, 106, 115]. This is consequence of the asymmetric current profiles in the SC. When the SC moves horizontally, it undergoes a non horizontally symmetric magnetic field variation which turns out into a non symmetric current profile as can be seen in Fig. 5.8(a). Magnetic field variation is the same but opposite in sign if the SC moves from the left (negative x) to the center ($d_\mathrm{x} = 0$) as compared from the right (positive x) to the center. Therefore current profiles at the center have similar shapes

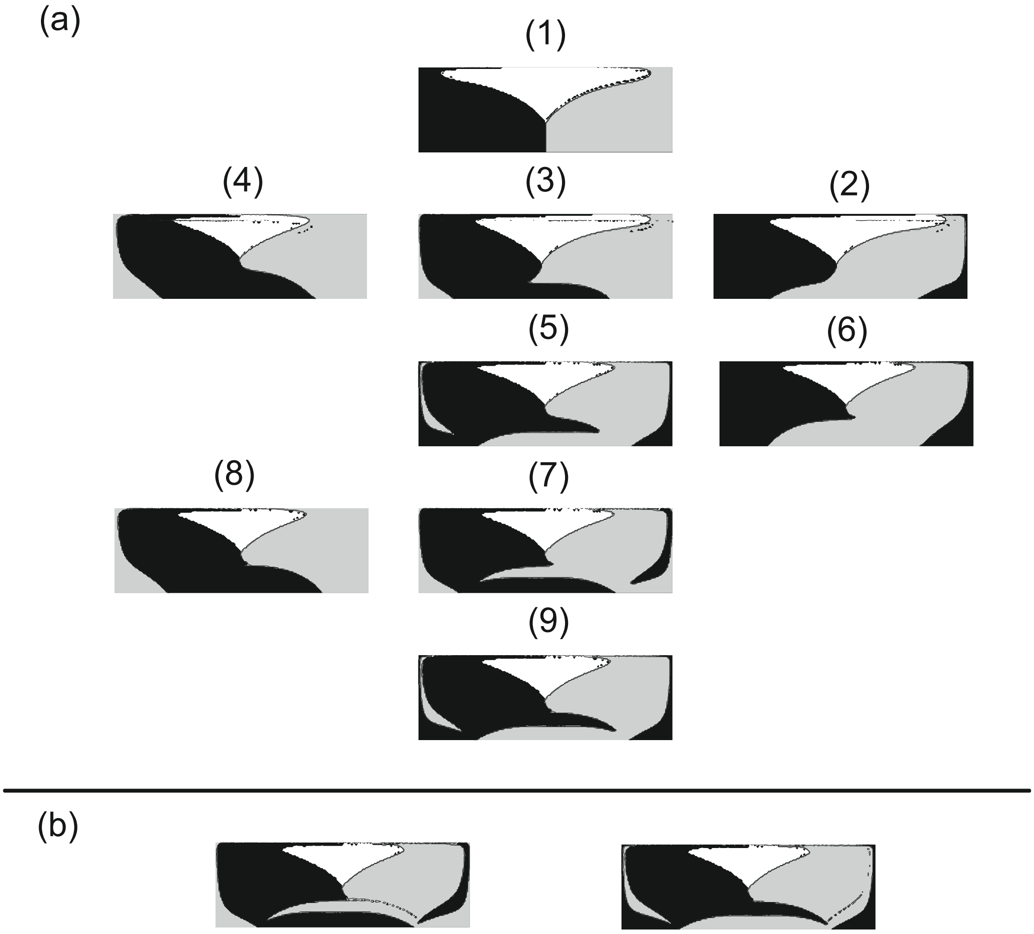

Figure 5.8: Current profiles in the SC for a minor loop at $d_{\mathrm{y}}/b_{\mathrm{PM}} = 0.5$ with amplitude $|\Delta d_{\mathrm{x}}/b_{\mathrm{PM}}| = 0.2$ when the guideway has the FM. Numbers in (a) correspond to the marked points in Fig. 5.7. Left (right) current profile in (b) is the current distribution at $d_{\mathrm{x}}/b_{\mathrm{PM}} = 0$ coming from negative (positive) x direction after 25 horizontal minor loops.

[see for instance profiles 7 and 9 in Fig. 5.8(a)] but changing the asymmetric induced currents by opposite sign and making a reflection at $y = 0$ axis.

Current profiles have a deeper penetration of asymmetric currents in the SC as it passes through $d_{\mathrm{x}} = 0$. However after several minor loops this current profile saturates (see Fig. 5.8) and therefore levitation force also saturates. This can be seen in the inset of Fig. 5.7 where the normalized levitation force at $d_{\mathrm{x}} = 0$ is plotted as a function of the number of minor loops.

Comparing the cases of the guideway with FM and without it, the observed behavior is the same, however force is always larger for the case of having a FM because of the deeper penetration of currents. The decay of the force at $d_{\mathrm{x}} = 0$ is also larger for the guideway with FM for the same reason.

Our levitation system is not always stable to horizontal displacement as opposed to

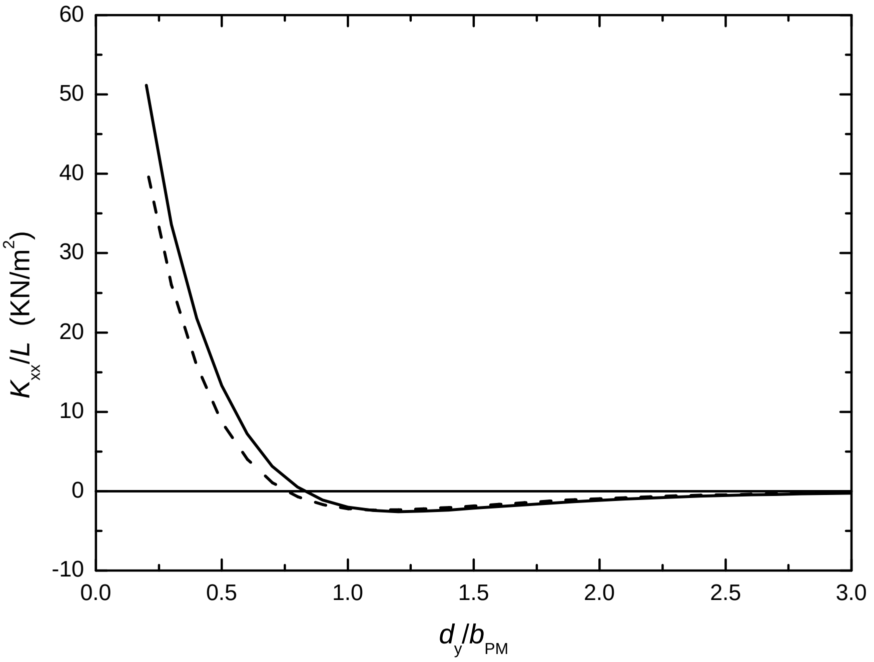

Figure 5.9: Horizontal stiffness per unit length as a function of the vertical separation d_y for the cases of the guideway of two PMs (dashed line) or the same guideway with a FM in the middle (line).

the vertical ones. In Fig. 5.9 we have plotted the horizontal stiffness as a function of the vertical separation between the guideway and the SC. Each point of both curves has been calculated descending the SC from ZFC vertically aligned with the guideway ($d_x = 0$) up to each distance d_y and then making a small horizontal displacement of $|\Delta d_x| = 0.2$. This figure shows that when the guideway consists of two PMs the system becomes unstable for distances $d_y/b_{PM} \gtrsim 0.75$. The addition of a FM makes the system to become stable at a smaller distance d_y and enhances the stability at the distances where it was already stable.

5.4 Optimization of the Ferromagnet Width

In Sec. 4.3 an optimized value for the FM height was found to be $b_{FM} = 0.6 b_{PM}$. In this section we show which is the optimum width of the FM for a larger levitation force.

In Fig. 5.10 we show the levitation force at a vertical distance $d_y = b_{PM}/2$ for a SC covering the entire width of the guideway ($a_{SC} = 2b_{PM} + a_{FM}$) for different widths of the FM (a_{FM}). For large and small widths, the levitation force decrease and has a maximum in between. This behavior is the result of two effects, the closeness of the PMs and the SC volume. By reducing the FM width the magnetic field above the guideway increases

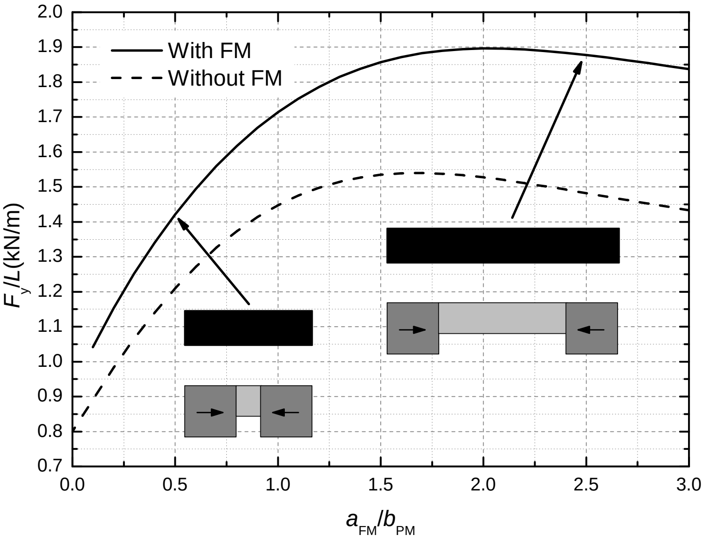

Figure 5.10: Levitation force per unit length as a function of the FM width at a vertical distance $d_y = b_{PM}/2$ for the case of a guideway composed of two square-sectioned PMs of side $b_{PM} = a_{PM} = 0.05$m (dashed line) and the same PMs with a FM of height $b_{FM} = 0.6b_{PM}$ in between (solid line). The SC has a cross section of $(2b_{PM} + a_{FM}) \times b_{PM}$, i.e. it occupies the total width of the PMs-FM guideway as shown in the two insets representing the cases $a_{FM}/b_{PM} = 0.5$ and $a_{FM}/b_{PM} = 2.5$.

because the field of the two PMs sum up. This effect makes the force to increase since the penetration of currents is larger and so it is the horizontal field over them. However, as we decrease the FM width, the SC volume is also reduced and therefore less currents are able to penetrate. This last effect makes the force to decrease. Compensation of both occurs at the maximum shown in Fig. 5.10 in which the SC volume is not sufficiently small whereas the PMs are close enough to make a large field.

As expected, levitation force is larger with FM due to the increase of magnetic field above the guideway as can be seen comparing the two curves in Fig. 5.10. It is noteworthy that the effect of the FM is larger for large FM widths and it decreases as the FM is shrunk. This result may not be intuitive for small FM widths because magnetic pole density on the top side of the FM tends to diverge. However, top side surface tends to zero which in turn results in a finite magnetic field produced by the FM. On the contrary, in the limit of large FM widths the force tends to a finite value because the SC tends to be penetrated only in the regions above the PMs.

Another difference is observed between the two cases, the maximum in Fig. 5.10 occurs at larger a_{FM} when the FM is present. A fact that can be explained by the increase in horizontal field due to the FM which makes the compensation to occur for larger FM widths. As before, this enhancement of horizontal field and current penetration makes the system with FM to be more stable. It is indeed always vertically stable for any FM width but it becomes horizontally unstable for widths $a_{FM}/b_{PM} > 1.5$.

5.5 Modifying the Permanent Magnet Width

The study in the previous section considered only square-sectioned PMs, but changing the PM shape makes the magnetic field distribution and intensity to be different. As in previous section, we consider here that the SC occupies the total width of the guideway. In particular one may think on tunning the levitation force as a function of the geometrical parameters of the PMs a_{PM} and b_{PM} to find an even larger levitation force. In this section the width of the PMs (a_{PM}) is changed keeping its height $b_{\mathrm{PM}} = 0.05$ m constant to see how the maximum of force changes as a function of the FM width a_{FM}. The FM height is kept to its optimized value b_{FM}=$0.6 b_{\mathrm{PM}}$.

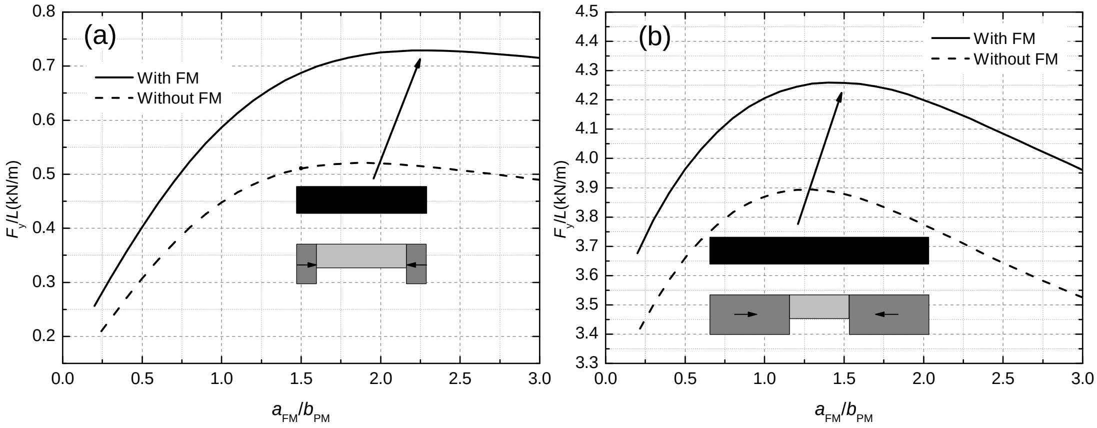

Figure 5.11: Same as Fig. 5.10 but the PMs width set to $a_{\mathrm{PM}} = b_{\mathrm{PM}}/2$ in (a) and $a_{\mathrm{PM}} = 2b_{\mathrm{PM}}$ in (b) where $b_{\mathrm{PM}} = 0.05$m.

In Figs. 5.11(a) and 5.11(b) the levitation force is plotted as a function of the FM width for the case of $a_{\mathrm{PM}} = b_{\mathrm{PM}}/2$ and $a_{\mathrm{PM}} = 2b_{\mathrm{PM}}$, respectively. We observe that the maximum of force in the curves of different a_{PM} is shifted. That is, the maximum occurs for large a_{FM} when a_{PM} is small and vice versa. This is so because for large a_{PM} the horizontal field in the central part above the PM is smaller than when a_{PM} is small; for this reason when a_{PM} is large it is necessary to decrease the gap between the PMs to increase the horizontal field above them so the compensation occurs at a smaller a_{FM}. The levitation force increases as the PM width is larger and the peak of maximum force in the case of having FM has a value of approximately $2 \times a_{\mathrm{PM}}/b_{\mathrm{PM}}$. The stability has been also analyzed and is found that the system is always vertically stable and the horizontally stable region is enhanced when the FM is added to the guideway.

5.6 Chapter Summary and Conclusions

Throughout this chapter the basics of levitation with hard type II SC have been studied for a guideway consisting on two PMs and the same PMs with a FM in the middle. This system is always vertically stable and becomes horizontally unstable for vertical distances smaller tan $d_{\mathrm{y}}/b_{\mathrm{PM}} < 1.5$. Vertical minor loops are closed but not so horizontal minor loops. In both cases the magnetic history is the responsible of these behaviors.

We have quantitatively shown that by adding a soft ferromagnetic material in the guideway of the levitating system, the levitation force increases and both the vertical and horizontal stabilities are slightly enhanced. The reason is that the soft ferromagnet guides the magnetic field of the PMs to produce a larger field in the supercoductor which makes it to be more penetrated by currents. The combination of guiding the magnetic field and increasing the penetration results in an increased levitation force. It is also possible to increase the levitation force by increasing the permanent magnet width; this implies a reduction of the ferromagnetic width to achieve a larger levitation force.

Even though the levitation performance is better when increasing the PM volume this results in an increase of costs. PM volume can be reduced by adding soft ferromagnetic parts to the guideway which help to guide the magnetic field towards the SC. The results presented in this chapter may be useful for better understanding the role that a soft ferromagnetic material plays in the guideway of a linear magnetic levitation system based on levitating superconductors.

Part II

Modeling Magnetism at the Nanoscale: Application to Exchange Bias and Thin Soft Ferromagnets

Over the past few decades there has been an active research on magnetic properties at the nanoscale [134, 135, 136]. Part of this interest was boosted by the magnetic recording industry [134, 137, 138] since magnets produce strong magnetic fields that can be used to store information. In this introduction we briefly review the applications of nanoscale magnets and their foreseeable future.

Conventionally digital information in computers was stored in hard disk drives typically consisting on a polycrystalline thin film media [139]. Small regions of this material were in-plane uniformly magnetized using a inductive write head such as a small electromagnet. In the boundary separating two uniformly magnetized regions a stray field resulting from the magnetic poles generated appears. Depending on the magnetization directions this stray field has two out-of-plane field directions (a bit of information) that can be read with a magnetic field sensor. The key to improve this technology is to reduce the signal-to-noise ratio and increase both, the read/write speed and the information density (number of bits per area of magnetic media). Hard disk drives have the advantage of storing information even when the power is cut (non-volatile devices) but reading/writing process can be considered slow because the read/write tip has to be mechanically moved to read different zones of the disk.

An important breakthrough, the discovery of giant magnetoresistance (GMR) [140] made possible to construct much more efficient magnetic field sensors [141] at the nanoscale (read heads using GMR were available in 1997) therefore reducing the read error while enabling to increase the information density. GMR [142] is observed in multilayered thin film structures composed of alternating ferromagnetic and non-magnetic conductive layers. In these systems the in-plane or out-of-plane resistance is very low when the ferromagnetic layers have the same magnetization direction whereas very large when they are oppositely magnetized. In many cases the multilayered film consists of two ferromagnetic layers, one of which (free layer) can be magnetized in two directions whereas the other (pinned layer) has magnetization direction fixed due to exchange coupling with an antiferromagnetic (AFM) layer. The free layer can change its magnetization direction depending on the field that undergoes therefore changing the resistance of the multilayer and enabling the sensing of small magnetic fields.

GMR effects also provide new ways to store information [143, 144]. The idea is to put several multilayers and magnetize the free layer of each in the desired direction so that to store a bit of information. Commonly these multilayers presenting GMR are stacks of ferromagnetic-metal-ferromagnetic (spin valves) or ferromagnetic-insulator-ferromagnetic (magnetic tunnel junctions). These devices, where the information is stored by the orientation of magnets and are of random access nature (the time for accessing an individual bit is independent of its position), are called magnetic random access memories (MRAM). MRAMs [2] are also non volatile and since they do not need moving parts to store and read information they are expected to be much faster in the reading/writing process than hard disk drives.

The first commercial MRAM was released in 2006 and is expected to replace random access memories widely used in computation today. Research is now focused not only on the change of magnetization direction due to a magnetic field but on spin polarized currents. It was theoretically demonstrated [145, 146] and experimentally validated [147] that a polarized current carries a torque that can be transferred to the magnetic material making possible the switching of magnetization without magnetic fields. This effect, known as the spin transfer torque effect [148] (STT) is complementary to the GMR in the sense that the first changes the magnetization with polarized currents whereas the second changes the flow characteristics of this current due to the magnetization. This new effect, STT, may be applicable in other types of magnetic storage devices, such as the magnetic racetrack memory [149].

In this part of the thesis we develop a model to describe the magnetic behavior of nano-sized magnetic structures in the first chapter. This model is applied to control the magnetization of a magnetic dot based on a magnetic vortex structure in the second chapter. In the last chapter we extend the model to introduce the effect that an anti-ferromagnetic material exchange coupled to the ferromangetic layer can produce to the ferromagnetic layer.

CHAPTER 6

Micromagnetic Model

Micromagnetics is a theory describing the magnetization distribution of ferromagnetic materials at the intermediate length scale between magnetic domains and crystal lattice sites (from tens of nanometers to few micrometers). In this chapter we introduce a procedure to obtain the quasistatic magnetization distribution of a ferromagnetic body of arbitrary shape.

6.1 Micromagnetic Energy Density and Assumptions

As pointed out in the basic concepts part (Chapter 1), ferromagnetic materials are formed by a discrete distribution of atomic spins or magnetic moments. These magnetic moments interact locally by the exchange interaction and globally by magnetostatics. The goal of micromagnetics is to describe this problem in a continuum approximation as opposed to discrete for an effective mesoscopic theory.

The first approximation is to describe the exchange energy in a continuum [1, 9, 10] by assuming classical spins which vary in direction a small amount from one to the other. A continuous expression of the exchange energy is obtained where involving no longer magnetic moments but their average, i.e. magnetization. This theory makes compatible exchange energy with the Maxwell's theory of electromagnetism in which one deals with averaged physical quantities, such as permeabilities or susceptibilities [10]. The second approximation is to assume that the magnetization modulus $|\mathbf{M}(\mathbf{r})| = M_\mathrm{s}$ is constant throughout the sample, which is a valid approximation if averaging the magnetic moments of a perfect crystal. M_s is, in general, temperature dependent [150] and henceforth we will only deal with isothermal conditions.

Considering all the above, the Gibbs free energy density [10, 151] at a point $\mathbf{r}$ inside a homogeneous ferromagnetic sample is

$$\begin{aligned} g\left[\mathbf{r},\mathbf{m}(\mathbf{r})\right] &= A\left[(\nabla m_{\mathrm{x}})^2+(\nabla m_{\mathrm{y}})^2+(\nabla m_{\mathrm{z}})^2\right] \\ &- \frac{1}{2}\mu_0 M_{\mathrm{s}}\mathbf{H}_{\mathrm{d}}\cdot\mathbf{m}-\mu_0 M_{\mathrm{s}}\mathbf{H}_{\mathrm{a}}\cdot\mathbf{m}+K\left[1-(\mathbf{u}_{\mathrm{k}}\cdot\mathbf{m})^2\right], \end{aligned} \tag{6.1}$$

where $\mathbf{m}(\mathbf{r}) \equiv \mathbf{m}$ is a unitary vector in the direction of the magnetization at point $\mathbf{r}$ and with components m_{x}, m_{y} and m_{z} in the x, y and z directions, respectively.

The first term in Eq. (6.1) is the exchange energy density. This energy tries to keep the ferromagnet with uniform magnetization by penalizing the non uniformity with a positive energy. The exchange constant A is an effective parameter coming from the continuation of the exchange energy [1] and is related to the exchange energy density between neighboring spins. A also takes into account the symmetry of the crystal, which in our case is cubic because we are considering that A is isotropic throughout the material [1, 152]. The second term in Eq. (6.1) corresponds to the magnetostatic energy density [1, 3, 97]. $\mathbf{H}_{\mathrm{d}}(\mathbf{r}) \equiv \mathbf{H}_{\mathrm{d}}$ is the demagnetizing field whose sources are the surface and volumic magnetic poles of the sample itself. At every point this field depends on all the magnetic poles of the sample, in this sense it is a global quantity. The demagnetizing or stray energy is minimized by reducing the poles or, equivalently the demagnetizing field in the sample. The exchange energy, depends on the gradient of the magnetization at each point and therefore is a local quantity. The energy density due to the interaction of the sample with an external applied field $\mathbf{H}_{\mathrm{a}}$ (Zeeman energy) is the third term of Eq. (6.1). This term becomes minimum when the magnetization aligns in the direction of the field. The last term of Eq. (6.1) is the energy density due to uniaxial crystalline anisotropy in the direction of the unitary vector $\mathbf{u}_{\mathrm{k}}$. This means that the anisotropy energy density is minimized when the magnetization points the direction $\mathbf{u}_{\mathrm{k}}$ or $-\mathbf{u}_{\mathrm{k}}$, which are the easy magnetization directions. Other crystalline anisotropy symmetries can be studied within the micromagnetic framework by simply substituting the last term of Eq. (6.1) by the corresponding expression [10]. However we will only deal with uniaxial anisotropy.

6.2 Brown's Static Equations

A static physical magnetization distribution in a ferromagnetic body is one that minimizes the Gibbs free energy [1], that is, the sum of $g\left[\mathbf{r},\mathbf{m}(\mathbf{r})\right]$ over the sample volume. Eq. (6.1) may present many relative minima corresponding to different magnetization patterns. Many works have been published by assuming a magnetization distribution and minimizing the energy as a function of one parameter. For instance in [153] the domain wall thickness is found assuming Bloch, Néel or cross-tie walls magnetization configurations. In Ref. [154] it is assumed a configuration close to a vortex state and the best magnetization shape for the minimum energy is found.

It is possible to find a set of equations that $\mathbf{m}$ must satisfy so that the energy of the magnetic sample is an extremal (maximum or minimum). This set of equations is called Brown's static equations [9, 150] and can be obtained using first order variations [1, 9, 150] on $\mathbf{m}$ of the Gibbs energy density [Eq. (6.1)] or deriving Eq. (6.1) by $\mathbf{m}$ [10]. Brown's static equations are

$$\begin{cases} \mathbf{m} \times \mathbf{H}_{\text{eff}}(\mathbf{r}) = 0, & \text{if } \mathbf{r} \in \mathrm{V}, \quad (6.2) \\ \dfrac{\partial \mathbf{m}}{\partial \mathbf{n}} = 0, & \text{if } \mathbf{r} \in \partial \mathrm{V}, \quad (6.3) \end{cases}$$

where V is the volume of the sample and ∂V its surface. In Eq. (6.2), $\mathbf{H}_{\text{eff}}(\mathbf{r}) = \mathbf{H}_{\text{eff}}$ is the effective field, defined as

$$\mathbf{H}_{\text{eff}} = \frac{2A}{\mu_0 M_{\text{s}}} \nabla^2 \mathbf{m} + \mathbf{H}_{\text{d}} + \mathbf{H}_{\text{a}} + \frac{2K}{\mu_0 M_{\text{s}}} \mathbf{u}_{\text{k}} \left(\mathbf{m} \cdot \mathbf{u}_{\text{k}} \right), \tag{6.4}$$

with

$$\nabla^2 \mathbf{m} = \frac{\partial^2 \mathbf{m}}{\partial x^2} + \frac{\partial^2 \mathbf{m}}{\partial y^2} + \frac{\partial^2 \mathbf{m}}{\partial z^2}. \tag{6.5}$$

Equation (6.2) indicates that the magnetization at each point of the magnetic sample must have the same direction to the effective field $\mathbf{H}_{\text{eff}}$ for the magnetization distribution to be in a local energy minimum (or maximum). This field is also a continuous function of the position and contains the contributions of the exchange (first term), magnetostatic (second term), external applied field (third term) and anisotropy (last term) energies. It must be noticed that adding an arbitrary term proportional to $\mathbf{m}$ to the effective field does not change the solution of (6.2) [1].

The second equation [Eq. (6.3)] refers to the boundary conditions [1, 151, 155, 156] meaning that at the sample surface the magnetization must not vary along the direction $\mathbf{n}$ (perpendicular to the surface). This condition arise from the symmetry breaking of exchange interactions at the surfaces [151]. The case shown here is the free boundary conditions [151]. If the material is attached to other magnetic materials with different exchange anisotropy, Eq. (6.3) may be modified at the interface between the two materials [157, 158].

The Gibbs free energy density Eq. (6.1) can now be rewritten in terms of the contributions to the effective field $\mathbf{H}_{\text{eff}}$ as

$$g\left[\mathbf{r}, \mathbf{m}\right] = -\frac{1}{2} \mu_0 M_{\text{s}} \mathbf{m}(\mathbf{r}) \left[\mathbf{H}_{\text{ex}}(\mathbf{r}) + \mathbf{H}_{\text{d}}(\mathbf{r}) + 2\mathbf{H}_{\text{a}}(\mathbf{r}) + \mathbf{H}_{\text{an}}(\mathbf{r}) \right], \tag{6.6}$$

with $\mathbf{H}_{\text{ex}}(\mathbf{r}) = \mathbf{H}_{\text{ex}}$ the exchange field [first term of Eq. (6.4)] and $\mathbf{H}_{\text{an}}(\mathbf{r}) = \mathbf{H}_{\text{an}}$ the anisotropy field [last term of Eq. (6.4)].

The advantage of Brown's equations is that by assuming a certain magnetization (either minimum or not) the result of the calculation is a magnetization distribution whose energy is a relative minimum. This makes possible to describe hysteresis because one finds a relative energy minimum at a certain applied field taking into account the magnetization distribution at the previous applied field, hence the history of the magnetic sample.

6.3 Discretization of Effective Field

Consider a ferromagnetic sample whose saturation magnetization is M_s having a uniaxial anisotropy with constant K and direction $\mathbf{u}_\mathrm{k}$. The exchange of the sample is considered isotropic with exchange constant A. We divide the magnetic sample into N_x, N_y and N_z parts in the x, y and z directions forming a regular array of $N = N_\mathrm{x}\times N_\mathrm{y}\times N_\mathrm{z}$ orthorhombic cells with sides Δ_x, Δ_y and Δ_z. Each discretization cell (micromagnetic cell) i is characterized by three integer indexes i_x, i_y and i_z in the cartesian coordinates, and is uniformly magnetized in the direction $\mathbf{m}_i$ (where $|\mathbf{m}_i| = 1$ and with components m_{ix}, m_{iy} and m_{iz}). The center of i-th cell will be denoted by the coordinates x_i, y_i and z_i ($\mathbf{r}_i = x_i\mathbf{e}_x + y_i\mathbf{e}_y + z_i\mathbf{e}_z$, being $\mathbf{e}_x$, $\mathbf{e}_y$, and $\mathbf{e}_z$ the unit vectors in the cartesian coordinates).

The size of the micromagnetic cell must be small enough to make sure that the exchange forces in the cell dominate over the long range magnetostatic interactions. If this is the case it is valid to assume uniformly magnetized cells. The size of the cell may be determined by a characteristic length of the material, that for soft ferromagnets (very low anisotropy) is the exchange length defined by $l_\mathrm{ex} = \sqrt{2A/\mu_0 M_\mathrm{s}}$ [10]. This length indicates the order of magnitude over which $\mathbf{m}$ varies in direction by comparing the strength of the exchange and magnetostatic energies [151]. Much more coarser meshes may lead to very different unphysical solutions as discussed in [159] and calculated in [160].

In order to solve Eqs. (6.2) and (6.3) the effective field must be evaluated in the sample volume, or equivalently in all our micromagnetic cells. In the following sections it is described how to calculate numerically the discrete version of the effective field [Eq. (6.4)] at each micromagnetic cell.

6.3.1 Applied Field

When an external magnetic field $\mathbf{H}_\mathrm{a} = \mathbf{H}_\mathrm{a}(\mathbf{r})$ is applied to the sample the field at each cell is defined as

$$\mathbf{H}_{\mathrm{a},i} = \mathbf{H}_\mathrm{a}(\mathbf{r}_i), \tag{6.7}$$

this is, it is considered that in all the cell volume the applied field is uniform and with value and direction corresponding to center of the cell i.

6.3.2 Uniaxial Anisotropy Field

The effective field arising from uniaxial anisotropy at a cell i only depends on its local magnetization direction $\mathbf{m}_i$ and is

$$\mathbf{H}_{\mathrm{an},i} = \frac{2K}{\mu_0 M_\mathrm{s}}\mathbf{u}_\mathrm{k}\left(\mathbf{m}_i \cdot \mathbf{u}_\mathrm{k}\right). \tag{6.8}$$

Its direction is always along the easy axis of the material (defined by $\mathbf{u}_\mathrm{k}$) being its magnitude zero when $\mathbf{m}_i$ is perpendicular to the easy axis.

6.3.3 Exchange Field

The exchange field [first term of Eq. (6.4)], is a local quantity and depends on a second derivative $\nabla^2\mathbf{m}$. Therefore, to calculate the exchange field at the center of a cell i the $\mathbf{m}$ values of its neighboring cells are needed. This field is evaluated using the six nearest neighboring cells to the i-cell (two for each of the cartesian coordinates). The second numerical derivative of a function f at the discretization point i in the x direction is, if i belongs to the bulk

$$\left.\frac{\partial^2 f}{\partial x^2}\right|_i = \frac{f_{i_x-1,i_y,i_z} - 2f_{i_x,i_y,i_z} + f_{i_x+1,i_y,i_z}}{\Delta_x^2}, \tag{6.9}$$

where f_{i_x-1,i_y,i_z} and f_{i_x+1,i_y,i_z} are the values of the f function at the neighboring cell in the negative and positive x directions, respectively. Equivalently the second derivatives in the y and z directions are

$$\begin{aligned}\left.\frac{\partial^2 f}{\partial y^2}\right|_i &= \frac{f_{i_x,i_y-1,i_z} - 2f_{i_x,i_y,i_z} + f_{i_x,i_y+1,i_z}}{\Delta_y^2}, &(6.10)\\ \left.\frac{\partial^2 f}{\partial z^2}\right|_i &= \frac{f_{i_x,i_y,i_z-1} - 2f_{i_x,i_y,i_z} + f_{i_x,i_y,i_z+1}}{\Delta_z^2}, &(6.11)\end{aligned}$$

respectively. According to Eq. (6.4) and Eq. (6.5) the discrete version of the exchange field at a cell i is

$$\begin{aligned}\mathbf{H}_{ex,i} &= \frac{2A}{\mu_0 M_\mathrm{s}}\left(\left.\frac{\partial^2 m_x}{\partial x^2}\right|_i + \left.\frac{\partial^2 m_x}{\partial y^2}\right|_i + \left.\frac{\partial^2 m_x}{\partial z^2}\right|_i\right)\mathbf{e}_x\\ &+ \frac{2A}{\mu_0 M_\mathrm{s}}\left(\left.\frac{\partial^2 m_y}{\partial x^2}\right|_i + \left.\frac{\partial^2 m_y}{\partial y^2}\right|_i + \left.\frac{\partial^2 m_y}{\partial z^2}\right|_i\right)\mathbf{e}_y\\ &+ \frac{2A}{\mu_0 M_\mathrm{s}}\left(\left.\frac{\partial^2 m_z}{\partial x^2}\right|_i + \left.\frac{\partial^2 m_z}{\partial y^2}\right|_i + \left.\frac{\partial^2 m_z}{\partial z^2}\right|_i\right)\mathbf{e}_z. \end{aligned} \tag{6.12}$$

The above equation is only valid if the cell i is at the bulk. At the boundaries of the magnetic sample the exchange field must be evaluated differently in order to accomplish Eq. (6.3). This equation expresses that across the boundary of the sample the magnetization direction must not change. To take this into account some authors [161, 162] introduce a virtual shell of micromagnetic cells surrounding the boundary of the sample whose magnetization direction $\mathbf{m}$ is the same as its first neighbor. This shell is sometimes called mirror shell. The boundary cells at which we want to calculate the field undergo an exchange field due to its mirror whose direction is proportional to their magnetization and therefore, as explained before, can be left out. For this reason, in our calculations we only consider the exchange field produced by the real neighbors (in these cases, the "out-of-sample" terms in Eqs. (6.9), (6.10), (6.11) are considered zero). This method of calculating the exchange field at the boundaries is only valid when using six neighbors [161].

6.3.4 Magnetostatic or Stray Field

The demagnetizing field at the center of a micromagnetic cell is the sum of the stray field over this cell due to all the cells, including itself. When calculating the field at a cell, the first attempt is to consider that the field of each is of dipolar origin. This is, a dipole of moment $M_\mathrm{s}\Delta_x\Delta_y\Delta_z$ set at the center of each cell. The dipolar field is the same as for a uniformly magnetized sphere (outside the sphere) and therefore the approximation of a dipole in an orthorhombic micromagnetic box is better when the box is cubic. In this scheme, the field at the center of a cell due to itself (self field) is infinite. However, in the cubic approximation there is no need to evaluate the self field because uniformly magnetized cubes have no shape anisotropy [163, 164, 165] (their self energy is independent of the magnetization direction) and their field at its center is proportional to its magnetization. Therefore this field can be left out in the calculation of the effective field as mentioned above.

A much better approximation, specially for non-cubic cells, is calculating the field at the center of each cell due to uniformly magnetized cells. It should be borne in mind that since each cell is uniformly magnetized its volumic pole density is zero throughout the cell. However, a surface magnetic pole density does exist. Parallel surfaces of the cell have the same uniform surface magnetic pole density but of opposite sign. Their magnetic pole density depends on the direction of the magnetization on the cell and ranges from $-M_\mathrm{s}$ to M_s continuously depending on the local $\mathbf{m}$. This approximation allows to evaluate the self field of a cell. This scheme is more realistic than the dipolar one. In [163] a comparative study between both is made.

There are some cases in wich the evaluation of the demagnetizing field at the center of the cell can lead to large errors if the micromagnetic cell is not cubic. For instance there is a systematic error in the demagnetizing energy computation in thin magnetic samples magnetized along the thin direction [166]. In this case, the demagnetizing field evaluated at the center of the cell is the largest and therefore an overestimation of the demagnetizing energy is committed. A simple way to overcome this problem is to average the field over the entire cell [167, 168] instead of calculating it at its center. Throughout this work this last approximation will be followed.

The averaged demagnetizing field at a cell i due to a cell j may be expressed in the form of a matrix as

$$\mathbf{H}_{d,ij} = M_\mathrm{s} \begin{pmatrix} \eta_{ij}^{xx} & \eta_{ij}^{xy} & \eta_{ij}^{xz} \\ \eta_{ij}^{yx} & \eta_{ij}^{yy} & \eta_{ij}^{yz} \\ \eta_{ij}^{zx} & \eta_{ij}^{zy} & \eta_{ij}^{zz} \end{pmatrix} \begin{pmatrix} m_{jx} \\ m_{jy} \\ m_{jz} \end{pmatrix} = M_\mathrm{s}\eta_{ij}\mathbf{m}_j. \tag{6.13}$$

The matrix η_{ij} is purely geometrical and its elements have no units. A component η_{ij}^{xy} may be understood as the volume average of the x component of the demagnetizing field (normalized to M_s) due to a cell j uniformly magnetized in the y direction. The readers are referred to Appendix B for detailed calculation and discussion of the symmetries of the matrix η_{ij}.

The total demagnetizing field over a cell i is the sum of the field due to all the cells, therefore

$$\mathbf{H}_{\mathrm{d},i} = M_{\mathrm{s}} \sum_{j=1}^{N} \eta_{ij} \mathbf{m}_j. \tag{6.14}$$

Here, N calculations are needed to obtain the demagnetizing field at each cell, therefore for all the cells N^2. This makes this field the most time consuming in micromagnetic calculations. To overcome this problem some authors take advantage of the equidistant meshes and apply fast Fourier transforms [169, 170, 171] which reduces the number of calculations. Another approach is used here, and consists in defining a second discretization grid for the sample to approximate the demagnetizing field of far cells.

Consider now a coarser discretization of our micromagnetic sample $N_{xc} \times N_{yc} \times N_{zc} = N_c$. This discretization is related to the fine one (micromagnetic cells) by $N_x = n_x N_{xc}$, $N_y = n_y N_{yc}$ and $N_z = n_z N_{zc}$ where n_x, n_y and n_z are integers larger than 1 so that each coarse cell contains $n = n_x n_y n_z$ small cells in its interior. An schematic representation of the two grids in the case of $n_x = n_y = 3$ is shown in Fig. 6.1(a). In this scheme each micromagnetic cell i belongs to a larger cell i_c whose magnetization unit vector is defined as $\mathbf{m}_{ic}$, calculated as the average of $\mathbf{m}$ of the small containing cells.

The demagnetizing field at a general micromagnetic cell i has two contributions in this approximation, one from the small neighboring cells and another from the far coarse cells. This is mathematically expressed as

$$\mathbf{H}_{\mathrm{d},i} = \sum_{j \in t_i} \eta_{i,j} \mathbf{m}_j + \sum_{j \in T_i} \eta_{ij,c} \mathbf{m}_{j,c}, \tag{6.15}$$

where η_{ij} and $\eta_{ij,c}$ are the matrices for fine and coarse meshes, respectively.

In Eq. (6.15) t_i represents the set of small cells whose large cell is in contact with the large cell containing i. In Fig. 6.1(b) these neighboring cells are colored in light gray. T_i is the set of all the coarse cells whose small cells are not elements of t_i. A subset of T_i is represented in dark gray in Fig 6.1(b), all the remaining elements of T_i are not represented in this figure.

The first sum of Eq. (6.15) is over $27n$ and the second over $N/n - 9$. Therefore, for the total demagnetizing field evaluation the number of calculations is of the order of N^2/n^2 for N sufficiently large, reducing the computational time considerably.

Our approximation is very accurate in calculating the major contribution to the demagnetizing field of a cell, which is the field of its neighboring cells. The field from farther cells decays very rapidly with distance and tends to be the field of a dipole. This last contribution is very weak and for this reason large cells are considered avoiding the details of the fine grid. The approximation of considering large cells uniformly magnetized in the direction of the averaged containing cells is only justified where both discretization cells are of the order of magnitude of the exchange length of the material considered. In this way one can assume a quasiuniform magnetization at each large cell.

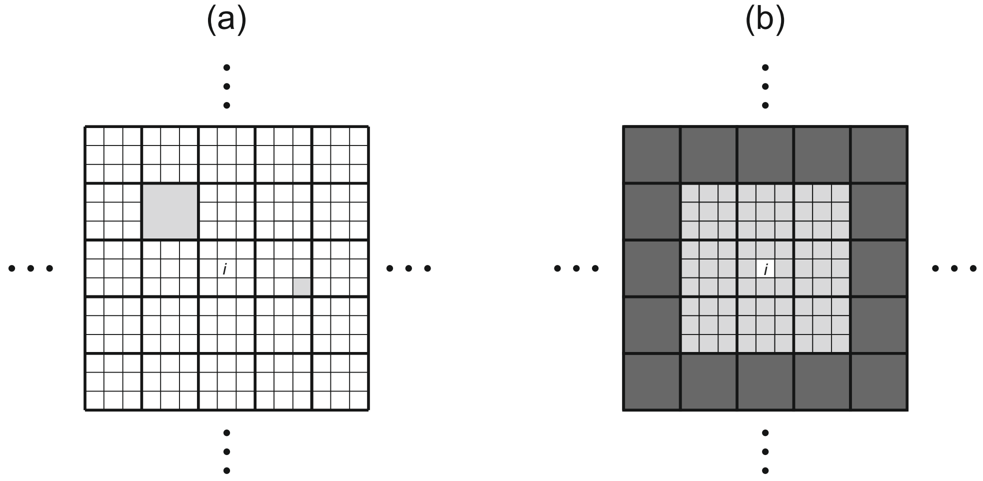

Figure 6.1: Schematic representation of the neighboring cells of a fine cell i in a two dimensional discretization. Coarse and fine grids (separated by thick and thin lines, respectively) are related with the parameters $n_x = n_y = 3$. A cell of each discretization is colored in light gray in (a). Dots indicate that there are more cells out of this neighborhood. In (b) fine cells light gray colored represent the set t_i whereas coarse cells in dark gray represent a subset of T_i. The remaining elements to complete T_i are all the coarse cells outside the represented neighborhood.

6.4 Numerical Iterative Procedure

Consider the set of all micromagnetic cells in a discretized sample whose magnetization directions are initially $\mathbf{m}_1(\zeta = 0), \cdots, \mathbf{m}_N(\zeta = 0)$, where ζ is the iteration step. The effective field is calculated at each cell as discussed above having the set $\mathbf{H}_{\text{eff},1}(\zeta), \cdots, \mathbf{H}_{\text{eff},N}(\zeta)$. Since at equilibrium the local magnetization points the effective field [Eq. (6.2)] we force each cell i to be in the same direction as its effective field, namely

$$\mathbf{m}_i(\zeta + 1) = \frac{\mathbf{H}_{\text{eff},i}(\zeta)}{|\mathbf{H}_{\text{eff},i}(\zeta)|}. \tag{6.16}$$

This process is repeated until the maximum change of angle (azimuth ϕ and zenith θ in spherical coordinates) with respect to the previous iteration step is below a threshold ϵ. This last condition must be fulfilled at all the cells. Therefore, for reaching the solution, the conditions

$$|\phi_{\mathbf{m}_i(\zeta+1)} - \phi_{\mathbf{m}_i(\zeta)}| < \epsilon, \tag{6.17}$$

$$|\theta_{\mathbf{m}_i(\zeta+1)} - \theta_{\mathbf{m}_i(\zeta)}| < \epsilon, \tag{6.18}$$

must be satisfied for every $i = 1, \cdots, N$. Here, $\phi_{\mathbf{m}_i(\zeta)}$ and $\theta_{\mathbf{m}_i(\zeta)}$ are the angles of the magnetization direction of a general micromagnetic cell i.

Once the equilibrium magnetization is found, we can calculate each energy contribution with the corresponding effective field as in Eq. (6.6). This is,

$$\begin{aligned} G = & - \mu_0 M_\mathrm{s} V_\mathrm{c} \sum_{i=1}^{N} \mathbf{H}_{\mathrm{a},i} \mathbf{m}_i - \frac{1}{2} \mu_0 M_\mathrm{s} V_\mathrm{c} \sum_{i=1}^{N} \mathbf{H}_{\mathrm{d},i} \mathbf{m}_i \\ & - \frac{1}{2} \mu_0 M_\mathrm{s} V_\mathrm{c} \sum_{i=1}^{N} \mathbf{H}_{\mathrm{ex},i} \mathbf{m}_i - \frac{1}{2} \mu_0 M_\mathrm{s} V_\mathrm{c} \sum_{i=0}^{N} \mathbf{H}_{\mathrm{an},i} \mathbf{m}_i, \end{aligned} \tag{6.19}$$

where $V_\mathrm{c} = \Delta_x \Delta_y \Delta_z$ is the volume of the micromagnetic cell. A quasi-static hysteresis loop is performed by first saturating the sample at a large magnetic field and then decreasing the field in small steps until the sample gets saturated in the opposite direction. At each field the equilibrium magnetization distribution is found by the iteration method described. Following this, highly metastable states could appear. For instance in small enough particles, typically the initial positive uniform state persist up to large negative field values which in turn results in large coercivities. In order to randomly break the symmetry of these states and allow the magnetic sample to reach more stable and less energetic magnetization distribution, we add a random parameter to our algorithm. When the field is changed and before the first iteration step, each $\mathbf{m}_i$ is changed by the angles $\pm\phi_{i,\epsilon}$ and $\pm\theta_{i,\epsilon}$. These angles are different at each micromagnetic cell and are generated from a random uniform distribution [172] with maximum amplitude ϵ.

6.5 Limits and Validity of the Model

The model presented in this chapter is only valid for ferromagnetic or ferrimagnetic materials at a fixed temperature T that determines the averaged magnetic moment $M_\mathrm{s}(T) = M_\mathrm{s}$. Here, only the quasi-static regime is considered (no time dependence) although it is possible to introduce some modifications in the exchange field [Eq. (6.4)] to take into account time effects. This can be done using the Landau-Lifshitz-Gilbert equation [1, 10].

The approximation of continuum matter makes only sense when calculating macroscale physical quantities such as domain wall size. Any result coming out from our calculations with size smaller than the exchange length may be unphysical and further analysis should be carried out. This means, for instance, that within our approximation we can not describe quantum spins but only their average behavior.

The numerical procedure presented in this chapter is tested in Appendix C where a standard problem is solved and compared to different solutions obtained by other authors. There we present reasonings why we use 6 neighbor to calculate the exchange field instead of 12 neighbors, which is more accurate. We also use $\epsilon = 10^{-4}$ in all the thesis as justified in Appendix C. This numerical procedure is valid for any size of the magnetic particle. However, since the size of the micromagnetic cell is fixed at the exchange length, the larger the magnetic particle the more micromagnetic cells we use and, thus, the more time consuming the calculation is.

CHAPTER 7

Geometrical Control of Magnetic Vortex States

In thin soft ferromagnetic cylinders (dots) with diameters less than a micron, the most stable magnetization pattern at zero applied field is typically a vortex state [173, 174]. This structure appears close to remanence and consists of an in-plane curling magnetization whose chirality can be clockwise (CW) or counterclockwise (CCW) and an out-of-plane core [175] with polarity up or down. The existence of this four energetic degenerate states of chirality and polarity have potential applications in MRAM [176, 177, 178], but this application requires the independent control of each bit (chirality and polarity).

In the literature there is large number of works focused on the control and/or modification of the vortex state in soft ferromagnetic dots. On the one hand there is much interest in achieving a fast vortex core polarity switching. This reversal process is produced due to applied magnetic field bursts [179] or spin polarized currents [180] that induce an oscillatory mode in the vortex core around its equilibrium position (gyroscopic mode [181]). On the other hand some works show how to control vortex chirality by introducing some asymmetries in the dot shape [182, 183, 184, 185], in its magnetic properties [186], or in the applied field distribution [187, 188, 189]. Some of them also control the polarity of the vortex by adding an out-of-plane magnetic field [184] or by using non-practical complex geometry [185]. The vortex chirality control has been achieved [190, 191] by modulating the thickness of the dot, however, the complete control of chirality and polarity in dots with practical geometries by adjusting a simple parameter is a remaining goal.

In the first section, the hysteresis loop of a typical cylindrical dot is studied to understand the shape modifications introduced in the thickness-modulated dot of the second section. In the last section a simple model to understand the physics will be presented.

7.1 Submicrometer Dot Hysteresis Loop

Consider a cylindrical Permalloy dot with diameter 360 nm and thickness 18 nm discretized in cubes of side 6 nm (l_{ex} =5.7 nm). This material has an exchange constant $A = 1.3 \times 10^{-11}$ J/m, a saturation magnetization $M_{\mathrm{s}} = 8 \times 10^5$A/m and a very low crystalline anisotropy which will be neglected ($K = 0$). The thickness has a similar length compared to l_{ex} so that the magnetization will be quasi-uniform across it. The large diameter-to-thickness ratio of the dot also favors an in-plane ($x - y$ plane) magnetization distribution because otherwise the magnetostatic energy would be very large according to the demagnetizing factors [4, 192].

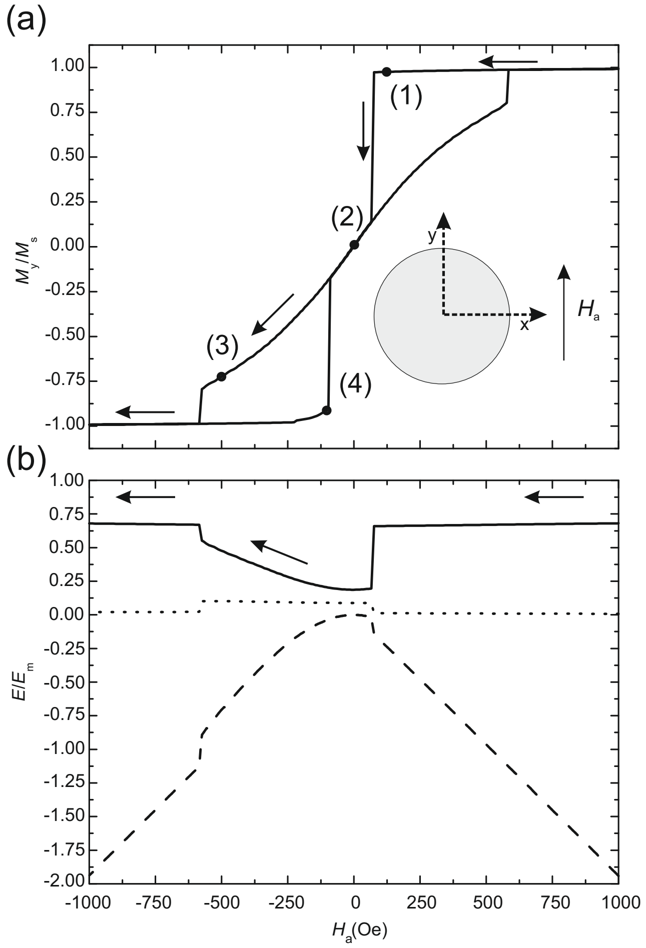

Figure 7.1: (a) Magnetization in the applied field direction of a Permalloy dot with diameter 360 nm and thickness 18 nm as a function of the applied field value. A schematic representation of the dot and the direction of the applied field is shown in the inset. Points with numbers indicate the magnetization along the applied field for the field values $\mathbf{H}_{\mathrm{a}} = 125, 0, -500$ Oe corresponding to numbers 1,2 and 3, respectively in the initial curve (marked with arrows). Number 4 is at -98 Oe of the reverse curve. (b) Energies of the initial curve normalized to the magnetostatic energy (E_{m}) of a perfectly in-plane uniformly magnetized dot with the geometry considered. Here straight, dotted and dashed lines are the magnetostatic, exchange and applied field energies, respectively.

A typical hysteresis loop of this dot with a uniform in-plane applied field is shown in Fig. 7.1(a). In the inset of this figure we show a schematic representation of the dot and the direction of the applied field (y direction). The corresponding energies (exchange, applied field and magnetostatic) normalized to the magnetostatic energy of the uniformly magnetized dot ($E_{\mathrm{m}} = \mu_0 M_{\mathrm{s}}^2 NV/2$, where V the volume of the dot and N its in-plane demagnetizing factor for $\chi \to 0^+$ [4]) are shown in Fig. 7.1(b).

At the beginning of the initial curve (from positive to negative applied field), the dot is saturated with a very large field. The Zeeman term is dominant over the exchange and magnetostatic ones and the particle gets magnetized in the direction of the applied field. The exchange energy is close to its minimum (zero) due to the uniformity of the magnetization. Magnetostatic energy however is very close to its maximum but does not reach it because, as can be seen in Fig. 7.2(1), the **m** distribution curves in the regions near the surfaces. This magnetization curvature reduces the surface magnetic pole density lowering the magnetostatic energy with respect to the uniform case. Commonly this magnetization shape is called onion state.

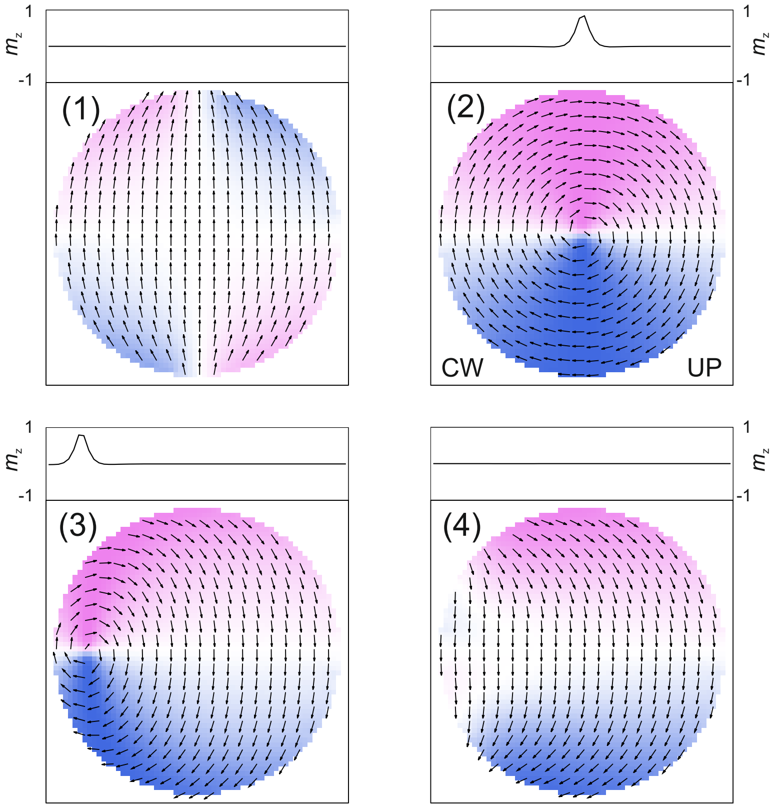

Figure 7.2: In-plane magnetization distribution at different applied fields marked with points 1,2,3 and 4 in Fig. 7.1(a). Arrows indicate the magnetization direction and violet and blue colors mark the regions where $m_x > 0$ and $m_x < 0$, respectively. Out-of-plane magnetization at $y = 0$ is shown at the top of each in-plane magnetization distribution plotted. The number of plotted spins is reduced for clarity.

When the applied field is decreased and close to zero, the Zeeman energy becomes negligible and the competition between exchange and magnetostatic energies determines the magnetization distribution. In this region is where the vortex state appears minimizing the magnetostatic energy at the expense of the exchange energy. As seen in Fig. 7.2(2), the magnetization curls in-plane so that surface and volumic poles are reduced, which turns in a sharp decrease of the magnetostatic energy as in Fig. 7.1 (b). The exchange energy, however, increases because the magnetization distribution is no longer uniform. At the core of the vortex, this in-plane curl would lead to an infinite exchange energy of the dot because there would be a very rapid magnetization change in this region. Therefore, at the core, the exchange forces the magnetization to uniformly point out-of-plane. This, in turn, produces a surface magnetic pole density in the core surfaces that prevents the magnetization energy to decrease to zero. In the vortex shown here Fig. 7.2(2), the chirality is clockwise (CW) and the vortex core points in the positive z direction (up).

Further decrease of the applied field maintains the vortex distribution [193, 194] due to its large stability but shifts its core as shown in Fig. 7.2(3). The shift is always perpendicular to the applied field and with direction determined by the chirality. In our case, since the vortex is CW the region pointing the negative field tends to increase so the vortex shifts to $-x$. Conversely, if the vortex was CCW the movement would be in $+x$ direction. So, the vortex chirality determines its movement direction. In all this process the magnetostatic energy increases because the dot is tending to a uniformly magnetized state whereas the exchange is reduced. For a sufficiently large applied field the core is expelled from the dot resulting in uniformly magnetized distribution in the applied field direction (this time, negative).

The reverse curve (from negative to positive applied field) must be ideally the same as the initial one because there is no asymmetry in the dot. However in Fig. 7.2(4) we see that the nucleation field (the field at which the vortex state appears) is smaller in the reverse curve. This is because the symmetry of the uniform state is broken differently in the two curves owing to the random. In our case for instance, a C-state [shown in Fig. 7.2(4)] appears just before the nucleation of the vortex. This precursor state of the vortex determines its chirality, which in this case will be CW. In fact, since this symmetry breaking is random, so it is the chirality and polarity of the vortex generated. This last result indicates that there is no way of controlling chirality and polarity of a vortex state with an in-plane applied field.

7.2 Thickness-Modulated Ferromagnetic Dot

As we say above, by changing the geometry of the dot it is possible to control the vortex state generated. Consider now a dot with diameter $a = 360$ nm and thickness $b = 18$ nm as in the previous section but with a thicker half part of total thickness $b + c = 24$ nm in the region $x > 0$ (see Fig. 7.3 for clarification) separated by a middle edge. An in-plane uniform field is applied at an angle θ_a with respect to the x axis so that $\mathbf{H}_\mathrm{a} = H_\mathrm{a}\left[\cos\theta_\mathrm{a}\mathbf{e}_x + \sin\theta_\mathrm{a}\mathbf{e}_y\right]$ where $\mathbf{e}_x$ and $\mathbf{e}_y$ are the unitary vectors in the x and y directions, respectively.

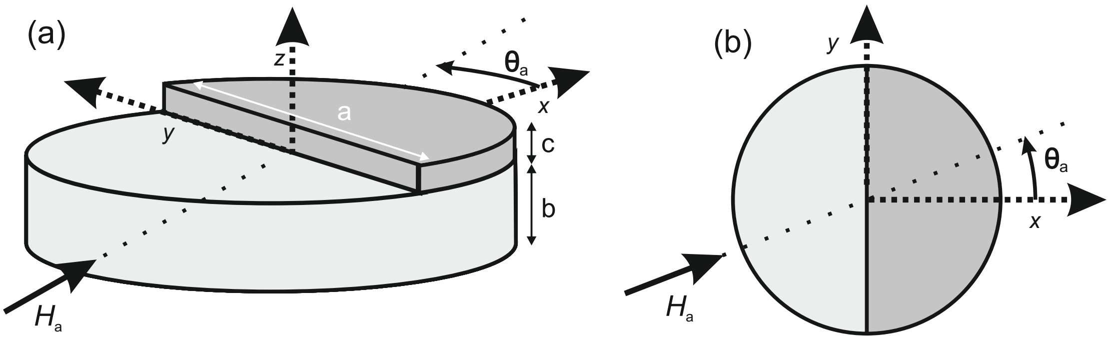

Figure 7.3: Schematic and not scaled representation of the thickness-modulated dot in a 3D (a) and 2D (b) views. This dot has a diameter a and a thickness b. The thicker part, colored in dark gray is set in the half part region $x > 0$ and has a total thickness of $b + c$. The in-plane field is applied at an angle θ_a with respect to the x axis. Positive angles are measured counterclockwise.

In Fig. 7.4(a) we show a calculated hysteresis loop for the dot with an applied field of $\theta_\mathrm{a} = \pi/4$. Initially, the dot is positively saturated in the applied field direction, then the field is decreased up to a non-uniform state appears. As explained before, when the applied field is reduced the minimization of the magnetostatic and exchange energies determines the magnetization pattern. In this case, the thicker zone is the first to bend its magnetization with respect to the applied field direction. A simple explanation for this is that in the thinner region the exchange energy dominates over the magnetostatic one, keeping the magnetization aligned at smaller fields compared to the thicker region. In fact, for sufficiently thin cylindrical dots [173, 174] a non-uniform magnetization is no longer possible and the dot remains uniformly magnetized.

The thicker region curls its magnetization following the applied field and the rounded border of the sample forming a C-state as shown in Fig. 7.4(b)(i) for the initial curve and Fig. 7.4(b)(iii) for the reversal curve. This C-state is determined and therefore so it is the chirality of the next vortex state. In this case at remanence a CCW vortex [see Fig. 7.4(b)(ii)] is formed in the initial curve and a CW vortex [see Fig. 7.4(b)(iv)] in the reversal one.

The vortex core enters by the surface of the dot near a point perpendicular to the applied and in the thinner region [white colored zone at the surface for $\theta = 3\pi/4$ of Figs. 7.4(b)(i) and 7.4(b)(iii)]. Its polarity is also determined and depends on the surface poles generated in the middle edge. When the C-state is formed, the magnetization tending to enter the thicker zone creates negative poles in the flat surface whereas the magnetization tending to exit the thicker zone a positive magnetic pole density. All these poles create an out-of-plane stray field in the whole sample, and in particular in the region where the vortex core nucleates. In our case we can see in Fig. 7.4(b)(i) that the positive poles are closer than the negative ones making a negative out-of-plane field which bias the core to point down [Fig. 7.4(b)(ii)]. Conversely, in the reverse curve the closer poles

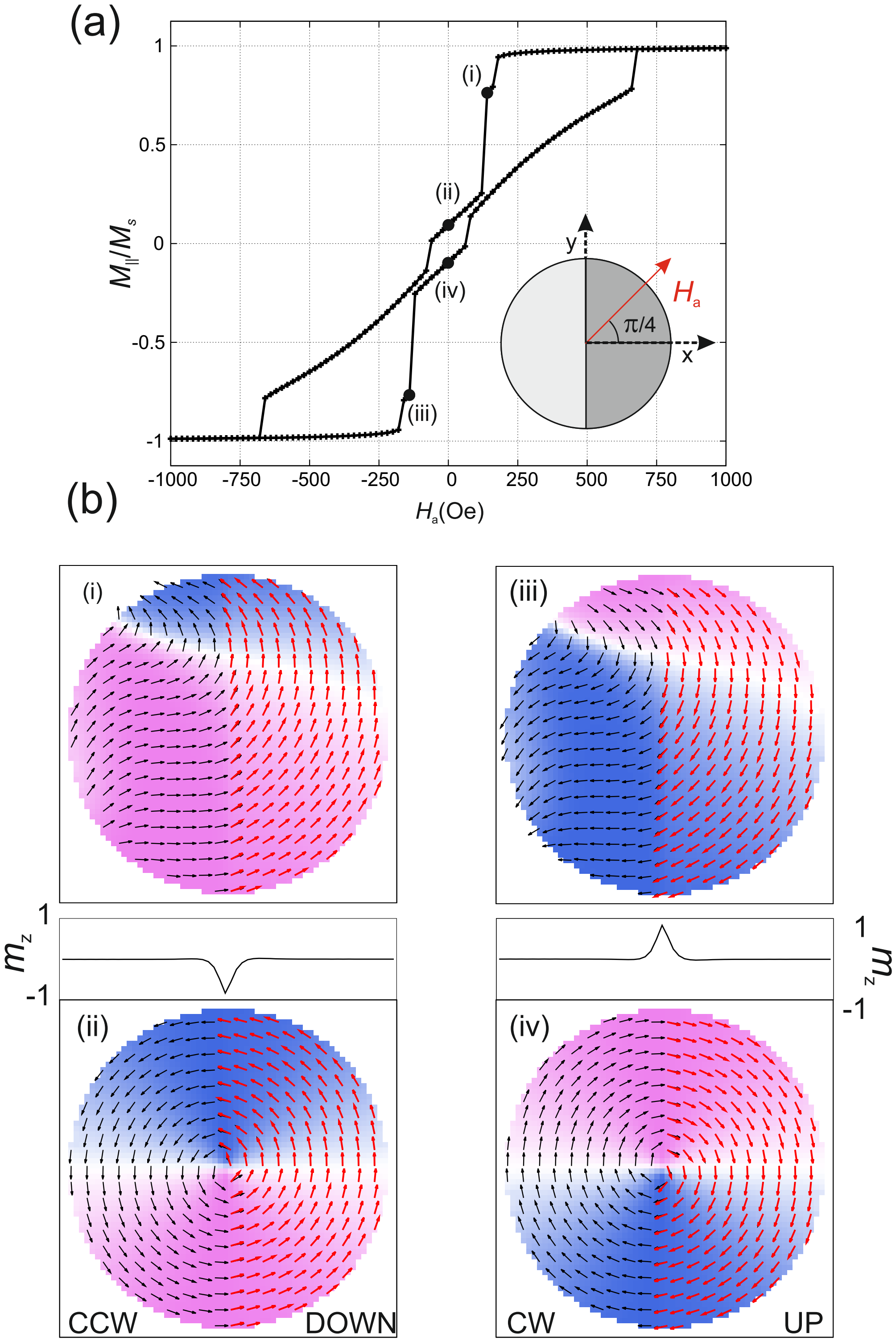

Figure 7.4: (a) Magnetization along the applied field direction $M_{\parallel}$ of a Permalloy dot of Fig. 7.3 with diameter of 360 nm and thicknesses 18 nm and 24 nm. The inset shows a scheme of the dot, where the thicker part ($x > 0$) is colored in dark gray, and the direction of the uniform applied field ($\pi/4$ with respect to the positive x axis) is indicated by a red arrow. (b) Magnetization distribution of the marked points of (a). Black arrows present the in-plane magnetization direction of the bulk and violet and blue colors indicate $m_x > 0$ and $m_x < 0$, respectively. Red arrows indicate the in-plane magnetization of the thicker part. In the upper part of the lower graphs there is also plotted the out-of-plane magnetization m_z along the line $y = 0$ and $z = -3$ nm. The number of plotted spins is reduced for clarity.

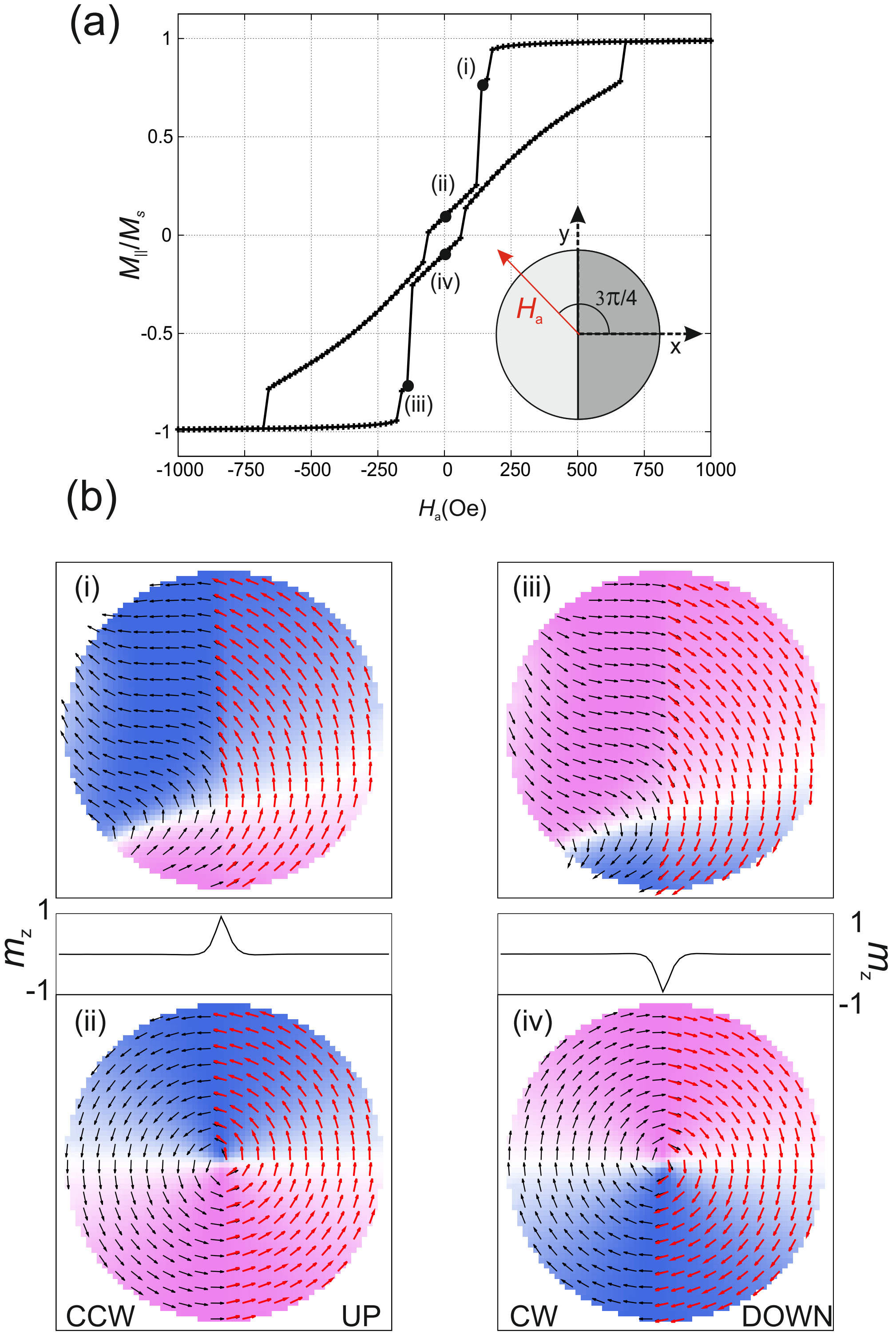

Figure 7.5: Same as Fig. 7.4 but with an applied field angle $\theta_a = 3\pi/4$.

are the negative ones [see Fig. 7.4(b)(iii)] which turns out into a vortex core pointing up as shown in Fig. 7.4(b)(iv). At remanence, the vortex state has a non zero in-plane magnetization because of the non-compensated contribution of the thicker zone [dark gray zone in Fig. 7.3(a)].

Summing up, if the applied field is $\theta_\mathrm{a} = \pi/4$ the remanent state is a CCW-down vortex, whereas the remanent state of the reversal curve is a CW-up vortex. We can define CW and up as $+1$ value, and CCW and down as -1 and the product of chirality and polarity, known as the handedness (H). From the above results we see that the handedness of the vortex in the initial and reverse curves is conserved and in this case is positive.

A hysteresis loop for a different applied field angle ($\theta_\mathrm{a} = 3\pi/4$) is shown in Fig. 7.5(a). In this case, the chirality of the vortex in the initial and reverse curves is the same as in the case $\theta_\mathrm{a} = \pi/4$, because in essence the C-state in the thicker zone follows the direction of the applied field. However the vortex starts to nucleate at $\theta = 5\pi/4$ and therefore the closer surface magnetic poles are opposed to that of the previous case. This is, in the initial curve the negative magnetic poles are closer [see Fig. 7.5(b)(i)] making a positive out-of-plane field that turns into an up core as shown in Fig. 7.5(b)(ii). In the reverse curve the closer poles are the positive ones [see Fig. 7.5(b)(iii)] obtaining a down vortex core as seen in Fig. 7.5(b)(iv). The handedness of the vortex is the same in the initial and reversal curves with a negative value as opposed to the case $\theta_\mathrm{a} = \pi/4$.

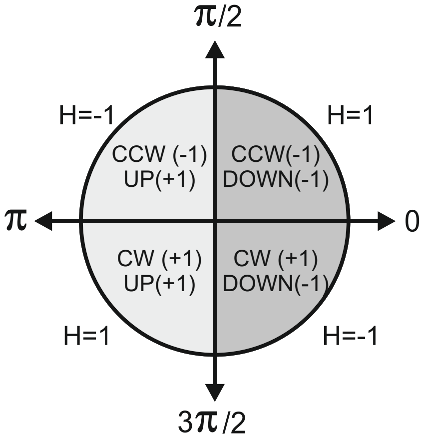

Figure 7.6: Four vortex states obtained from saturating the sample at any angle within the four different quadrants and quasi-statically decrease the field up to zero. H indicates the handedness of the resulting vortex.

With these two examples we have been able to obtain the four different vortex states for a ferromagnetic dot. These results are not only valid for the cases $\theta_\mathrm{a} = \pi/4$ and $\theta_\mathrm{a} = 3\pi/4$, in fact, the same vortex state is obtained if the field is applied at any angle belonging to the same quadrant. This is illustrated in Fig. 7.6 where the remanent vortex state is represented as a function of the angle θ_a. The procedure to prepare a specific state is always saturating the sample in the applied field direction whose remanent state is the desired one and then decrease quasi-statically the field up to zero. There are, however four cases in which the vortex state can not be determined a priori and its final state is random. At $\theta_{\mathrm{a}} = 0, \pi$ chirality is undetermined because the field is symmetric with respect to the thicker part, as a consequence polarity is also undetermined. At $\theta_{\mathrm{a}} = \pi/2, 3\pi/2$ chirality is fully determined but surface magnetic poles generated at the middle edge are symmetric making the vortex core polarity to be undetermined.

The results presented above are not only valid when the edge is in the central line of the dot ($x = 0$). In fact, it can be located at any position x leading to the same results as presented schematically in Fig. 7.6. For instance, we have tested cases where it is located at $x = -a/4$ and $x = a/4$ and obtained the same trends as in Fig. 7.6.

The simplicity of the chirality and polarity control in this kind of dots with modulated thickness is such that can be summarized in two simple rules:

1. Chirality of the vortex state is controlled by both the position of the thicker part and the sign of the applied field component parallel ($H_{a||}$) to the middle edge. If the position of the thicker zone is at right (left), for $H_{a||} > 0$ the chirality is CCW (CW) whereas for $H_{a||} < 0$ is CW (CCW).

2. Vortex core polarity is controlled by the sign of the magnetic poles (induced by the chirality in the flat surface of the edge) closer to the vortex core nucleation point. If the sign is positive (negative) the vortex core is down (up).

7.3 Analytical Model

A simple analytical model can capture the physics of the vortex-state determination in these dots. We consider the dot shown in Fig. 7.3 with the same dimensions as in the numerical case and with the in-plane applied field in the θ_{a} direction. As first approximation we consider that the vortex nucleates perpendicular to the applied field direction and in the thinner part. The nucleation point is, therefore,

$$\begin{aligned} x &= x_{\mathrm{n}} = -\frac{a}{2}|\sin\theta|, \\ y &= y_{\mathrm{n}} = \frac{a}{2}\mathrm{Sign}[\sin\theta]\cos\theta, \\ z &= z_{\mathrm{n}} \in [0, -b], \end{aligned}$$

(cross in Fig. 7.7), this is, at an angle $\theta_{\mathrm{a}} + \pi/2$ if $\theta_{\mathrm{a}} \in [0, \pi]$ and at an angle $\theta_{\mathrm{a}} - \pi/2$ if $\theta_{\mathrm{a}} \in [\pi, 2\pi]$. Magnetic pole densities induced in the C-state are assumed as two opposite magnetic charges Q_{m1} and Q_{m2} (Fig. 7.7). The sign of the magnetic charges is obtained by the sign of the applied-field component parallel to the flat surface of the middle edge $Q_{\mathrm{m1}} = M_{\mathrm{s}} c \frac{a}{2}\mathrm{Sign}[\sin\theta]$ and $Q_{\mathrm{m2}} = -Q_{\mathrm{m1}}$, so the chirality is $C = \mathrm{Sign}[\sin\theta]$. The sign of the out-of-plane component of the magnetic field created by these point charges at the nucleation point determines the polarity of the vortex $P = \mathrm{Sign}[H_z(x_{\mathrm{n}}(\theta), y_{\mathrm{n}}(\theta), z_{\mathrm{n}}(\theta))]$.

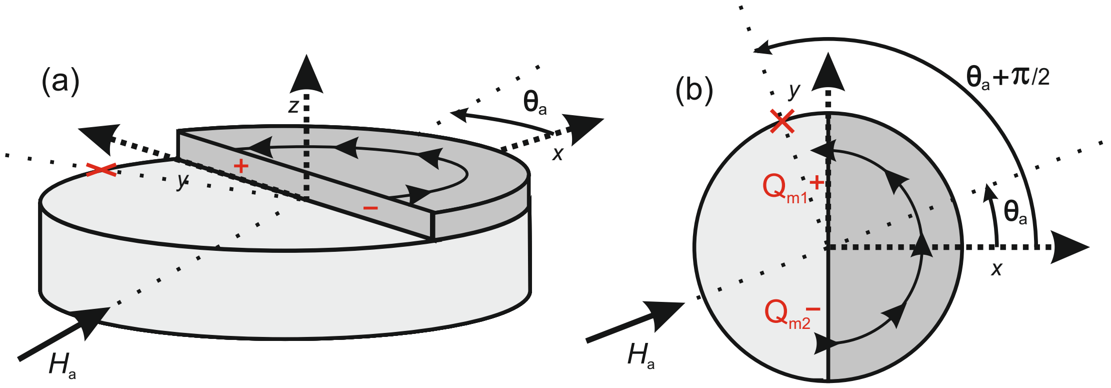

Figure 7.7: Schematic representation for the analytical model. (a) and (b) are 3D and 2D views, respectively. The red cross marks the nucleation point ($\theta_\mathrm{a} + \pi/2$) of the vortex. The C-state direction is indicated by the arrows in the thick part. As an approximation two point charges (instead of a continuum) with absolute value Q_m1 are set in the middle edge of the dot at the points with the same x and z coordinates ($x = 0$, $z = b + c/2$) but $y = a/4, -a/4$.

The out-of-plane field at any point in the space x, y, z can be written as the sum of the contributions of the two charges as

$$H_\mathrm{z}(x,y,z) = H_\mathrm{z1}(x,y,z) + H_\mathrm{z2}(x,y,z), \tag{7.1}$$

$$H_\mathrm{z1}(x,y,z) = \frac{Q_\mathrm{m1}}{4\pi}\frac{(z-c/2)}{(x^2+(y-a/4)^2+(z-c/2)^2)^{\frac{3}{2}}}, \tag{7.2}$$

$$H_\mathrm{z2}(x,y,z) = \frac{Q_\mathrm{m2}}{4\pi}\frac{(z-c/2)}{(x^2+(y+a/4)^2+(z-c/2)^2)^{\frac{3}{2}}}. \tag{7.3}$$

We are interested in the sign of the field at the nucleation point, depending on which the vortex core will be up or down.

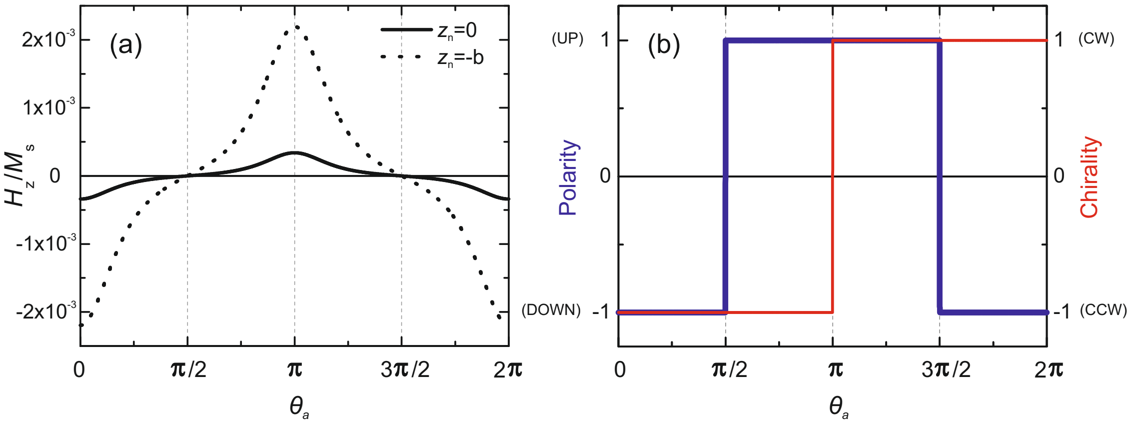

Figure 7.8: (a) Out-of-plane magnetic field created by the two opposite magnetic charges at the nucleation point with $z_\mathrm{n} = 0$ (solid) and $z_\mathrm{n} = -b$ (dotted) as a function of the angle θ_a between the applied field and the $x > 0$ axis. (b) Polarity (thick blue) and chirality (thin red) of the vortex state as a function of θ_a.

Figure 7.8(a) shows the evolution of the out-of-plane charge field with θ_a for $z_\mathrm{n} = 0$ (solid) and $z_\mathrm{n} = -b$ (dotted). In both cases and in the intermediate ones the trend is the same. For $0 < \theta_\mathrm{a} < \pi/2$ and $3\pi/2 < \theta_\mathrm{a} < 2\pi$ the z-field is negative because the positive charge (Q_m1 and Q_m2, respectively) is the nearest. When $\pi/2 < \theta_\mathrm{a} < \pi$ and $\pi < \theta_\mathrm{a} < 3\pi/2$ the proximity of the negative charge (Q_m2 and Q_m1, respectively) makes the field to be positive. At $\theta = \pi/2$ and $\theta = 3\pi/2$ the z-field is zero because the two opposite charges are equidistant from the nucleation point and their effects are compensated. In Fig. 7.8(b) we find a summary of the vortex chirality and polarity behaviors as a function of θ_a. We thus confirm that these results are the same as the numerical ones obtained in Fig. 7.6.

7.4 Chapter Summary and Conclusions

In this chapter we have seen that in a thin soft ferromagnetic cylinder of nanometer size the different competing energies favour a magnetic vortex state. This state minimized the magnetostatic energy at the expense of the exchange one. However in this geometry a specific state of chirality and polarity at remanence can not be determined a priori with an in-plane magnetic field.

A simple geometrical modification of the dot has been proposed. By saturating this dot and then decreasing quasistatically the field, the vortex that appears at near zero field depends only on the direction of the field. This procedure allows to prepare the desired vortex state at remanence.

In spite of the complexity of the micromagnetic model used here, the control of the vortex state can be summarized with two simple rules.

CHAPTER 8

Exchange Bias in Cylindrical Nanomagnets

The phenomenon of exchange bias (EB) or exchange anisotropy was first observed by Meiklejohn and Bean in the 50's [195] in the study of Co particles with its oxidized antiferromagnetic shell (CoO). EB occurs when cooling a ferromagnetic-antiferromagnetic coupled system through the Néel temperature (T_{N}) of the antiferromagnet (with $T_{\mathrm{c}} > T_{\mathrm{N}}$) in the presence of an applied magnetic field [196, 197]. The most well known effect is a shift of the hysteresis loop when the field is applied in the field-cool (FC) direction. This property is used in giant magnetoresistance based read heads to pin a reference ferromagnetic layer whilst keeping another layer free to sense the direction of the magnetic field [2, 144].

In this chapter we introduce an extension of the micromagnetic model presented in Chapter 6 describing the experimentally observed effects that an antiferromagnetic layer produces to the hysteresis loop of a ferromagnetic layer.

8.1 Exchange Bias Phenomenology and Existing Models

In antiferromagnetic materials spins are oriented anti-parallel because its exchange integral J is negative (see Sec. 1.3) and therefore the bulk material has no net macroscopic magnetization. At the interface layer between the ferromagnetic and antiferromagnetic material the antiferromagnetic moments can be compensated (no net magnetic moment) or uncompensated (all spins in the layer pointing the same direction)[198]. It is the exchange coupling of these antiferromagnetic interfacial spins with its homologous ferromagnetic ones that creates the EB effect. The coupling results in a shift of the hysteresis loop of the ferromagnetic layer by a quantity H_{b} (bias field) along the field-cool direction. This shift can be interpreted as a unidirectional (as opposed to uniaxial) anisotropy because spins have its minimum of energy along one direction only.

In addition, also a widening of the hysteresis loop is observed, i.e. an enhancement of the coercivity in the hysteresis loop of the ferromagnetic phase.

Different models to explain EB have been proposed [198, 199] and can be divided into two groups, depending on the AFM interface. The first group explains EB in compensated interfaces. The original model leading to EB in this kind of interfaces, proposed by Meiklejohn and Bean [200], assumed an interface layer completely frozen in the field-cool direction. Even though this model could describe the shift of the hysteresis loop H_b, its value was too large compared to the experiment. Mauri [201] proposed a simple model to reduce the bias field consisting on the relaxation of the AFM material accommodating a domain wall along its thickness (assumed infinite). In this model, the antiferromagnetic moments of the first interface layers can be dragged by the interfacial ferromagnetic spins due to the exchange coupling. Similar models have been proposed using this philosophy [202, 203, 204] but the main picture is as follows: for sufficiently thin AFM layer, the exchange coupling between FM and AFM layers is large enough to drag all the AFM spins to their equilibrium position along the opposite direction of the easy axis, leading to a uniaxial anisotropy (larger coercivity). For large AFM thickness the AFM can accommodate a reversible domain wall when the field is applied in the opposite direction to the cooling field. The difference of energies between the distributions with a domain wall and without it results in the shift of the hysteresis loop.

The second group of models tries to study EB in perfectly compensated interfaces. In these interfaces it is difficult to explain EB because the AFM interface has the same number of spins pointing opposite directions and therefore their averaged effect over the FM is null. In order to break this symmetry, Malozemoff [205] proposed a model in which the AFM surface is rough, this is, there appear small bumps in the AFM interface. These bumps, or defects, are randomly oriented giving rise to formation of domains (perpendicular to the interface) in the AFM, predicting very reasonable values of H_b. In another work Koon [206] calculated theoretically that compensated interface AFM spins present a spin-flop structure [7] with perpendicular alignment to the ferromagnetic spins. Schulthess and Butler [207] showed later that Koon's model would lead to a uniaxial anisotropy instead of unidirectional but allowing the spins to rotate in 3D [208] and including AFM defects at the interface leads to an effective explanation of EB in compensated interfaces.

In order to shine some light on which is the exact mechanism in EB systems, experiments have focused on the study of the interface separating the ferromagnetic and antiferromagnetic phases. It was found that EB occurs in both compensated [209] and uncompensated [210] interfaces. Measurements along the AFM interface [211, 212, 213, 214] and thickness [215] have resulted in a non-zero net magnetic moment component suggesting that some AFM spins are uncompensated (do not have its AFM counterpart). These uncompensated defects support the theory of Malozemoff [205] and there is a strong believe [216] that EB occurs due to a fraction of uncompensated spins that are pinned (frozen) in the field-cool direction.

The bias effect can be modeled without taking into account the microstructure of the interface as a uniform field in the field-cool direction [217]. However here we propose a rather more complex model consisting on a fully compensated interface with some defects on it capturing the physics of the experiments. These defects are considered as macroscopic (avoiding the details of the spin structure) in the micromagnetic framework.

8.2 Modeling Exchange Bias in Micromagnetic Formalism

In the following we consider a Permalloy dot with 504 nm of diameter and 30 nm of thickness with negligible crystalline anisotropy, a saturation magnetization $M_\mathrm{s} = 8 \times 10^5$ A/m and exchange constant $A = 1.3 \times 10^{-11}$J/m. For our simulation the sample is discretized in 6 nm sided cubes ($l_\mathrm{ex} = 5.7nm$). The dot is exchange biased to an antiferromagnet and both are field-cooled along the positive y direction. This antiferromagnet is simulated as an extra micromagnetic layer attached below the dot (see inset of Fig. 8.1) in which each micromagnetic site has zero magnetization (compensated sites) except some randomly chosen defects, which can be seen as a macroscopic average of uncompensated spins of the antiferromagnet. Defects in the antiferromagnet are of two types pinned (PIN) and unpinned (UPIN) [218]. The pinned defects are micromagnetic sites that have an infinite uniaxial anisotropy along the FC direction. Therefore, since they are initially saturated in the FC direction, cannot be switched with a finite applied field and so they remain fixed. The other kind of defects, the unpinned, have the same uniaxial anisotropy axis as the pinned ones but smaller anisotropy constant $K_{upin} = 5 \times 10^5$ J/m^3, which is of the order of magnitude found in IrMn [218]. These defects are able to rotate along with the FM due to the exchange coupling with it. The total number of defects considered is around 16% (900 micromagnetic cells), this is similar to the percentage of pinned uncompensated spins at the interface measured in several experiments [214, 212]. No exchange interaction is assumed among defects.

A symmetric hysteresis loop for this dot without AFM is shown in the black line of Fig. 8.1. Due to the dimensions considered, the reversal mechanism observed is via a vortex state formation as indicated by the shape of the hysteresis loop and the magnetization distribution shown in Fig. 8.2. Adding an antiferromagnetic layer with all its defects pinned (red line in Fig. 8.2) results in a shift of the hysteresis loop of 290 Oe. One way to understand the shift is by considering the asymmetry of the distributions when the sample is saturated along the field-cool direction and opposite to it. In the first case, the AFM sites point in the same direction as the FM ones, therefore the resultant exchange energy is very small. In the second case, the FM point oppositely to the AFM defects resulting in a large exchange energy. This excess of energy needs for a larger applied field (i.e. applied field energy) to reverse the magnetization oppositely to the FC direction resulting in a shift in the loop. Another way to see this effect is by considering that all the pinned spins make a constant effective exchange field along the field-cool direction and therefore shift the loop.

Blue line of Fig. 8.1 shows the case where all the defects are unpinned. Here,

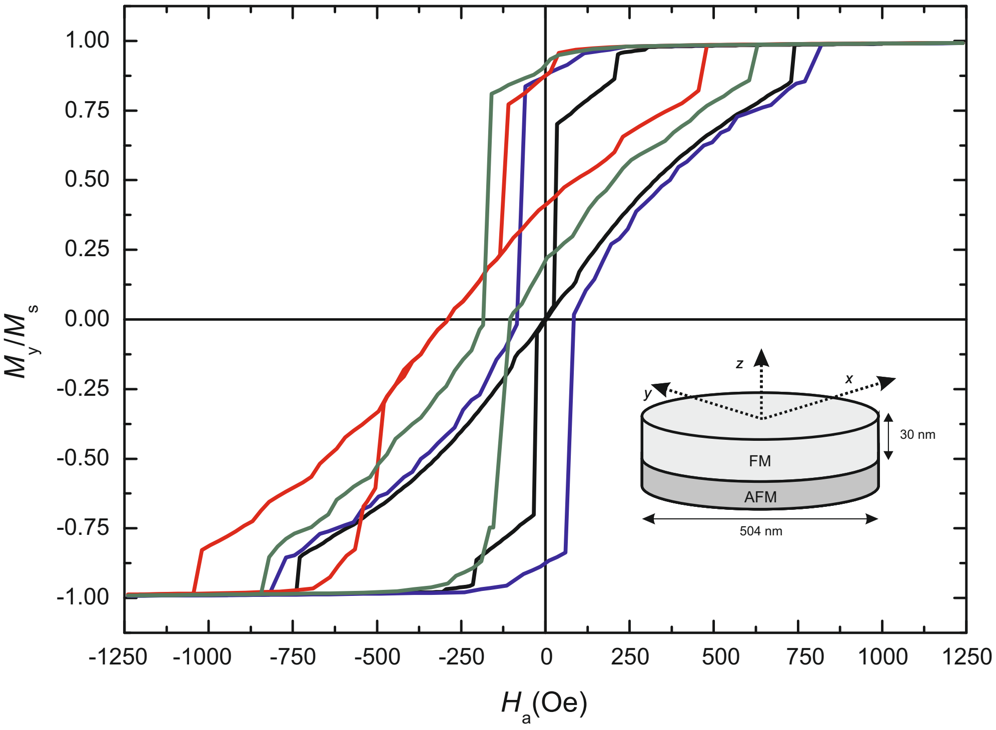

Figure 8.1: Magnetization loop along the y direction for a Permalloy dot of diameter 504 nm and thickness 30 nm attached to an AFM layer of the same diameter. The sample is FC along the positive y direction. Black, blue, green and red are the curves without defects, 900 defects unpinned, 400 pinned-500 unpinned, and 900 pinned. The inset shows a sketch of the FM and the attached AFM.

the hysteresis loop is not shifted because, contrary to the previous case, the energy of the saturated state along the FC direction and opposite to it is the same. This is, in both cases AFM sites point in the same direction as the FM ones. Comparing to the case without AFM (black line in Fig. 8.1) a larger coercivity (160 Oe of total width) is observed because the FM sites have to drag their underlying AFM sites due to the exchange coupling. However, AFM sites have two preferential directions (along the field-cool axis) making more difficult to reverse them, and in turn their exchange coupled FM sites. The difficulty on reversing the magnetization is observed in the blue line of Fig. 8.1 because the vortex nucleates and annihilates at larger fields in both, the initial and the reversed curves.

Up to now, we have seen that pinned defects make a shift of the hysteresis loop whereas the unpinned ones make it broader. The hysteresis loop a combination of both defects (400 pinned and 500 unpinned, for example) is shown in Fig. 8.1 in green line. In this case, a simultaneous loop shift and an increase in coercivity are observed. The bias field is reduced to practically half the value obtained in the case of all the defects pinned. The same occurs with the coercivity comparing to the case with all the defects unpinned. This suggests that bias and anisotropy scale linearly with the number of pinned and unpinned defects, respectively. A deeper study of both effects as a function of the number of defects will be further developed in Sec. 8.4.

Different loops with the same number and type of defects have been performed. Since the defects are randomly distributed we have obtained similar results as those presented in this section.

8.3 Distortion of an Exchange Biased Vortex

Due to the interfacial nature of the exchange bias phenomenon, a distortion of the magnetization distribution along the thickness of the ferromagnet is expected. In this section we analyze the difference in the magnetization distribution of the numerical ferromagnetic layer closer to the AFM (interface layer) and the layer of the FM farther from the interface (free layer).

In Fig. 8.2 we plot the magnetization distribution when the vortex state is centered (no net in-plane magnetization) for the cases of Fig. 8.1. The centered vortex is at zero applied field for the case without defects but at a non zero field for the other cases. Black and green (below black) arrows in each plot are the magnetizations of the free and interface layers, respectively, and the underlying colors indicate the difference in each component of the magnetization between the interface (i) and free (f) layers. Red for $m_{p,i} - m_{p,f} > 0$, blue for $m_{p,i} - m_{p,f} < 0$ and white for no difference. p is the magnetization component (x, y or z).

In the case without defects no difference should be observed in the region where the magnetization is in-plane because there is no asymmetry along the thickness. These regions are marked in white in the upper row of Fig. 8.2. However a clear difference in the x and y components of the magnetization can be observed in the region of the vortex core as shown in Figs. 8.2(i-1) and 8.2(i-2). Here, the out-of-plane magnetization (wich in this case points $+z$ direction) breaks the symmetry along the thickness. In order to understand how the magnetization changes along the thickness a schematic representation of the vortex core has been drawn in Fig. 8.3. As explained in the previous chapter, the vortex core magnetization lines up in order to minimize the exchange energy. However, if the magnetization was perfectly aligned along the z direction magnetostatic energy would be very large. To reduce this energy, the magnetization bends radially in the vortex core so that the surface magnetic pole density is reduced [see the signs in Fig. 8.3(a)] with respect to the uniform case. The same radial distortion of the magnetization but with opposite sign is undergone by the uppermost layer and the lowermost layer (black and green arrows, respectively) as depicted in Fig. 8.3(b). It is noteworthy that no difference in the z component of the magnetization is observed in Fig. 8.2(i-3), this is because we have only plotted the difference between the uppermost layer and the lowermost layer which, as shown in Fig. 8.3(a), have the same m_z. However, in Fig. 8.3(a) we see that in fact m_z also changes along the thickness.

Looking at the cases with defects, we may notice is that the m_z component of the magnetization practically does not change along the thickness as shown by the white and soft-colored zones in the right-most panels of Fig. 8.2. m_z is, in fact almost zero

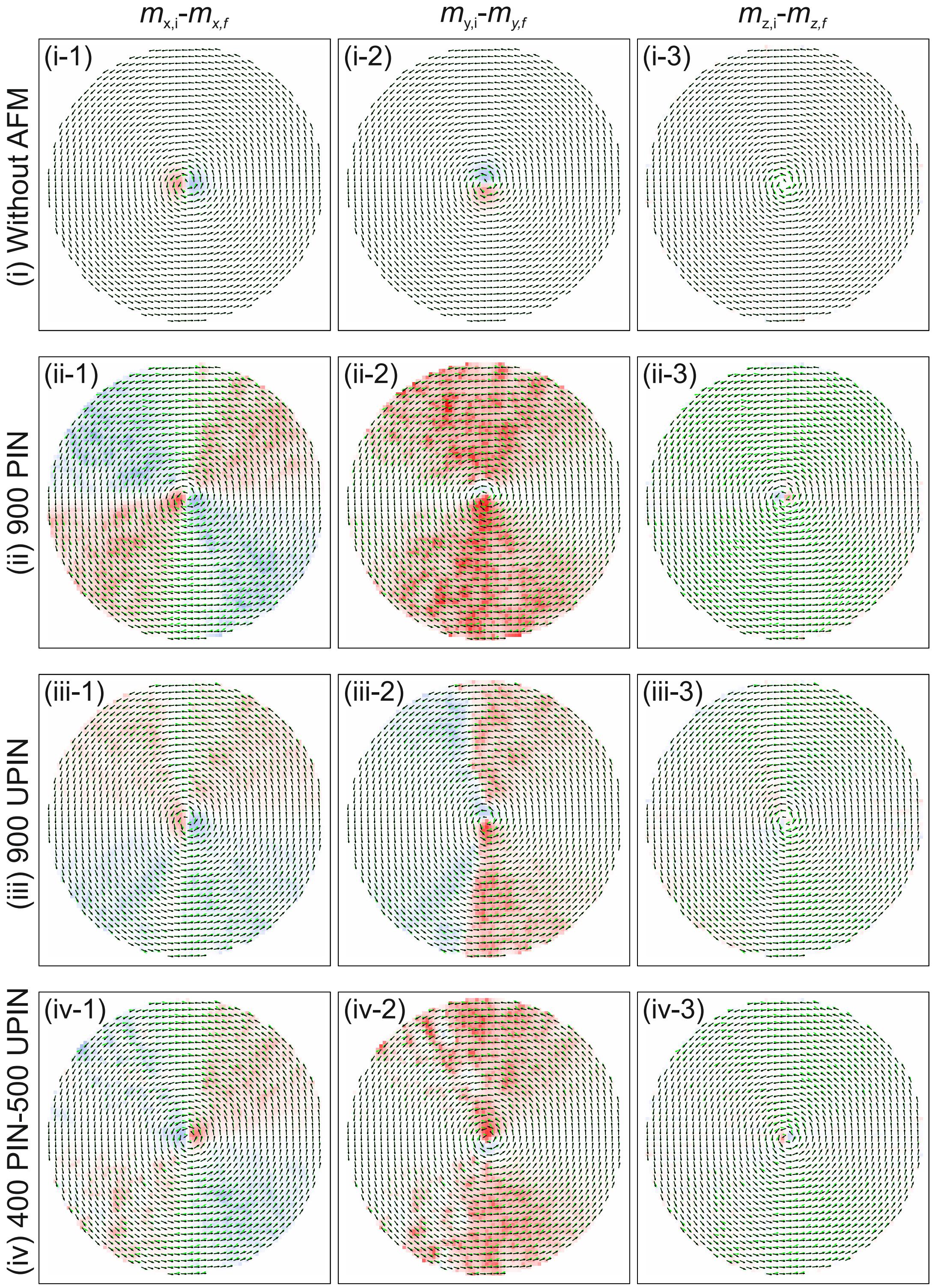

Figure 8.2: Magnetization distribution of a centered vortex state in the FM for the cases without antiferromagnet (zero defects), 900-PIN, 900-UPIN and 400-PIN 500-UPIN indicated by rows i, ii, iii and iv, respectively. The in-plane magnetization distribution for the interface FM layer and the free FM layer are represented by the green and black arrows, respectively. The same distribution of arrows is plotted in each row. Colors in the first, second and third columns (labeled with numbers 1,2 and 3) represent the quantities $m_{x,i} - m_{x,f}$, $m_{y,i} - m_{y,f}$ and $m_{z,i} - m_{z,f}$, respectively. This is, the difference of each component of the unit magnetization vector between the interface layer and the free layer with red positive (0.75 difference), blue negative (-0.75 difference) and white zero.

everywhere except in the vortex core where the magnetization distortion mechanism is the same as explained before. However, in the cases with AFM, a slight difference in m_z is observed in the vortex core due to the asymmetry induced by the defects. In all the cases with defects, the main magnetization distortion will be in-plane.

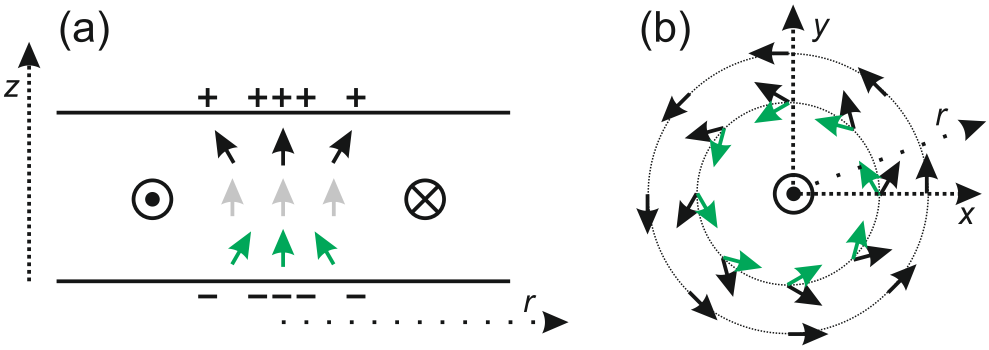

Figure 8.3: (a) Schematic representation of the magnetization vector projection on a plane perpendicular to the thickness in the region of the vortex core. The core in this case points in the z positive direction (up). Colors black and green represent the upper and lower layers along the thickness of the FM, respectively and plus and minus signs indicate the magnetic pole density induced in these surfaces. (b) In-plane projection of the magnetization vector at the vortex core. x, y and z axis are indicated in the figure and r represents an arbitrary radial direction. Dot an cross indicate the magnetization direction perpendicular to the paper plane.

In the second row of Fig. 8.2 we represent the difference between the interface and free layers for the case of an AFM with 900 defects pinned. Contrary to the case without AFM, here we not only observe a thickness distortion in the vortex core but in almost all the vortex. In this case, the symmetry between the interface and free layers is broken due to the pinned defects of the AFM shown in Fig. 8.5(a).

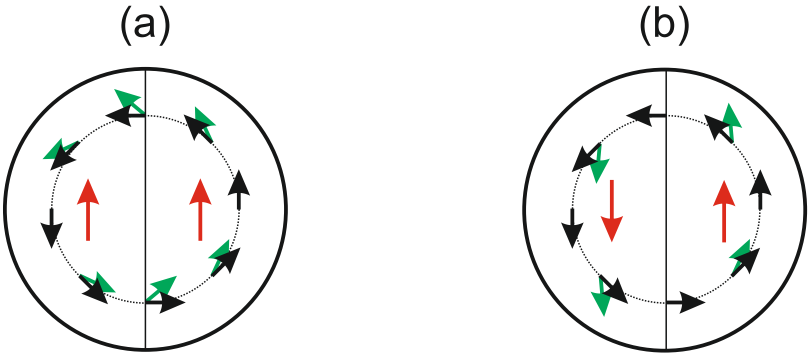

Figure 8.4: Schematic representation of the magnetization vector deviation of the interface layer (green arrows) with respect to the free layers (black arrows) for the cases in which the AFM has only pinned sites (a) or only unpinned sites (b). Red arrows indicate the direction of deviation. Vortex core is not shown here.

The free layer has a magnetization shape closer to a perfect vortex compared to the interface layer [see Fig. 8.4(a)] because it is less affected by the defects and as a consequence has the shape of minimum energy (vortex state). The interface layer, however, is distorted with respect to the perfect vortex [green arrows in Fig. 8.4(a)]. The distortion is in the field-cool direction because of the unidirectional exchange field produced by the defects and takes its maximum when the magnetization is more deviated from the field-cool direction [see red color in Fig. 8.2(ii-2) or green arrows in Fig. 8.4(a)]. In the regions where the magnetization points in the same direction to the field-cool ($+y$), it does not change along the thickness because the interface layer is aligned with the AFM defects minimizing the exchange energy. When the magnetization is aligned opposite to the field-cool direction ($-y$) the exchange energy is maximum but the magnetization is also unchanged because of the collective effect of the other neighbors.

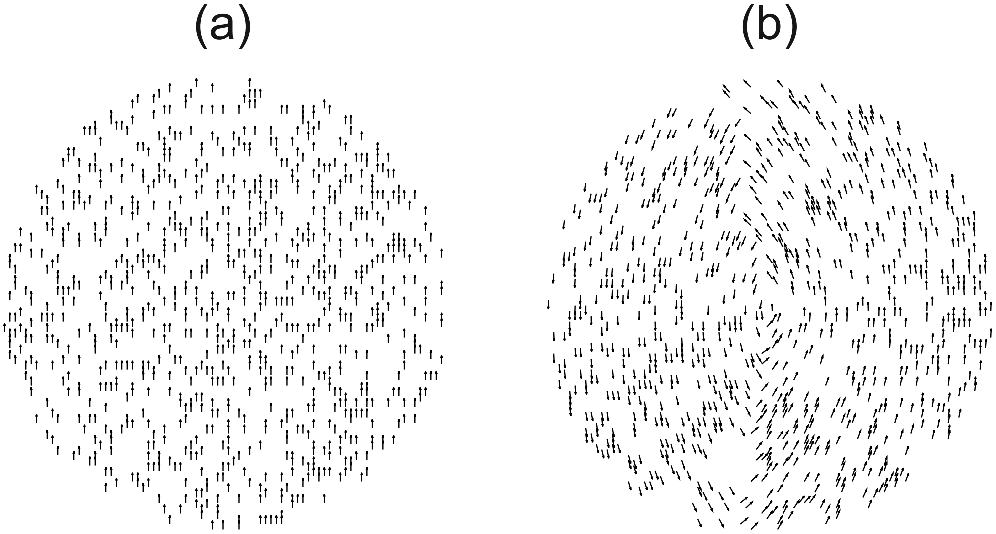

Figure 8.5: Defects at the AFM interface when the FM presents a vortex state. In case (a) 900 pinned defects and in (b) 900 unpinned defects, corresponding to Fig. 8.2(ii) and Fig. 8.2(iii), respectively.

For 900 unpinned defects, a different distortion pattern for m_{y} is observed in Fig. 8.2(iii)[and schematically in Fig. 8.4(b)]. These defects have two easy directions and therefore, the magnetization of the interface layer will bend in the field-cool direction if the magnetization has $+m_y$ component and opposite to the FC direction if the magnetization has $-m_{\mathrm{y}}$ component. This can be seen schematically by the red and green arrows in Fig. 8.4(b) and by the colors and arrows in Fig. 8.2(iii-2). Minimum magnetization distortion is in the region where the magnetization points to $+y$ and $-y$ directions (as in the case of 900 pinned) and in the small region where m_{y} changes of sign because the anisotropy field by the defects reaches zero. Contrary to the pinned defects, the unpinned ones are able to rotate with the FM and form an elongated vortex due to the uniaxial anisotropy as shown in Fig. 8.5(b). This result, the impression of the vortex state in the AFM has already been observed experimentally [219].

The combination of pinned and unpinned defects in the AFM is shown in the bottom row of Fig. 8.2. A similar distortion to the case with pinned defects is found indicating

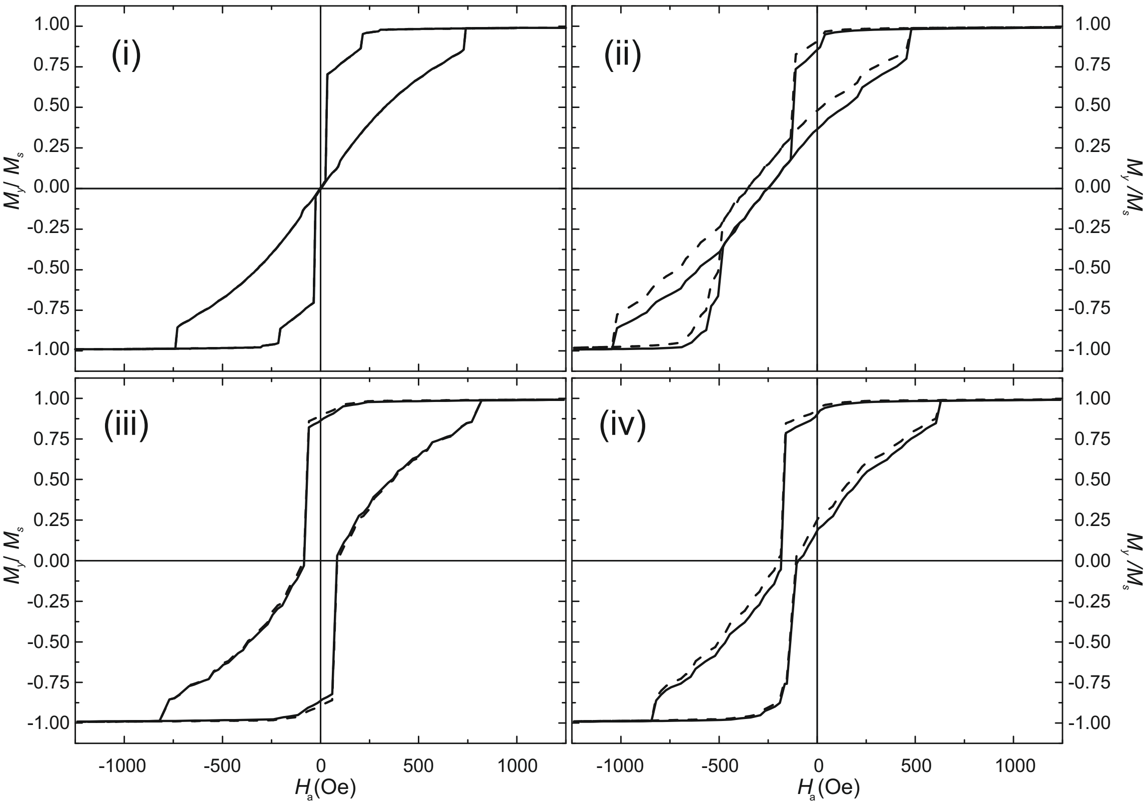

Figure 8.6: Same hysteresis loops as in Fig. 8.1 showing the interface layer (dashed line) and the free layer (solid line) magnetizations normalized to the saturation magnetization of one layer. i,ii,iii and iv are the cases without defects, 900 pinned, 900 unpinned and 400 pinned-500 unpinned, respectively (same as rows in Fig. 8.2).

that even though there are more unpinned defects the appreciable distortion is produced by the pinned ones. However, this distortion is significantly smaller if we compare the color of Figs. 8.2(ii-2) and 8.2(iv-2) because there are less pinned defects in the second case.

The vortex distortion is not only appreciable in the magnetization configuration but in the hysteresis loop itself. In Fig. 8.6 we show the hysteresis loop for the interface and free layers in the same cases of Figs. 8.1 and 8.2. Here we have only represented the magnetization along the field direction (FC direction) because even though there is a local distortion of the vortex in the x and z directions, they compensate and no net difference between the layers is observed. This can be understood by looking at the colors of the difference in m_x and m_z of Fig. 8.2.

As expected, no change in the loop is found for the case without defects [Fig. 8.6(i)] so that the two curves collapse. When the defects are pinned the magnetization of the interface layer (dashed line) is vertically shifted (towards larger M_y) in all the points of the hysteresis loop as shown in Fig. 8.6(ii). It is therefore difficult to reverse the magnetization opposite to the FC direction but easier to do so when the field is along the FC direction. When all the defects are unpinned [see Fig. 8.6(iii)] it is difficult to reverse the interfacial layer in both branches, the initial and the reverse ones due to the uniaxial nature of the defects. This is, the interfacial curve is above the free layer for the initial curve and below it for the reversal one [see Fig. 8.6(iii)]. Even though the separation between the two curves may seem small it has been found systematically in calculations with more unpinned defects (not shown here). Finally, in Fig. 8.6(iv) the 400 pinned defects make an effect similar to the 900 defects [see Fig. 8.6(ii)] although with a much weaker distortion due to the number of pinned defects.

8.4 Effect on the Antiferromagnet Thickness

As mentioned in Sec. 8.1, the bias phenomenon is not only linked to a shift of the hysteresis loop but also to an increase of the coercivity [196, 220, 221]. These two properties vary with the thickness of the AFM giving three distinct behaviors for large, intermediate and thin thicknesses. For thick AFM layers the bias field and the coercivity are independent of the AFM thickness. However, as the thickness is decreased a dramatic reduction of the bias and an increase of coercivity are observed. Further decrease of the thickness reduces the bias field to zero and the coercivity to a small value.

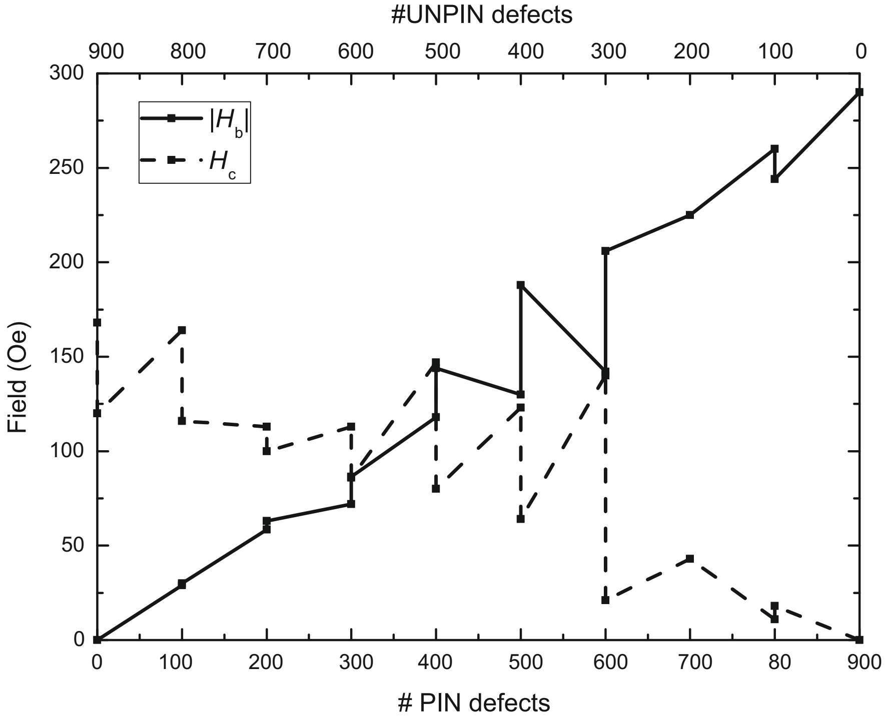

Figure 8.7: Bias (H_b, in absolute value) and coercive (H_c) fields as a function of the type of defects. The total number of defects is 900.

Our purpose is to explain the AFM thickness dependence of bias and coercivity in the intermediate thickness regime. To do so, we assume that the number of interfacial defects (900 in total) is fixed because the interface does not change, however as the thickness changes so does the type of defects. In thick AFM layers only pinned defects are considered leading to a large bias, whereas for thin ones we just consider unpinned defects whose effect is an increase of coercivity as explained in Sec. 8.2.

Bias and anisotropy as a function of the type of defects is shown in Fig. 8.7. To obtain each of this pair of values (bias and coercivity) we have performed a complete hysteresis loop twice so as to take into account two sets of random positions of the defects. Different randoms lead to quite different values of bias and coercivity for the same number and type of defects. This fact can be attributed to the change of nucleation field for the vortex. This is, at fields where the vortex is about to nucleate, it presents a metastable state whose symmetry may be easier or more difficult to break depending on the position of the defects, thus the random. This effect leads to large variation of coercivities which in turn result in a variation of the calculated bias field. However, the general tendency is that bias and coercivity increase quasi linearly with the number of pinned and unpinned defects, respectively.

8.5 Chapter Summary and Conclusions

In this chapter we have presented an extended version of the micromagnetic model to describe an exchange biased system. Within this framework we have been able to reproduce the two main features observed in the hysteresis loops of an exchange biased FM, a unidirectional anisotropy (bias) and a uniaxial anisotropy (increase in coercivity). A bias is obtained with pinned defects in the AFM and the coercivity with the unpinned ones.

The distortion along the thickness of the vortex state has been analyzed. The layers close to the AFM have a larger distortion due to the interaction with it. The pinned defects distort the vortex along the field-cool direction and the unpinned ones along the FC direction and opposite to it depending on the magnetization direction. These effects can also be observed in the hysteresis loops of the interfacial and free layers.

A simple way to model the behavior of the AFM thickness has been proposed. In this model, a large coercivity and small bias is observed when the AFM is thin whereas a large bias and small coercivity are obtained when the AFM thickness is large. In spite of the disperse values of bias and coercivity a general trend could be observed. However, it is clear that further research in this issue has to be carried out.

CHAPTER 9

Conclusions of the Work and Future Lines

In this thesis we have presented two different ways to model soft ferromagnetic materials and in particular their interaction with other magnetic materials such as superconductors or antiferromagnets. This thesis is divided in two parts, one for each model and their applicable scales.

In the first model we study the physics at large scale of soft ferromagnets. We consider a linear, isotropic, and homogeneous ferromagnetic bar with very large susceptibility and a superconducting bar in the critical state. Both magnetic elements have a rectangular cross section (although other cross sections can be considered) and are infinitely long in the same direction. A functional related to the energy is minimized to obtain the magnetic pole density in the ferromagnet and the current density distribution in the superconductor. The key point of this model is that it can take into account the mutual magnetostatic interaction between the soft ferromagnet and the superconductor, this is currents in the superconductor are affected by poles in the ferromagnet and vice versa.

This model is applied to the study of a soft ferromagnet in different applied magnetic fields, either uniform or non uniform due to permanent magnets. We have seen that, since soft ferromagnets guide and concentrate magnetic fields, the change of geometry of the ferromagnet changes dramatically the field at its surroundings. In particular, one can concentrate or screen the magnetic field of a permanent magnet using a soft ferromagnet. A more practical case of study deals with superconducting levitation using a guideway of permanent magnets. In our case, the guideway consists of two square-sectioned permanent magnets oppositely magnetized with a gap (of the same size as the magnets) in the middle. In this arrangement the maximum magnetic field concentration above the guideway using a soft ferromagnet placed in the gap is achieved when the height of the soft ferromagnet is around 0.6 times the height of the permanent magnet.

The levitation force undergone by a superconductor placed above the optimized guideway is compared with the same guideway without ferromagnet. We analyze the case that the superconductor is zero-field cooled far away from the permanent magnets, descended towards them and then ascended again. We have found that the optimized guideway gives larger values of force because the superconductor is more penetrated by the currents and the field felt by them has a larger horizontal component compared with the case without ferromagnet. However, not only the superconductor gets affected by the ferromagnet, in fact, when the superconductor is near the guideway the ferromagnet gets demagnetized due to the strong fields produced by the currents in the superconductor. The superconductor in the guideway with the soft ferromagnet has been demonstrated to be more stable to vertical and horizontal displacements.

The second model deals with the description of the physics of soft ferromagnets at a nanoscopic scale, this is, at a length that describes well the details of ferromagnetic domains and domain walls at which the behavior of the ferromagnet is highly non linear. The mathematical formulation is based on micromagnetics formalism. The model is applied to the study of a nanoscopic soft ferromagnetic cylinder in which the most stable magnetization pattern is a vortex state consisting of a curling in-plane magnetization (with a certain chirality) and an out-of-plane core (polarity). It is argumented that in this kind of cylinders chirality and polarity can not be controlled using quasistatic uniform applied fields. We have proposed a thickness modulated dot in which this control can be achieved by a simple process of saturating the sample with an in-plane field and then decreasing quasistatically the field up to remanence. In this dot, the control of the vortex chirality and polarity is governed by two simple rules and is achieved by tuning just one parameter, the applied field direction.

The non-linear model is extended to study the case of exchange biased soft ferromagnets. The antiferromagnetic layer is modeled as an extra layer of material with some macroscopic defects randomly distributed along its surface. Two kinds of defects are assumed: the pinned defects are frozen in the field-cool direction and do not respond to any applied field whereas the unpinned ones have a large but finite anisotropy in the field-cool direction. In this approximation, the pinned defects lead to a unidirectional anisotropy (a bias shift) and the unpinned ones explain uniaxial anisotropy (coercivity increment). The model is able to reproduce the main features observed in experimental hysteresis loops of exchange biased systems.

Since exchange bias phenomenon occurs at the interface between the soft ferromagnet and the antiferromagnet it is expected that the magnetization distribution changes in the regions close to the antiferromagnet compared to those far from it. In particular, we have studied the vortex distortion along the thickness of the soft ferromagnet. A net distortion along the field-cool direction is found in the case that pinned defects are present in the antiferromagnet. Also the effect that increasing the thickness of the antiferromanget has on the shape of the hysteresis loop for the ferromagnet has been effectively studied although the random position of the defects blur the tendency of bias and coercivity.

Future works based on the work in this thesis may lead to a deeper understanding of the interaction between soft ferromagnetic materials and other materials. For instance, the interaction between a superconducting vortex pinned due to the field of the core of a magnetic vortex. This effect has already been observed experimentally [43, 44, 45, 47]. Another possible extension of the work is to consider time effects and polarized currents in micromagnetic modeling so as to model more complex magnetic structures such as skyrmions [222, 223, 224, 225].

APPENDIX A

Geometrical Factors for Magnetic Scalar Potential and Magnetic Vector Potential

In this appendix we calculate the factors E_{ij}, Q_{ij}^{SC} of the discretized functional of the FM (3.7) and the factors D_{ij}, Q_{ij}^{FM} coming from the discretized functional of the SC (3.8). The first two are related to the magnetic scalar potential ϕ whereas the other two with the vector potential $\mathbf{A}$.

In all the calculations following we assume the SC and FM elements to be infinitely long in the z direction. The SC element has a cross section $\Delta_x \times \Delta_y$ in the x and y directions respectively whereas the FM element has a length ΔL in its finite direction, that can be either x or y. Further it is considered that the SC element carry a uniform current density $\mathbf{J} = J_z = I/\Delta_x\Delta_y$ along the z direction whilst the FM element has a uniform magnetic pole density σ. The position of each element either the SC or the FM is defined in their respective center and will be denoted as (x_k, y_k) for the k element.

A.1 Magnetic Scalar Potential Over the FM

The energy terms of the functional (3.6) in its discretized form Eq. (3.7) contain the geometrical factors E_{ij} and Q_{ij}^{SC}. The first is the magnetic scalar potential per unit magnetic pole density that creates an element of the FM averaged to another one. The second is the magnetic scalar potential per unit current density created by an element of the SC in the center of an element of the FM.

A.1.1 Calculation of the Matrices E_{ij}

Consider a FM element i with its finite length along the x direction. Magnetic scalar potential per unit magnetic pole density created by such magnetic pole distribution in any point space (x, y) except in the element i is

$$U_i(x, y, x_i, y_i) \equiv \frac{\phi(x, y, x_i, y_i)}{\sigma} = -\frac{1}{4\pi} \int_{x_i-\Delta L/2}^{x_i+\Delta L/2} \ln\left[(x_i - x)^2 + (y_i - y)^2\right] \mathrm{d}x_i. \quad \text{(A.1)}$$

The matrix $E_{i,j}$ is defined as the magnetic scalar potential per unit magnetic pole density of the element i averaged to another element j in the FM. This is mathematically

$$E_{i,j}(x_i, x_j, y_i, y_j) = \frac{1}{\Delta L} \int_{l_j-\Delta L/2}^{l_j+\Delta L/2} U_i(x_j, y_j, x_i, y_i) \mathrm{d}l_j, \quad \text{(A.2)}$$

where l_j is the coordinate of the j element in the finite direction and $\mathrm{d}l_j$ the differential of length in the same direction. In the case that the j element lies in the x direction (parallel to i), $l_j = x_j$ and $\mathrm{d}l_j = \mathrm{d}x_j$ and considering a vertical (along y) separation b between i and j Eq. (A.2) becomes

$$\begin{aligned} E^{\|}_{ij}(x_i, x_j, b) &= \frac{-1}{4\pi\Delta L}\left[f(x_i + \Delta L/2, x_j + \Delta L/2; b)\right. \\ &- f(x_i - \Delta L/2, x_j + \Delta L/2; b) \\ &- f(x_i + \Delta L/2, x_j - \Delta L/2; b) \\ &+ \left. f(x_i - \Delta L/2, x_j - \Delta L/2; b)\right], \end{aligned} \quad \text{(A.3)}$$

where the function $f(u, v; b)$ is

$$\begin{aligned} f(u, v; b) &= -\frac{1}{2}\left[6uv + 4b(u - v)\arctan\left(\frac{u - v}{b}\right)\right. \\ &- \left.(b^2 - (u - v)^2)\ln(b^2 + (u - v)^2)\right]. \end{aligned} \quad \text{(A.4)}$$

For the self interaction (E_{ii}) the two sheets are infinitely close, i.e. $x_j \to x_i$ and $b \to 0$, Eq. (A.3) is the magnetic scalar potential per unit magnetic pole density of the element i over himself,

$$E^{\|}_{ii} = \frac{\Delta L}{4\pi}(3 - \ln(\Delta L^2)). \quad \text{(A.5)}$$

Another possible case is when the j is perpendicular to i ($\mathrm{d}l_j = \mathrm{d}y_j$) then the matrix E_{ij} becomes

$$\begin{aligned} E^{\perp}_{ij}(x_i, y_j; y_i, x_j) &= \frac{1}{4\pi\Delta L}\left[g(x_i - x_j + \Delta L/2, y_i - y_j - \Delta L/2)\right. \\ &- g(x_i - x_j - \Delta L/2, y_i - y_j - \Delta L/2) \\ &- g(x_i - x_j + \Delta L/2, y_i - y_j + \Delta L/2) \\ &+ \left. g(x_i - x_j - \Delta L/2, y_i - y_j + \Delta L/2)\right], \end{aligned} \quad \text{(A.6)}$$

with

$$\begin{aligned} g(u, v) &= v^2 \arctan\left(\frac{u}{v}\right) + u^2 \arctan\left(\frac{v}{u}\right) \\ &+ vu\ln(u^2 + v^2) - 3uv. \end{aligned} \quad \text{(A.7)}$$

Parallel [Eq. (A.3)] and perpendicular [Eq. (A.6)] interactions are symmetric under permutation of their indices ($E_{ij} = E_{ji}$) meaning that the magnetic scalar potential per magnetic pole density created by i over j is the same that j creates over i. All possible interactions between two geometrical infinite sheets are considered in this two equations.

A.1.2 Calculation of Matrices Q_{ij}^{SC}

Consider an element i of the SC. Using Biot-Savart law it is easy to calculate the magnetic field at any point in the space produced by such current distribution, then integrating the $x(y)$ field component on $-x(-y)$ direction we obtain the magnetic scalar potential per current density. The magnetic scalar potential per current density produced by an element i of the SC over the center of the element j (x_j, y_j) in the FM is

$$\begin{aligned}
Q_{ij}^{\mathrm{SC}}(x_i, y_i; x_j, y_j, \Delta_x, \Delta_y) &\equiv \frac{\phi(x_i, y_i; x_j, y_j, \Delta_x, \Delta_y)}{J} = \\
&= \frac{1}{8\pi}\left[4(\alpha - x_j)(\gamma - y_j)\arctan\left(\frac{\alpha - x_j}{\gamma - y_j}\right)\right. \\
&- 4(\alpha - x_j)(\delta - y_j)\arctan\left(\frac{\alpha - x_j}{\delta - y_j}\right) \\
&+ 4(\beta - x_j)(\delta - y_j)\arctan\left(\frac{\beta - x_j}{\delta - y_j}\right) \\
&- 4(\beta - x_j)(\gamma - y_j)\arctan\left(\frac{\beta - x_j}{\gamma - y_j}\right) \\
&+ (\gamma - y_j)^2\ln\left(\frac{(\beta - x_j)^2 + (\gamma - y_j)^2}{(\alpha - x_j)^2 + (\gamma - y_j)^2}\right) \\
&+ (\alpha - x_j)^2\ln\left(\frac{(\alpha - x_j)^2 + (\gamma - y_j)^2}{(\alpha - x_j)^2 + (\delta - y_j)^2}\right) \\
&+ (\gamma - y_j)^2\ln\left(\frac{(\alpha - x_j)^2 + (\delta - y_j)^2}{(\beta - x_j)^2 + (\delta - y_j)^2}\right) \\
&+ \left.(\gamma - y_j)^2\ln\left(\frac{(\beta - x_j)^2 + (\delta - y_j)^2}{(\beta - x_j)^2 + (\gamma - y_j)^2}\right)\right], \qquad \text{(A.8)}
\end{aligned}$$

where α, β, γ and δ are defined as

$$\begin{aligned}
\alpha &= x_i + \Delta_x/2, \\
\beta &= x_i - \Delta_x/2, \\
\gamma &= y_i + \Delta_y/2, \\
\delta &= y_i - \Delta_y/2, \qquad \text{(A.9)}
\end{aligned}$$

and (x_i, y_i) is the center of the element i.

A.2 Potential Vector Over the SC

In the discretized functional (3.8) two geometrical factors D_{ij} and Q_{ij}^{FM} appear. The first is the potential vector per unit current and μ_0 that an i element of the SC produces to another one. The second is the vector potential per unit magnetic pole density and μ_0 produced by an element i of the FM to the center of an element j in the SC. In the following we use the gauge $\nabla \cdot \mathbf{A} = 0$ (Coulomb gauge) so that the vector potential is in the same direction of the current density ($\mathbf{A} = A_z\mathbf{k}$) with $\mathbf{k}$ the unit vector in z.

A.2.1 Calculation of Matrices $D_{i,j}$

Considering an i element of the SC we can calculate the magnetic vector potential using the one created by a wire and summing up for the i cross section. Then, the magnetic vector potential of the element i on any point space (x, y) outside i per unit current and μ_0

$$\begin{aligned} A'_z(x,y;x_i,y_i) &\equiv \frac{A_z(x,y;x_i,y_i)}{\mu_0 I} = -\frac{1}{4\pi}\left[g(x-x_i-\Delta_x/2, y-y_i-\Delta_y/2)\right. \\ &- g(x-x_i+\Delta_x/2, y-y_i-\Delta_y/2) \\ &- g(x-x_i-\Delta_x/2, y-y_i+\Delta_y/2) \\ &+ \left. g(x-x_i+\Delta_x/2, y-y_i+\Delta_y/2)\right], \end{aligned} \tag{A.10}$$

where $g(u, v)$ is the function defined previously, Eq. (A.7). Considering another element j in the SC, the coefficient D_{ij}, is the average over j cross section of the vector potential per unit current and μ_0 generated by the element i, this is

$$D_{ij} = \frac{1}{\Delta_x\Delta_y}\int_{x_j-x_i-\Delta_x/2}^{x_j-x_i+\Delta_x/2} \mathrm{d}x \int_{y_j-y_i-\Delta_y/2}^{y_j-y_i+\Delta_y/2} \mathrm{d}y A'_z(x,y;x_i,y_i). \tag{A.11}$$

When inserting Eq. (A.10) in Eq. (A.11) we obtain

$$\begin{aligned} D_{ij} &= \frac{-1}{4\pi\Delta_x\Delta_y}\left[h(x_j-x_i+\Delta_x/2, y_j-y_i+\Delta_y/2, \Delta_x, \Delta_y)\right. \\ &- h(x_j-x_i-\Delta_x/2, y_j-y_i+\Delta_y/2, \Delta_x, \Delta_y) \\ &- h(x_j-x_i+\Delta_x/2, y_j-y_i-\Delta_y/2, \Delta_x, \Delta_y) \\ &+ \left. h(x_j-x_i-\Delta_x/2, y_j-y_i-\Delta_y/2, \Delta_x, \Delta_y)\right], \end{aligned} \tag{A.12}$$

with $h(u, v; t, d)$ defined as

$$\begin{aligned} h(u,v;t,d) &= G(u+t, v+d) - G(u-t, v+d) \\ &- G(u+t, v-d) + G(u-t, v-d), \end{aligned} \tag{A.13}$$

where

$$\begin{aligned} G(l,k) &= -\frac{25}{24}l^2k^2 \\ &- \frac{1}{24}(k^4+l^2-6l^2k^2)\ln(l^2+k^2) \\ &+ \frac{l^3k}{3}\arctan\left(\frac{k}{l}\right)+\frac{lk^3}{3}\arctan\left(\frac{l}{k}\right). \end{aligned} \tag{A.14}$$

As in the calculation of the matrices E_{ij}, D_{ij} is symetric under permutation of their indices ($D_{ij} = D_{ji}$).

A.2.2 Calculation of Matrices Q_{ij}^{FM}

For an i element of the FM it is easy to obtain the magnetic field distribution and then integrating the $x(y)$ of the field on the $y(-x)$ direction we find the vector potential created by a sheet with uniform magnetic pole distribution.

In the case that the i element lies in the horizontal direction x, the potential vector over the center of an element j of the SC per unit magnetic pole density and μ_0 is

$$\begin{aligned} Q_{ij}^{\mathrm{FM}}(x_j,y_j,y_i,\alpha,\beta) &= \frac{A(x_j,y_j,y_i,\alpha,\beta)}{\mu_0\sigma} = \frac{1}{4\pi}\left[2(\beta-x_j)\arctan\left(\frac{y_j-y_i}{\beta-x_j}\right)\right. \\ &- 2(\alpha-x_j)\arctan\left(\frac{y_j-y_i}{\alpha-x_j}\right) \\ &+ \left.(y_j-y_i)\ln\left(\frac{(y_j-y_i)^2+(\beta-x_i)^2}{(y_i-y_j)^2+(\alpha-x_j)^2}\right)\right], \end{aligned} \tag{A.15}$$

where α and β are defined as

$$\begin{aligned} \alpha &= x_i+\Delta L/2, \\ \beta &= x_i-\Delta L/2. \end{aligned} \tag{A.16}$$

However, if the FM element is in the y direction the factor Q_{ij}^{FM} is calculated as $Q_{ij}^{\mathrm{FM}}(y_j,x_j,x_i,\gamma,\delta)$ where the factors γ and δ are

$$\begin{aligned} \gamma &= y_i+\Delta L/2, \\ \delta &= y_i-\Delta L/2. \end{aligned} \tag{A.17}$$

APPENDIX B

Magnetostatic Field Interaction Matrix

Consider a uniformly magnetized (along a direction $\mathbf{m}_j = (m_{jx}, m_{jy}, m_{jz})$ with $|\mathbf{m}_j| = 1$) ortorrombic cell j with sides Δ_x, Δ_y and Δ_z in the x, y and z directions, respectively. The center of this cell is at the distance $\mathbf{r}_j = (x_j, y_j, z_j)$ from the origin. The center of a second cell i with the same dimensions is located at a distance $\mathbf{r}_i = (x_i, y_i, z_i)$. Then the demagnetizing field at i averaged through all its volume due to the cell j is written as

$$\mathbf{H}_{d,ij} = M_\mathrm{s} \begin{pmatrix} \eta_{ij}^{xx} & \eta_{ij}^{xy} & \eta_{ij}^{xz} \\ \eta_{ij}^{yx} & \eta_{ij}^{yy} & \eta_{ij}^{yz} \\ \eta_{ij}^{zx} & \eta_{ij}^{zy} & \eta_{ij}^{zz} \end{pmatrix} \begin{pmatrix} m_{jx} \\ m_{jy} \\ m_{jz}. \end{pmatrix} = M_\mathrm{s} \eta_{ij} \mathbf{m}_j, \tag{B.1}$$

where η_{ij} is the interaction matrix [163]. A general component of the matrix $\eta_{ij}^{\zeta_1,\zeta_2}$ must be understood as the ζ_1 (x, y or z) component of the field averaged over a cell i normalized to M_s due to another cell j magnetized in the ζ_2 (x, y or z) direction. For instance η_{ij}^{xy} is the x component of the field at i normalized to M_s due to a cell j magnetized in the y direction.

It is important to notice that due to the reciprocity theorem [9, 150] η_{ij} is symmetric and therefore only six terms must be evaluated [151]. Due to the symmetry of the interactions only two mathematical expressions are needed to compute the six terms, an off-diagonal term and a diagonal term. We calculate first a diagonal term.

The z field component at the center of a cell i (not averaged and normalized to M_s) due to a cell j uniformly magnetized in the z direction can be calculated as

$$h_{ij}^{zz} = \frac{1}{4\pi} \sum_{\alpha,\beta,\gamma=0}^{1} (-1)^{\alpha+\beta+\gamma+1} \arctan\left(\frac{(x_i - x_{\alpha j})(y_i - y_{\beta j})}{(z_i - z_{\gamma j}) D(i, x_{\alpha j}, y_{\beta j}, z_{\gamma j})} \right). \tag{B.2}$$

In this equation

$$\zeta_{\alpha j} \equiv \zeta_j + \frac{\Delta\zeta}{2}(-1)^{\alpha-1} \tag{B.3}$$

are the coordinates ($\zeta = x, y, z$) of the vertices of the micromagnetic cell j and the distance between each vertex of the j cell and the center of i is defined by

$$D(i, x_{\alpha j}, y_{\beta j}, z_{\gamma j}) = \sqrt{(x_i - x_{\alpha j})^2 + (y_i - y_{\beta j})^2 + (z_i - z_{\gamma j})^2}. \tag{B.4}$$

The matrix component η_{ij}^{zz} is defined as the average over the volume of the i cell of the quantity h_{ij}^{zz}

$$\eta_{ij}^{zz} = \frac{1}{\Delta_x \Delta_y \Delta_z} \int\int\int h_{ij}^{zz} \mathrm{d}x_i \mathrm{d}y_i \mathrm{d}z_i, \tag{B.5}$$

where the integral is performed through all the volume of the cell i.

To obtain the other diagonal terms (η_{ij}^{xx} and η_{ij}^{yy}) one just have to make permutations of all the variables in Eq. (B.2) and calculate its average as in Eq. (B.5).

For the off diagonal terms of the matrix η_{ij} we calculate for instance the x component of the field at the center of a cell i due to a cell j uniformly magnetized in the z direction as

$$h_{ij}^{xz} = -\frac{1}{4\pi} \sum_{\alpha,\beta,\gamma=0}^{1} (-1)^{\alpha+\beta+\gamma+1} \ln |y_i - y_{\beta j} + D(i, x_{\alpha j}, y_{\beta j}, z_{\gamma j})|. \tag{B.6}$$

As before, the averaged quantity of Eq. (B.6) is the quantity η_{ij}^{xz} and therefore can be written as

$$\eta_{ij}^{xz} = \frac{1}{\Delta_x \Delta_y \Delta_z} \int\int\int h_{ij}^{xz} \mathrm{d}x_i \mathrm{d}y_i \mathrm{d}z_i. \tag{B.7}$$

The other off-diagonal terms η_{ij}^{xy} and η_{ij}^{yz} can be obtained by permutations of all the variables in Eq. (B.6) and then calculating the average.

A simple and shorter [167] way to express η_{ij}^{zz} and η_{ij}^{xy} is

$$\eta_{ij}^{zz} = \sum_{\alpha,\beta,\gamma,\alpha',\beta',\gamma',=0}^{1} (-1)^{\alpha+\beta+\gamma+\alpha'+\beta'+\gamma'} \quad F \quad (z_{ij} + z_{\gamma i} - z_{\gamma' j} \\ , \quad x_{ij} + x_{\alpha i} - z_{\alpha' j}, y_{ij} + y_{\beta i} - y_{\beta' j}),$$

$$\eta_{ij}^{xz} = \sum_{\alpha,\beta,\gamma,\alpha',\beta',\gamma',=0}^{1} (-1)^{\alpha+\beta+\gamma+\alpha'+\beta'+\gamma'} \quad G \quad (y_{ij} + y_{\beta i} - y_{\beta' j} \\ , \quad z_{ij} + z_{\gamma i} - z_{\gamma' j}, x_{ij} + x_{\alpha i} - x_{\alpha' j}),$$

where x_{ij}, y_{ij} and z_{ij} are the components of the vector $\mathbf{r}_i - \mathbf{r}_j$ and the functions F and

G are defined as

$$\begin{aligned} F(z;x,y) &= xyz\arctan\left(\frac{xy}{zd}\right)+\frac{1}{2}x(y^2-z^2)\ln(|d-x|) \\ &+ \frac{1}{2}y(x^2-z^2)\ln(|d-y|)+\frac{1}{6}(x^2+y^2-2z^2)d, \qquad \text{(B.8)} \\ G(y;z,x) &= -xyz\ln(d+y)+\frac{1}{6}x(x^2-3y^2)\ln(z+d) \\ &+ \frac{1}{6}z(x^2-3y^2)\ln(d+x)+\frac{1}{2}z^2y\arctan\left(\frac{xy}{zd}\right) \\ &+ \frac{1}{2}x^2y\arctan\left(\frac{zy}{xd}\right)+\frac{1}{6}y^3\arctan\left(\frac{xz}{yd}\right)+\frac{1}{3}xzd, \qquad \text{(B.9)} \end{aligned}$$

respectively with $d=\sqrt{x^2+y^2+z^2}$.

In micromagnetic calculations where a magnetic sample is discretized in a regular (equi-spaced) array of N ortorrombic cells, the number of matrices needed would be N^2. This is, for the field evaluation at each cell the contribution of all the others must be taken into account. The matrix η_{ij} depends only on three parameters, that are the absolute value of the relative positons between cells i and j. Therefore η_{ij} only depends on $|x_i-x_j|$, $|y_i-y_j|$ and $|z_i-z_j|$ and the number of independent matrices reduces to N.

APPENDIX C

Solution of Standard Problem # 2

Different problems analyzing the behavior of magnetic particles have been proposed by the National Institute of Standards and Technology (NIST) [226]. The aim of this initiative is to identify numerical problems between the modeling community.

In this appendix we analyze standard problem # 2 in order to verify our numerical procedure compared to other reports [166, 227, 228]. In this problem, a rectangular magnetic particle with lengths $5d, d$ and $0.1d$ in the x, y and z directions (see Fig. C.1), respectively is set in a uniform applied field in the (1,1,1) direction. The characteristic exchange length of the material is l_{ex} defined as in section 6.3. In this appendix all calculations will be performed with a convergence criterion $\epsilon = 10^{-5}$ without randomizing the magnetization distribution after each applied field.

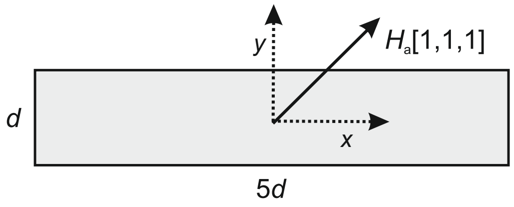

Figure C.1: Schematic representation of the particle shape. x and y axis are shown in dotted arrows whereas z axis is out-of-plane. A uniform field is applied in the (1,1,1) direction, this is, at an angle $\arccos\left[1/\sqrt{3}\right]$ (54.74 degrees approximately) from each of the coordinate axis.

In Fig. C.2 a hysteresis loop of a particle with size $d/l_{\text{ex}} = 15$ is shown. In this calculation we have used an in-plane square mesh of $\Delta_x = \Delta_y = l_{\text{ex}}$ and an out-of-plane cell size $\Delta_z = 1.5 l_{\text{ex}}$. For the computation of the demagnetizing field no coarser mesh has been used (see Sec. 6.3.4).

The particle size is comparable to the exchange length and for this reason it will be almost uniformly magnetized. At a large field, the magnetization points the direction of the field. However, taking a closer look at the individual components of the magnetization M_x, M_y and M_z on Fig. C.2 we see that at large field $M_\mathrm{x} > M_\mathrm{y} > M_\mathrm{z}$. The reason is that the quasi-uniform magnetization distribution favors the magnetization along the longest particle axis in order to minimize the magnetostatic energy. This fact can be understood comparing the demagnetizing factors [5, 229] of this prism.

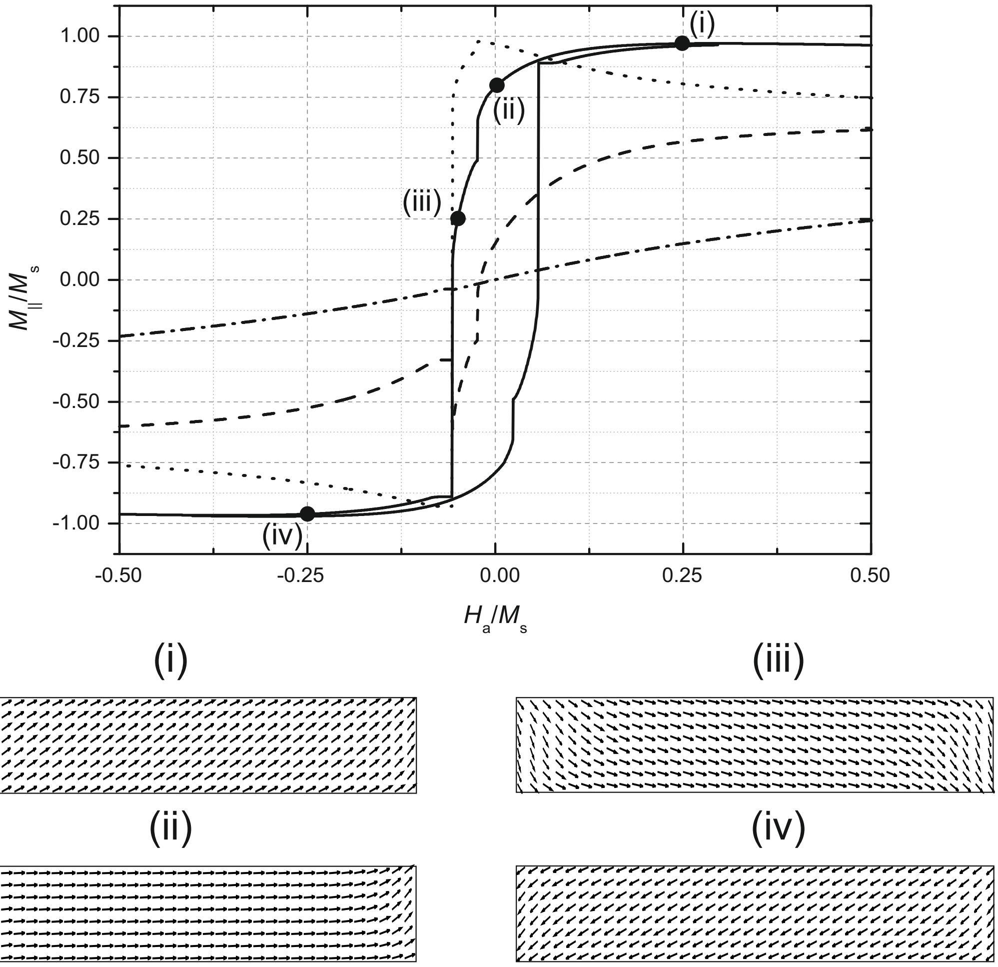

Figure C.2: Hysteresis loop of a particle with $d/l_\mathrm{ex} = 15$. Solid line indicates the magnetization in the applied field direction. Dotted, dashed and dashed-dotted represent the magnetization in the x, y and z directions, respectively for the initial curve only. In the insets, we show different magnetization distributions corresponding to the applied fields $H_\mathrm{a}/M_\mathrm{s} = 0.25, 0, -0.05, -0.25$ for i,ii,iii and iv, respectively. These points are marked in the initial curve of the hysteresis loop.

At remanence (zero applied field) the particle gets magnetized along the longest direction (x direction), however a small canting in the edges of the particle exist [see Fig. C.2 (ii)] . This canting follows the positive y direction as a reminiscence of the previous applied field forming an "S-state" (also found in [227] for a particle of $d/l_\mathrm{ex} = 12$) that reduces the surface magnetic pole density. The pole reduction helps to decrease the magnetostatic energy compared to the uniform state case.

Further decrease of the applied field make the interior zone of the particle to rotate more rapidly than the edges in the direction of the field. This rotation goes on up to a sharp jump in the hysteresis loop that corresponds to a rapid change of the sign of M_y as shown in Fig. C.2 (iii). A second larger jump in the hysteresis loop can be observed. This change of magnetization uniformly rotates the magnetization passing though the $-y$ direction up to the full alignment with the field (see Fig. C.2 (iv)).

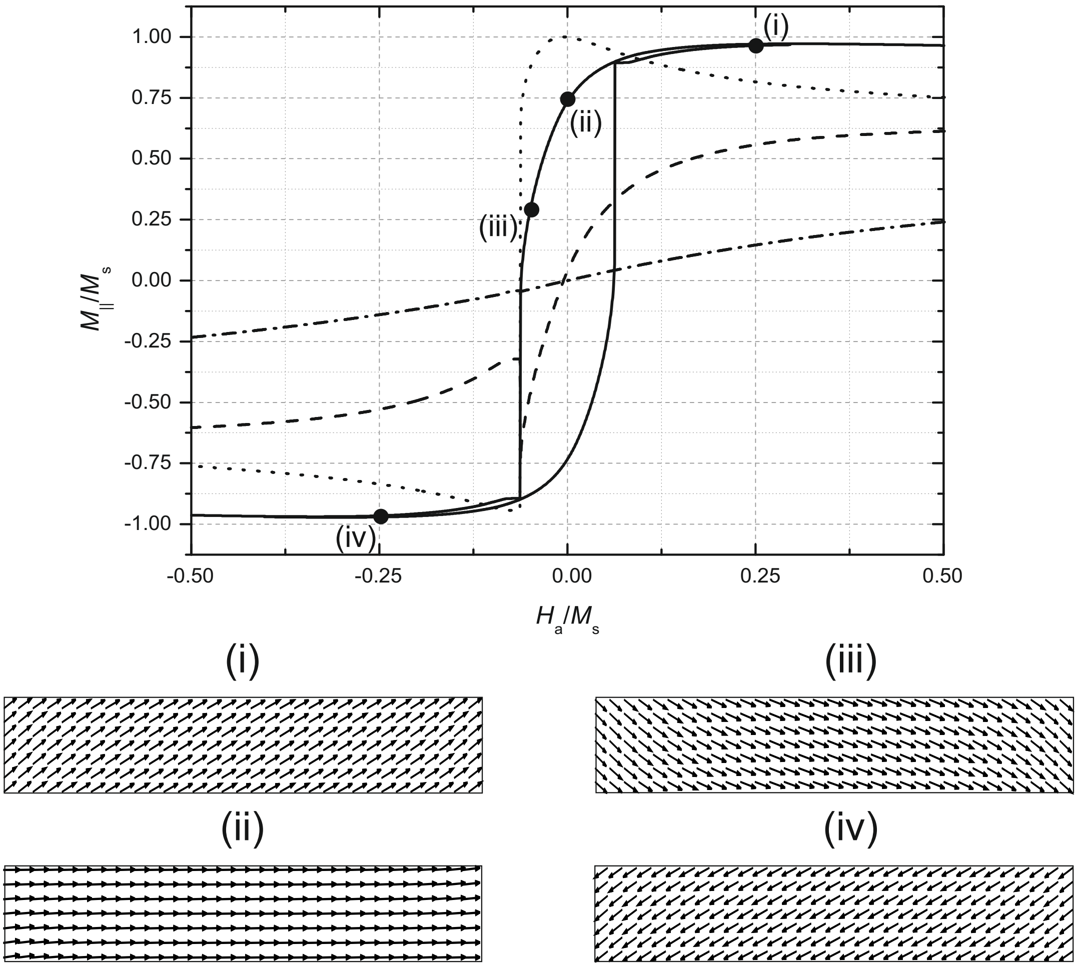

Figure C.3: Same as Fig. C.2 but with particle size $d/l_\mathrm{ex} = 5$.

In Fig. C.3 we show the same hysteresis loop as in Fig. C.2 but for a smaller particle of size $d/l_\mathrm{ex} = 5$. In this calculation the micromagnetic cells are cubic with side $\Delta_x = \Delta_y = \Delta_z = 0.25 l_\mathrm{ex}$. As opposed to the previous calculation we use a second coarser grid with parameters $n_x = n_y = n_z = 2$ to evaluate the demagnetizing field (see Sec. 6.3.4).

Since the particle is very small compared to the exchange length the exchange energy dominates and the particle remains almost uniformly magnetized through all the hysteresis loop. This means that both the initial (from positive field to negative field) and reversal (from negative field to positive field) curves occur via coherent rotation of the magnetization as can be seen in the insets of Fig. C.3. At remanence [see Fig. C.3 (ii)] this particle is much more uniformly magnetized in the x direction than in the larger particle tending to minimize the magnetostatic energy. In fact, as the size of the particle tend to zero, the remanent magnetization must be $M_{\mathrm{x}}/M_{\mathrm{s}} = 1$. i.e. perfectly magnetized along the x direction. To see this in Fig C.4 we show the x component of the remanent magnetization as a function of the particle size d in two different calculations, using 12 neighbors and 6 neighbors [161] for the evaluation of the exchange field.

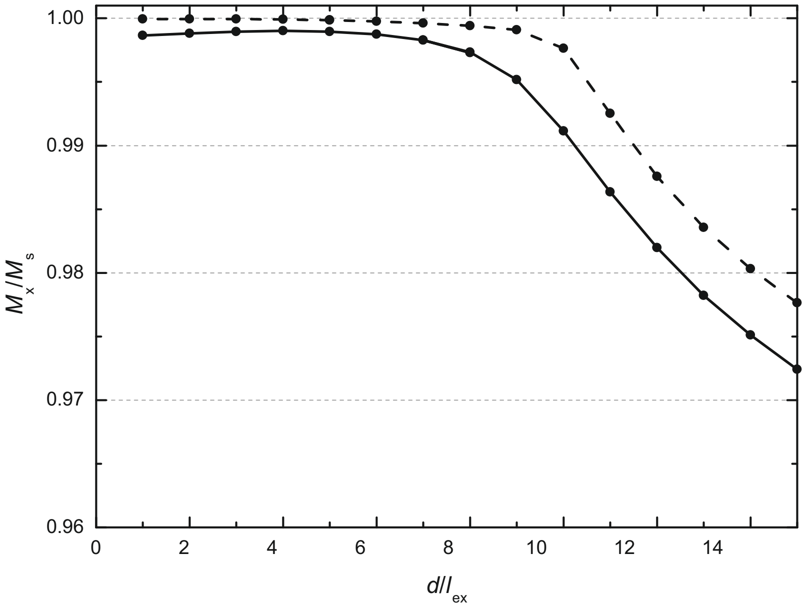

Figure C.4: x component of magnetization at remanence as a function of the particle size d. Solid and dashed line correspond to the same calculation but using 6 neighbors and 12 neighbors [161], respectively for the computation of the exchange field.

In Fig. C.4 we see that for very small particles the remanent magnetization lies along the x direction as expected. The size at which the x component of the magnetizaton at remanence has a sharp decrease due to the S-state is about $d/l_{\mathrm{ex}} = 10$ as found by other authors in [227, 226]. This sets the quantitative limit for the particle to be uniformly magnetized.

In Fig. C.4 we see that the 6 neighbor approximation slightly underestimates the exchange field because for small particles the remanence $M_{\mathrm{x}}/M_{\mathrm{s}}$ is not as close to 1 as the 12 neighbor case. However these two curves are very similar (notice the range of M_{x} in Fig. C.4) and therefore since we do not need to reproduce such detail, all calculations in this thesis are performed using 6 neighbors. The same occurs with the convergence criterion. Although in this problem we have used $\epsilon = 10^{-5}$ because we need more accuracy, $\epsilon = 10^{-4}$ is used in all the thesis. For smaller ϵ the calculation of hysteresis loops has no significant difference neither on the shape of the loop nor in the magnetization distributions.

Bibliography

[1] A. Aharoni, *Introduction to the Theory of Ferromagnetism* (Oxford University Press, Oxford, 1996).

[2] J. M. D. Coey, *Magnetism and Magnetic Materials* (Cambridge University Press, 2010).

[3] J. D. Jackson, *Classical Electrodynamics* (New York: John Wiley & Sons, 1975).

[4] D.-X. Chen, J. A. Grug and R. B. Goldfarb, IEEE Trans. Magn. **27**, 3601 (1991).

[5] D.-X. Chen, E. Pardo, and A. Sanchez, IEEE Trans. Magn. **41**, 2077 (2005).

[6] G. Bai, R. W. Gao, Y. Sun, G. B. Han, and B. Wang. J. Magn. Magn. Mat. **308**, 20 (2007).

[7] B. D. Cullity, *Introduction to Magnetic Materials* (John Wiley & Sons, Hoboken, New Jersey, 2009).

[8] W. F. Brown, Jr., Rev. Mod. Phys. **17**, 15 (1945).

[9] W.F. Brown Jr. *Magnetostatic Principles in Ferromagnetism* (North-Holland, Amsterdam, 1962).

[10] H. Kronmuller, M. Fahnle, *Micromagnetism and the Microstructure of Ferromagnetic Solids* (Cambridge University Press, Cambridge, 2003).

[11] W. F. Brown Jr., J. Appl. Phys. **39**, 993 (1968).

[12] A. C. Rose-Innes and E. H. Rhoderik, *Introduction to Superconductivity* (Oxford: Pergamon Press, 1969).

[13] P. G. de Gennes, *Superconductivity of Metals and Alloys* (Reedwod City: Addison-Wesley, 1989).

[14] C. P. Poole Jr, H. A. Farach, and R. J. Creswick, *Superconductivity* (San Diego: Academic Press, 1995).

[15] M. Cyrot and D. Pavuna, *Introduction to superconductivity and high-*T_c *materials. (Singapore: World Scientific, 1992).*

[16] A. A. Abrikosov, Sov. Phys. JETP **5**, 1174 (1957).

[17] C. P. Bean, Phys. Rev. Lett. **8**, 250 (1962).

[18] C. P. Bean, Rev. Mod. Phys. **36**, 31 (1964).

[19] D. -X. Chen and R. B. Goldfarb, J. Appl. Phys **66**, 2489 (1989).

[20] D. -X. Chen, A. Sanchez, J. Nogués, and J. S. Muñoz, Phys. Rev. B **41**, 9510 (1990).

[21] R. B. Godfarb, M. Lelental, and C. A. Thompson, *Magnetic Susceptibility of Superconductors and Other Spin Systems*, R. A. Hein, T. L. Francavilla, D. H. Liebenberg, New York (1991).

[22] D.-X. Chen and A. Sanchez, J. Appl. Phys. **70**, 5463 (1991).

[23] A. Sanchez, Physica C **255**, 136 (1994).

[24] F. Gömöry, Supercond. Sci. Technol. **10**, 523 (1997).

[25] F. Gömöry, R. Tebano, A. Sanchez, E. Pardo, C. Navau, I. Husek, F. Strycet, and P. Kovac, Supercond. Sci. Technol. **15**, 1311 (2002).

[26] A. Palau, T. Puig, X. Obradors, E. Pardo, C. Navau, A. Sanchez, A. Usoskin, H. C. Freyhardt, L. Fernández, B. Holzapfel, R. Feenstra, Appl. Phys. Lett. **84**, 230 (2004).

[27] C. Navau, N. Del-Valle, and A. Sanchez, IEEE Trans. Appl. Supercond. **23**, 1051 (2013).

[28] D. Larbalestier, A. Gurevich, M. Feldmann, and A. Polyanskii, Nature **414**, 368 (2001).

[29] M. W. Rupich, X. Li, S. Sathyamurthy, C. L. H. Thieme, K. DeMoranville, J. Gannon, and S. Fleshler, IEEE Trans. Appl. Supercond. **23** 6601205, (2013).

[30] H. Song, P. Brownsey, Y. Zhang, J. Waterman, T. Fuushima, and D. Hazelton, IEEE Trans. Appl. Supercond. **23**, 4600806 (2013).

[31] A. C. Wulff, O. V. Mishin, N. H. Andersen, Y. Zhao, J.-C. Grivel, Mat. Lett. **92**, 386 (2013).

[32] D. W. Hazelton, V. Selvamanickam, J. M. Duval, D. C. Larbalestier, W. D. Markiewicz, H. W. Weijers, and R. L. Holtz, IEEE Trans. Appl. Supercond. **19**, 2218 (2009).

[33] X. D. Xue, K. W. E. Cheng, and D. Sutanto, Supercond. Sci. Thechnol. **19**, R31 (2006).

[34] N. Koshizuka, Phys. C **445**, 113 (2006).

[35] J. Tang, J. Fang, and W. Tong, IEEE Trans. Appl. Supercond. **22**, 5702109 (2012).

[36] G. Snitchler, B. Gamble, and S. S. Kalsi, IEEE Trans. Appl. Supercond. **15**, 2206 (2005).

[37] N. Mathias, M. Steurer, Supercond. Sci. Thechnol. **20**, R15 (2007).

[38] J. R. Hull, S. Hanany, T. Matsumara, B. Juhnson, and T. Jones, Supercond. Sci. Technol. **18**, S1 (2005).

[39] S. R. Foltyn, L. Civale, J. L. Macmanus-Driscoll, Q. X. Jia, B. Maiorov, H. Wang and M. Maley, Nature Mater. **6**, 631 (2007).

[40] N. Del-Valle, C. Navau, A. Sanchez, R. B. Dinner, AIP Adv. **2**, 022166 (2012).

[41] N. Del-Valle, C. Navau, A. Sanchez, and D.-X. Chen, Appl. Phys. Lett. **98**, 202506 (2011).

[42] A. Palau, H. Parvaneh, N. A. Stelmashenko, H. Wang, J. L. Macmanus-Driscoll, and M. G. Blamire, Phys. Rev. Lett. **98**, 117003 (2007).

[43] T. Shapoval, V. Metlushko, M. Wolf, V. Neu, B. Holzapfel, L. Schultz, Phys. C Supercond.**470**, 867 (2010).

[44] T. Shapoval, V. Metlushko, M. Wolf, V. Neu, B. Holzapfel, V. Neu, and L. Schultz, Phys. Rev. B **81**, 092505 (2010).

[45] A. Hoffmann, P. Prieto, V. Metlushko, I. K. Schuller, J. Supercond. Nov. Magn. **25**, 2187 (2012).

[46] A. Hoffmann, L. Fumagalli, N. Jahedi, J. C. Sautner, J. E. Pearson, G. Mihajlovic and V. Metlushko, Phys. Rev. B **77**, 060506 (2008).

[47] A. V. Silhanek, N. Verellen, V. Metlushko, W. Gillijns, F. Gozzini, B. Ilic, V. V. Moshchalkov, Phys. C **468**, 563 (2008).

[48] F. Gomory, M. Vojenciak, E. Pardo, and J. Souc, Supercond. Sci. Technol. **22**, 034017 (2009).

[49] M. D. Ainslie, W. Yuan, T. J. Flack, IEEE Trans. Appl. Supercond. **23**, 4700104 (2013).

[50] E. H. Brandt, Science **243**, 349 (1989).

[51] S. Earnshaw, Tran. Cambridge Philos. Soc. **7**, 97 (1842).

[52] F. C. Moon, *Superconducting levitation*, Wiley, New York (1994).

[53] M. V. Berry and A. K. Geim, Eur. J. Phys. 18, 307 (1997).

[54] M. D. Simon, A.K. Geim, J. Appl. Phys. **87**, 6200 (2000).

[55] A. R. Qian, D. C. Yin, P. F. Yang, Y. Lv, Z. C. Tian, P. Shang, IEEE Trans. Appl. Supercond. **23**, 1051 (2013).

[56] M. Donolato, A. Torti, N. Kostesha, M. Deryabina, E. Sogne, P. Vavassori, M. F. Hansen, R. Bertacco, Lab. Chip **11**, 2976 (2011).

[57] E. H. Brandt, Am. J. Phys. **58**, 43 (1990).

[58] R. M. Stephan, R. de Andrade, Jr., G. C. dos Santos, M. A. Neves, and R. Nicolsky, Physica C **386**, 490 (2003).

[59] W. Yang, M. Qiu, Y. Liu, Z. Wen, Y. Duan, and X. Chen, Supercond. Sci. Technol. **20**, 281 (2007).

[60] S. Wang, J. Wang, X. Wang, Z. Ren, Y. Zeng, C. Deng, H. Jiang, M. Zhu, G. Lin, Z. Xu, D. Zhu and H. Song, IEEE Trans. Appl. Supercond. **13**, 2134 (2003).

[61] J. Wang, S. Wang, Y. Zeng, H. Huang, F. Luo, Z. Xu, Q. Tang, G. Lin, C. Zhang, Z. Ren, G. Zhao, D. Zhu, S. Wang, H. Jiang, M. Zhu, C. Deng, P. Hu, C. Li, F. Liu, J. Lian, X. Wang, L. Wang, X. Shen, and X. Dong, Physica C **378-381**, 809 (2002).

[62] L. Schultz, O. de Haas, P. Verges, C. Beyer, S. Rohlig, H. Olsen, L. Kuhn, D. Berger, U. Noteboom, and U. Funk, IEEE Trans. Appl. Supercond. **15**, 2301 (2005).

[63] R. M. Stephan, R. Nicolsky, M. A. Neves, A. C. Ferreira, R. de Andrade, Jr., M. A. Cruz Moreira, M. A. Rosario, and O. J. Machado, Physica C **408-410**, 932 (2004).

[64] Gareth P. Hatch, GeoScienceWorld **8**(5), 341 (2012).

[65] J. Wang, S. Wang and J. Zheng, IEEE Trans. Appl. Supercond. **19**, 2142 (2009).

[66] G. G. Sotelo, D. H. N. Dias, R. de Andrale Jr and R. M. Stephan, IEEE Trans. Appl. Supercond. **21**, 1464 (2011).

[67] G. G. Sotelo, D. H. N. Dias, O. J. Machado, E. D. David, R. de Andrale Jr., R. M. Stephan and G. C. Costa, J. of Phys. Conf. Series **234**, 032054 (2010).

[68] N. Amemiya and M. Nakahata, Physica C 463-465, 775 (2007).

[69] Y. A. Genenko, H. Rauh, and P. Kruger, Appl. Phys. Lett. **98**, 152508 (2011).

[70] F. Gomory, M. Vojenciak, E. Pardo, M. Solovyov, and J. Souc, Supercond. Sci. Technol. **23**, 034012 (2010).

[71] Y. Mawatari, Phys. Rev. B **77**, 104505 (2008).

[72] Y. A. Genenko, A. Snezhko, and H. C. Freyhardt, Phys. Rev. B **62**, 3453 (2000).

[73] E. Pardo, J. Souc, and M. Vojenciak, Supercond. Sci. Technol. **22**, 075007 (2009).

[74] A. Sanchez, N. Del-Valle, C. Navau, and D.-X. Chen, Appl. Phys. Lett. **97**, 072504 (2010).

[75] Y. B. Kim, C. F. Hempstead, and A. R. Strnad, Phys. Rev. Lett. **9**, 306 (1962).

[76] L. Prigozhin, J. Comp. Phys. **129**, 190 (1996).

[77] L. Prigozhin, IEEE Trans. Appl. Supercond **7**, 3866 (1997).

[78] A. Badia and C. Lopez, Phys. Rev. Lett. **87** 127004 (2001); A. Badia and C. Lopez, Phys. Rev. B **65** 104514 (2002).

[79] K. V. Bhagwat, S. V. Nair, and P. Chaddah, Physica C **227**, 176 (1994).

[80] A. Sanchez and C. Navau, Phys. Rev. B **64**, 214506 (2001).

[81] C. Navau and A. Sanchez, Phys. Rev. B **64**, 214507 (2001).

[82] E. Pardo, A. Sanchez, D.-X. Chen, and C. Navau, Phys. Rev. B **71**, 134517 (2005).

[83] E. Pardo, A. Sanchez, and C. Navau, Phys. Rev. B **67**, 104517 (2003).

[84] A. Sanchez, N. Del-Valle, E. Pardo, D.-X. Chen, and C. Navau, J. Appl. Phys. **99**, 113904 (2006).

[85] L. Prigozhin, J. Comput. Phys. **129**, 190 (1996).

[86] A. H. Morrish, *The Physical Principles of Magnetism* (Wiley, 1965).

[87] O. Gutfleisch , M. A. Willard , E. Bruck , C. H. Chen , S. G. Sankar , and J. P. Liu, Adv. Mater **23**, 821 (2011).

[88] E. H. Brandt, Phys. Rev. B **54**, 4246 (1996).

[89] A. Forkl, H. Kronmüller, Phys. Rev. B **52**, 16130 (1995).

[90] E. Pardo, D.-X. Chen, A. Sanchez, and C. Navau, Supercond. Sci. Technol. **17**, 16130 (2004).

[91] K. V. Bhagwat and P. Chaddah, Phys. C Supercond. **190**, 444 (1992).

[92] K. V. Bhagwat and D. Karmakar, Pramana **57**, 763 (2001).

[93] N. Del-Valle, A. Sanchez, C. Navau, and D.-X. Chen, IEEE Trans. Appl. Supercond. **19**, 2070 (2009).

[94] N. Del-Valle, A. Sanchez, C. Navau, and D.-X. Chen, J. Low Temp. Phys. **162**, 62 (2011).

[95] A. Sanchez, N. Del-Valle, C. Navau, and D.-X. Chen, J. Appl. Phys. **105**, 023906 (2009).

[96] D.-X. Chen, C. Prados, E. Pardo, A. Sanchez, and A. Hernando, J. Appl. Phys. **91**, 5254 (2002).

[97] J. R. Reitz, F. J. Milford, and R. W. Christy, *Foundations of the Electromagnetic Theory* (Reading [Mass.]: Addison-Wesley, 1979).

[98] L. D. Landau, E. M. Lifshitz, and L. P. Pitaevskii, *Electrodynamics of Continuous Media* (Oxford: Pergamon Press, 1984).

[99] R. de Andrale, Jr., J. A. A. S. Cardoso, G. C. dos Santos, L. B. de Cicco, A. F. G. Fernandes, M. A. P. Rosario, M. A. Neves, A. P. de Suza, A. Ripper, G. C. da Costa, R. Nicolsky, and R. M. Stephan, IEEE Trans. Appl. Supercond. **13**, 2271 (2003).

[100] J. Wang, S. Wang, C. Deng, J. Zheng, H. Song, Q. He, Y. Zeng, Z. Deng, J. Li, G. Ma, H. Jing, Y. Huang, J. Zhang, Y. Lu, L. Liu, L. Wang, J. Zhang, L. Zhang, M. Liu, Y. Qin, and Y. Zhang, IEEE Trans. Appl. Supercond. **17**, 2091 (2007).

[101] M. Qiu, W. Yang, Z. Wen, L. Lin, G. Yang and Y. Liu, IEEE Trans. Appl. Supercond. **16**, 1120 (2006).

[102] H. Song, J. Zheng, M. Liu, L. Zhang, Y. Lu, Y. Huang, Z. Deng, J. Zhang, H. Jing, S. Wang, J. Wang, IEEE Trans. Appl. Supercond. **16**, 1023 (2006).

[103] H. Jing, J. Wang, S. Wang, L. Wang, L. Liu, J. Zheng, Z. Deng, G. Ma, Y. Zhang, and J. Li, Physica C **463-465**, 426 (2007).

[104] L. Zhang, J. Wang, Q. He, J. Zhang and S. Wang, Phys. C Supercond. **459**, 33 (2007).

[105] W. Liu, S. Y. Wang, H. Jing, J. Zheng, M. Jiang, and J. S. Wang, Physica C **468**, 974 (2008).

[106] G. T. Ma, Q. X. Lin, J. S. Wang, S. Y. Wang, Z. G. Deng, Y. Y. Lu, M. X. Liu, and J. Zheng, Supercond. Sci. Technol. **21**, 065020 (2008).

[107] Z. Deng, J. Wang, J. Zheng, H. Jing, Y. Lu, G. Ma, L. Liu, W. Liu, Y. Zhang, and S. Wang, Supercond. Sci. Technol. **21**, 115018 (2008).

[108] G. G. Sotelo, D. H. N. Dias, R. de Andrale, Jr., R. M. Stephan, N. Del-Valle, A. Sanchez, C. Navau, and D.-X. Chen, IEEE Trans. Appl. Supercond. **21**, 3532 (2011).

[109] S. Wang, J. Wang, Z. Ren, H. Jiang, M. Zhu, X. Wang, and Q. Tang, IEEE Trans. Appl. Supercond. **11**, 1808 (2001).

[110] Z. Ren, J. Wang, S. Wang, H. Jiang, M. Zhu, X. Wang and X. Shen, Phys. C, Supercond. **378**, 873 (2002).

[111] X. Wang, J. Wang, S. Wang, Z. Ren, H. Song, J. Zheng and X. Shen, Phys. C, Supercond **390**, 113 (2003).

[112] Z. Ren, Phys. C, Supercond. **384**, 159 (2003).

[113] W. Yang, Z. Wen, Y. Duan, X. Chen, M. Qiu, Y. Liu, and L. Lin, IEEE Trans. Appl. Supercond. **16**, 1108 (2006).

[114] X. Wang, H. H. Song, Z. Y. Ren, M. Zhu, J. S. Wang, S. Y. Wang, and X. Z. Wang, Phys. C, Supercond. **386**, 536 (2003).

[115] H. Song, O de Haas, C. Beyer, G. Krabbes, P. Verges, and L. Schultz, Appl. Phys. Lett. **86**, 192506 (2005).

[116] L. Kuehn, M. Mueller, R. Schubert, C. Beyer, O. de Haas, and L. Schultz, IEEE Trans. Appl. Supercond. **17**, 2079 (2007).

[117] S. Wang, J. Zheng, H. song, X. Wang, and J. Wang, IEEE Trans. Appl. Supercond. **15**, 2277.

[118] D. H. N. Dias, E. S. Motta, G. G. Sotelo, and R. de Andrale, Jr., Supercond. Sci. Technol. **23**, 075013 (2010).

[119] N. Del-Valle, A. Sanchez, E. Pardo, D.-X. Chen, and C. Navau, Appl. Phys. Lett. **90**, 042503 (2007).

[120] N. Del-Valle, A. Sanchez, E. Pardo, C. Navau, and D.-X. Chen, Appl. Phys. Lett. **91**, 112507 (2007).

[121] N. Del-Valle, A. Sanchez, C. Navau, and D.-X. Chen, Supercond. Sci. Technol. **21**, 125008 (2008).

[122] N. Del-Valle, A. Sanchez, C. Navau, and D.-X. Chen, IEEE Trans. Appl. Supercond. **21**, 1469 (2011).

[123] G.-T. Ma, J.-S Wang, and S.-Y. Wang, IEEE Trans. Appl. Supercond **20**, 2228 (2010).

[124] E. S. Motta, D. H. N. Dias, G. G. Sotelo, H. O. C. Ramos, J. H. Norman, and R. M. Stephan, IEEE Trans. Appl. Supercond. **21**, 3548 (2011).

[125] Y. Lu, J. Wang, S. Wang, and J. Zheng, J. Supercond. Novel Magn. **21** 467 (2008).

[126] Y. Lu, B. Lu, and S. Wang, J. Low Temp. Phys. **164**, 279 (2011).

[127] M. Liu, Y. Lu, S. Wang, and G. Ma, J. Supercond. Novel Magn. **24**, 1159 (2011).

[128] Y. Lu, X. Bai, Y. Ge, and J. Wang, J. Supercond. Novel Magn. **24**, 1967 (2011).

[129] Y. Qin and B. Liu, J. Supercond. Novel Magn. **24**, 1357 (2011).

[130] J. F. Herbst, Rev. Mod. Phys. **63**, 819 (1991).

[131] X. Wang, Z. Ren, H. Song, X. Wang, J. Zheng, S. Wang, J. Wang and Y. Zhao, Supercond. Sci. Thechnol. **18**, S99 (2005).

[132] J. Wang, S. Wang, Y. Zeng, H. Huang, F. Luo, Z. Xu, Q. Tang, G. Lin, C. Zhang, Z. Ren, G. Zhao, D. Zhu, S. Wang, H. Jiang, M. Zhu, C. Deng, P. Hu, C. Li, F. Liu, J. Lian, X. Wang, L. Wang, X. Shen, and X. Dong, Physica C **378-381**, 809 (2002).

[133] N. Del-Valle, A. Sanchez, C. Navau, and D.-X. Chen, Appl. Phys. Lett. **92** 042505 (2008).

[134] R. Skomski, J. Phys.: Condens. Matter **15**, R841 (2003).

[135] C. A. Ross, Annu. Rev. Mater. Res. **31**, 203 (2001).

[136] B. D. Terris, and T. Thomson, J. Phys. D: Appl. Phys. **38**, R199 (2005).

[137] M. P. Sharrock, IEEE Trans. Magn. **5**, 4374 (1989).

[138] W. M. Mularie, J. Appl. Phys. **69**, 4938 (1991).

[139] S. N. Piramanayagam, J. Appl. Phys. **102**, 011301 (2007).

[140] M. N. Baibich, J. M. Broto, A. Fert, F. Nguyen Van Dau, F. Petroff, P. Eitenne, G. Creuzet, A. Friederich, and J. Chazelas, Phys. Rev. Lett. **61**, 2472 (1988).

[141] G. A. Prinz, Science **282**, 1660 (1998).

[142] M. E. Flatté, IEEE Trans. Elect. Dev. **54**, 907 (2007).

[143] S. A. Wolf, D. D. Awschalom, R. A. Buhrman, J. M. Daughton, S. von Molnár, M. L. Roukes, A. Y. Chtchelkanova, and D. M. Treger, Science **294**, 1488 (2001).

[144] S. S. P. Parkin, X. Jiang, C. Kaiser, A. Panchula, K. Roche, and M. Samant, Proc. IEEE **91** 661 (2003).

[145] J. C. Slonczewski, J. Magn. Magn. Mat. **159**, L1 (1996).

[146] L. Berger, Phys. Rev. B **54**, 9353 (1996).

[147] E. B. Myers, D. C. Ralph, J. A. Katine, R. N. Louie, R. A. Buhrman, Sicence **285**, 867 (1999).

[148] A. Brataas, A. D. Kent, and H. Ohno, Nat. Mat. **11**, 372 (2012).

[149] S. S. P. Parkin, M. Hayashi, and L. Thomas, Science **320**, 190 (2008).

[150] W.F. Brown Jr. *Micromagnetics* (Willey Interscience, New York, 1963).

[151] J. E. Miltat and M. J. Donahue, 2007. Numerical Micromagnetics: Finite Difference Methods. *Handbook of Magnetism and Advanced Magnetic Materials.*

[152] T. Jourdan, A. Marty and F. Lançon. Phys. Rev. B **77**, 224428 (2008).

[153] C. J. Kriessman, J. Appl. Phys. **34**, 1054 (1963).

[154] N. A. Usov and S. E. Peschany, J. Magn. Magn. Mat. **118**, L290 (1993).

[155] J. Fidler and T. Schrefl. J. Phys. D: Appl. Phys **33**, R135 (2000).

[156] M. Kruzik and A. Prohl. SIAM Rev. **48**, 439 (2006).

[157] M. Labrune and H Miltat, J. Magn. Magn. Mat. **1**51, 231 (1995).

[158] K.Yu. Guslienko and A. N. slavin, Phys. Rev. B, **7**2, 014463 (2005).

[159] A. Aharoni, Phys. B **306**, 1 (2001).

[160] W. Rave, K. Ramstock, A. Hubert, J. Magn. Magn. Mat. **183**, 329 (1998).

[161] M. J. Donahue, D. G. Porter, Phys. B **343**, 177 (2004).

[162] S. Müller-Pfeiffer, M. Schneider and W. Zinn. Phys. Rev. B **49**, 15745 (1994).

[163] M. E. Shabes, A. Aharoni, IEEE Trans. Magn. **23**, 3882 (1987).

[164] M. E. Shabes and H. N. Bertram. J. Appl. Phys. **64**, 1347 (1988).

[165] R. Moskowitz and E. Della-Torre. IEEE TRans. Magn. **2**, 739 (1966).

[166] M. J. Donahue, D. G. Porter, and R. D. McMichael, J. Appl. Phys. **87**, 5520 (2000).

[167] H. Fukushima, Y. Nakatani and N. Hayashi, IEEE Trans. Magn. **34**, 193 (1998).

[168] A. J. Newell, W. Williams, and D. J. Dunlop, J. Geophys. Res. **98**, 9551 (1993).

[169] L. Greengard, Science **265**, 909 (1994).

[170] B. Van de Wiele, F. Olyslager, L. Dupre and D. De Zutter, J. Magn. Magn. Mat. **332**, 469 (2010).

[171] C. Abert, G. Selke, B. Kruger, and A. Drews, IEEE Trans. Magn. **48**, 1105 (2012).

[172] W. H. Press, S. A. Teukolsky, W. T. Vetterling and B. T. Flannery *Numerical Recipes* (Cambridge University Press, Cambridge, 2007)

[173] R. P. Cowburn, D. K. Koltsov, A. O. Adeyeye, and M. E. Welland, Phys. Rev. Lett. **83**, 1042 (1999).

[174] K. L. Metlov, K. Y. Guslienko, J. Magn. Magn. Mat. **242**, 1015 (2002).

[175] T. Shinjo, T. Okuno, R. Hassdorf, K. Shijeto, T. Ono, Science **289**, 930 (2000).

[176] S. Bohlens, B. Krüger, A. Drews, M. Bolte, G. Meier, and D. Pfannkuche, Appl. Phys. Lett. **93**, 142508 (2008).

[177] K. Nakano, D. Chiba, N. Ohshima, S. Kasai, T. Sato, Y. Nakatani, K. Sekiguchi, K. Kobayashi, and T. Ono, Appl. Phys. Lett. **99**, 262505 (2011).

[178] M. Goto, H. Hata, A. Yamaguchi, Y. Nakatani, T. Yamaoka, Y. Nozaki, and H. Miyajima, Phys. Rev. B **84**, 064406 (2011).

[179] B. Van Waeyenberge, A. Puzic, H. Stoll, K. W. Chou, T. Tyliszczak, R. Hertel, M. Fähnle, H. Brückl, K. Rott, G. Reiss, I. Neudecker, D. Weiss, C. H. Back, and G. Schütz, Nature **444**, 461-464 (2006).

[180] K. Yamada, S. Kasai, Y. Nakatani, K. Kobayashi, H. Kohno, A. Thiaville, and T. Ono, Nature Mat. **6**, 269-273 (2007).

[181] K. Y. Guslienko, K.-S. Lee, and S.-K. Kim, Phys. Rev. Lett. **100**, 027203 (2008).

[182] S. Yakata, M. Miyata, S. Nonoguchi, H. Wada, and T. Kimura, Appl. Phys. Lett. **97**, 222503 (2010).

[183] N. M. Vargas, S. Allende, B. Leighton, J. Escrig, J. Mejia-Lopez, D. Altbir, and Ivan K. Schuller, J. Appl. Phys. **109**, 073907 (2011).

[184] M. Jaafar, R. Yanes, D. Perez de Lara, O. Chubykalo-Fesenko, A. Asenjo, E. M. Gonzalez, J. V. Anguita, M. Vazquez, and J. L. Vicent, Phys. Rev. B **81**, 054439 (2010).

[185] V. Cambel and G. Karapetrov, Phys. Rev. B **84**, 014424 (2011).

[186] Z. Zhong, H. Zhang, X. Tang, Y. Jing, L. Jia, and S. Liu, J. Magn. Magn. Mater **321**, 2345-2349 (2009).

[187] M. Konoto, T. Yamada, K. Koike, H. Akoh, T. Arima, and Y. Tokura, J. Appl. Phys. **103**, 023904 (2008).

[188] Y. Gaididei, D. D. Sheka, and F. G. Mertens, Appl. Phys. Lett. **92**, 012503 (2008).

[189] S. Yakata, M. Miyata, S. Honda, H. Itoh, H. Wada, and T. Kimura, Appl. Phys. Lett. **99**, 242507 (2011).

[190] V. Uhlir, M. Urbanek, l. Hladik, J. Spousta, M-Y. Im, P. Fischer, N. Eibagi, J. J. Kan, E. E. Fullerton, and T. Sikola, Nature Nanotechnology **8**, 341 (2013).

[191] G. Shimon, A. O. Adeyeye, and C. A. Ross, Phys. Rev. B **87**, 214422 (2013).

[192] A. Aharoni. IEEE Trans. Magn. **25**, 3470 (1989).

[193] K. Y. Guslienko and K. L. Metlov. Phys. Rev. B **63**, 100403 (2001).

[194] K. Y. Guslienko, N. Novosad, Y. Otani, H. Shima and K. Fukamichi. Appl. Phys. Lett. **78**, 3848 (2001).

[195] W. H. Meiklejoghn and C. P. Bean. Phys. Rev. **102**, 1413 (1956).

[196] J. Nogués and I. K. Schuller, J. Magn. Magn. Mat. **192**, 203 (1999).

[197] A. E. Berkowitz and K. takano, J. Magn. Magn. Mat. **200**, 442 (1999).

[198] M. Kiwi. J. Magn. Magn. Mat. **234**, 584 (2001).

[199] J. Nogués, J. Sort, V. Langlais, V. Skumryev, S. Suriñach, J. S. Muñoz, and M. D. Baró, Phys. Rep. **422**, 65 (2005).

[200] W. H. Meiklejohn, J. Appl. Phys. **33**, 1328 (1962).

[201] D. Mauri, H. C. Siegmann, P. S. Bagus, and E. Kay, J. Appl. Phys **62**, 3047 (1987).

[202] J. Geshev, Phys. Rev. B **62**, 5627 (2000).

[203] J. Geshev, S. Nicolodi, R. B. da Silva, J. Nogués, V. Skumryev and M. D. Baró, J. Appl. Phys **105**, 053903 (2009).

[204] H. Xi, R. M. White, Phys. Rev. B **61**, 80 (2000).

[205] A. P. Malozemoff, Phys. Rev. B. **35**, 3679 (1987).

[206] N. C. Koon, Phys. Rev. Lett **78**, 4865 (1997).

[207] T. C. Schulthess, W. H. Butler, Phys. Rev. Lett **81**, 4516 (1998).

[208] T. C. Schulthess, W. H. Butler, J. Appl. Phys. **85**, 5510 (1999).

[209] Y. Ijiri, J. A. Borchers, R. W. Erwin, S.-H. Lee, P. J. van der Zaag, and R. M. Wolf, Phys. Rev. Lett. **80**, 608 (1998).

[210] K. Takano, R. H. Kodama, and A. E. Berkowitz, Phys. Rev. Lett. **79**, 1130 (1997).

[211] H. Ohldag, T. J. Regan, J. Stör, A. Scholl, F. Nolting, J. Lünning, C. Stamm, S. Anders, and R. L. White, Phys. Rev. Lett. **87**, 247201 (2001).

[212] H. Ohldag, A. Scholl, F. nolting, E. Arenholz, S. Maat, A. T. Young, M. Carey, and J. Stöhr, Phys. Rev. Lett. **91**, 017203 (2003).

[213] M. R. Fitzsimmons, B. J. Kirby, S. Roy, Z.-P. Li, I. V. Roshchin, S. K. Sinha, and I. K. Schuller, Phys. Rev. B **75**, 214412 (2007).

[214] E. blackburn, C. Sanchez-Hanke, S. Roy, D. J. Smith, J.-I. Hong, K. T. Chan, A. E. Berkowitz, and S. K. Sinha, Phys. Rev. B **78**, 180408(R) (2008).

[215] S. Roy, M. R. Fitzsimmons, S. Park, M. Dorn, O. Petracic, I. V. Roshchin, Z.-P. Li, X. Batlle, R. Morales, A. Misra, X. Zhang, K. Chesnel, J. B. Kortright, S. K. Sinha, ans I. K. Schuller, Phys. Rev. Lett. **95**, 047201 (2005).

[216] J. Wu, J. S. Park, W. Kim, E. Arenholz, M. Liberati, A. Scholl, Y. Z. Wu, Chanyong Hwang, and Z. Q. Qiu, Phys. Rev. Lett. **104**, 217204 (2010).

[217] J. Sort, A. Hoffmann, S.-H Chung, K. S. Buchanan, M. Grimsditch, M. D. Baró, B. Dieny and J. Nogués. Phys. Rev. Lett. **95**, 067201 (2005).

[218] S. K. Mishra, F. Radu, S. Valencia, D. Schmitz, E. Schierle, H. A. Dürr, and W. Eberhardt, Phys. Rev. B **81**, 212404 (2010).

[219] J. Sort, K. S. Buchanan, V. Novosad, A. Hoffmann, G. Salazar-Alvarez, A. Bollero, M. D. Baró, B. Dieny and J. Nogués, Phys. Rev. Lett. **97**, 067201 (2006).

[220] R. Jungblut, R. Coehoorn, M. T. Johnson, J. aan de Stegge, A. Reinders, J. Appl. Phys. **75**, 6659 (1994).

[221] M. Ali, C. H. Marrows, M. Al-Jawad, B. J. Hickey, A. Misra, U. Nowak, and K. D. Usadel, Phys. Rev. B **68**, 214420 (2003).

[222] A. Fert, V. Cros, and João Sampaio, Nature Nanotechnology **8**, 152 (2013).

[223] J. Iwasaki, M. Mochizuki, and N. Nagaosa, Nature Communications **4**, 1463 (2013).

[224] A. Rosh, Nature Nanotechnology **8**, 160 (2013).

[225] N. Romming, C. Hanneken, M. Menzel, J. E. Bickel, B. Wolter, K. Bergmann, A. Kubetzka, and R. Wiesendanger, Nature **341** 636 (2013).

[226] http://www.ctcms.nist.gov/ rdm/mumag.org.html

[227] L. Lopez-Diaz, O. Alejos, L. Torres and J. I. Iniguez, J. Appl. Phys. **85**, 5813 (1999).

[228] R. D. McMichael, M. J. Donahue, and D. G. Porter, J. Appl. Phys. **85**, 5816 (1999).

[229] A. Aharoni, J. Appl. Phys. **83**, 3432 (1998).